UC San Diego

UC San Diego Electronic Theses and Dissertations

Title

Advanced Numerical Weather Prediction Techniques for Solar Irradiance Forecasting : : Statistical, Data-Assimilation, and Ensemble Forecasting

Permalink

https://escholarship.org/uc/item/9qn3v10q

Author

Mathiesen, Patrick James

Publication Date

2013

Peer reviewed|Thesis/dissertation

eScholarship.org Powered by the California Digital Library
University of California

UNIVERSITY OF CALIFORNIA, SAN DIEGO

Advanced Numerical Weather Prediction Techniques for Solar Irradiance Forecasting: Statistical, Data-Assimilation, and Ensemble Forecasting

A dissertation submitted in partial satisfaction of the
requirements for the degree Doctor of Philosophy

in

Engineering Sciences (Mechanical Engineering)

by

Patrick James Mathiesen

Committee in charge:

Professor Jan Kleissl, Chair
Professor Carlos Coimbra
Professor Robert Fovell
Professor Joel Norris
Professor Kraig Winters

2013

The dissertation of Patrick James Mathiesen is approved, and it is acceptable in quality and form for publication on microfilm and electronically:

_____

_____

_____

_____

_____

_____

Chair

University of California, San Diego

2013

EPIGRAPH

A lot of things can't be modeled very well.

Nate Silver

If you work really hard and you're kind, amazing things will happen.

Conan O'Brien

TABLE OF CONTENTS

Signature Page iii

Epigraph iv

Table of Contents v

List of Abbreviations vii

List of Symbols ix

List of Figures xi

List of Tables xiv

Acknowledgements xv

Vita xvii

Abstract of the Dissertation xviii

Chapter 1 Introduction 1
1.1 Challenges of Renewable Energy Integration 1
1.2 Solar Forecasting Overview 3
1.3 Solar Forecasting Techniques 5
1.3.1 Statistical Techniques 5
1.3.2 Imagery-Based Techniques 6
1.3.3 Numerical Weather Prediction (NWP) 7
1.4 NWP Error Sources 10
1.5 Project Overview 13

Chapter 2 Marine Layer Meteorology 17
2.1 Marine Layer Stratocumulus Overview 17
2.2 Climatology 22
2.3 Leipper Cycle 24
2.4 Mixed-Layer Cloud Dissipation Model 25
2.5 Acknowledgements 30

Chapter 3 Evaluation of Operational NWP for Solar Forecasting 31
3.1 Numerical Weather Prediction (NWP) Models 31
3.1.1 The North American Mesoscale Model (NAM) 31
3.1.2 The Global Forecasting System (GFS) 33
3.1.3 The European Centre for Medium Range Weather Forecasts Model (ECMWF) 34
3.2 Review of Previous Studies for Solar Irradiance Forecasting 35
3.3 Evaluation of the NAM, GFS, and ECMWF for irradiance forecasting in the continental United States 37
3.3.1 SURFRAD Ground Measurement Network 37
3.3.2 Forecasting Methods 38
3.3.3 Error Metrics 40
3.3.4 Effect of Spatial Averaging 41
3.3.5 Forecast Error of N_K, G, and E 42
3.4 Spatial Evaluation of the NAM for solar irradiance forecasting in California 44
3.4.1 CIMIS Ground Measurement Network 44

3.4.2 SolarAnywhere GHI Dataset 46
3.4.3 Spatial Accuracy Evaluation 46
3.5 Summary and Conclusions 49
3.6 Acknowledgements 49

Chapter 4 Statistical Correction Techniques for NWP 50
4.1 Model Output Statistics (MOS) Bias Correction 51
4.1.1 MOS Methodology 51
4.1.2 NAM MBE Correction 52
4.1.3 GFS MBE Correction 55
4.1.4 ECMWF MBE Correction 55
4.1.5 RMSE Comparison 56
4.2 Statistical Functions for Uncertainty Forecasts 58
4.2.1 Relating Synoptic Conditions to Forecast Accuracy 58
4.2.2 Historical rMBE Distribution 59
4.2.3 Uncertainty Interval Example 59
4.3 Summary and Conclusions 60
4.4 Acknowledgements 61

Chapter 5 A High-Resolution Cloud-Assimilating NWP 62
5.1 The Weather Research and Forecasting Model (WRF) 63
5.2 WRF Cloud Assimilation System (WRF-CLDDA) 64
5.2.1 GOES Cloud Data 64
5.2.2 WRF-CLDDA Methodology 65
5.3 WRF-CLDDA Validation 68
5.3.1 Qualitative Validation of a Single Day 68
5.3.2 Irradiance Error Metrics 70
5.3.3 Variability Error Metrics 77
5.4 Summary and Conclusions 81
5.5 Acknowledgements 84

Chapter 6 A WRF-Based Ensemble Forecasting System (WRF-SRAF) 85
6.1 WRF Configuration 86
6.2 Validation of Mixed-Layer Cloud Dissipation Model 90
6.3 Influence of Non-Idealized Conditions 92
6.4 Ensemble Composition and Bowen Ratio Uncertainty 94
6.5 WRF-SRAF Ensemble Validation 99
6.5.1 Ensemble Case Study 99
6.5.2 Accuracy Improvement and Dispersion Analysis 101
6.6 Summary and Conclusions 104
6.6 Acknowledgements 108

Chapter 7 Afterword 109

References 112

LIST OFABBREVIATIONS

3DVAR	Three-Dimensional Variational Data Assimilation
4DVAR	Four-Dimensional Variational Data Assimilation
ANN	Artificial Neural Network
AR	Auto-Regressive
ARIMA	Auto-Regressive Integrated Moving Average
ARMA	Auto-Regressive Moving Average
ARPS	Advanced Regional Prediction System
CAPS	Center for Analysis and Prediction of Storms
CCN	Cloud Condensation Nuclei
CDF	Cumulative Distribution Function
CE	Catalina Eddy
CFD	Computational Fluid Dynamics
CFL	Courant-Freidrichs-Lewy
CIMIS	California Irrigation Management Information System
CONUS	Continental United States
CSI	California Solar Initiative
CTD	Coastally Trapped Disturbance
CTT	Cloud Top Temperature
DEMROES	Decision Making using Real-time Observations for Environmental Sustainability
DNS	Direct Numerical Simulation
DWS	Department of Water Resources
ECMWF	European Centre for Medium-Range Weather Forecasts
ESRL	Earth Systems Research Laboratory
GDAS	Global Data Assimilation System
GFS	Global Forecast System
GFDL-SW	Geophysical Fluid Dynamics Laboratory Short-Wave
GHI	Global Horizontal Irradiance
GOES	Geostationary Operational Environmental Satellite
GSIP	GOES Surface and Insolation Product
GSI	Gridpoint Statistical Interpolation
HRRR	High-Resolution Rapid Refresh model
IWP	Ice Water Path
kNN	*k*-Nearest Neighbor
KSI	Kolmogorov-Smirnov Integral
LBLRTM	Line-By-Line Radiative Transfer Model
LCL	Lifting Condensation Level
LES	Large Eddy Simulation
LSM	Land-Surface Model
LWP	Liquid Water Path
MAE	Mean Absolute Error
MBE	Mean Bias Error
MLS	Marine Layer Stratocumulus
MM5	PSU/NCAR Mesoscale Model
MOS	Model Output Statistics

MRF	Medium Range Forecast
MYNN	Mellor-Yamada-Nakanishi-Niino PBL Model
NAM	North American Mesoscale Model
NCAR	National Center for Atmospheric Research
NCEP	National Centers for Environmental Prediction
NDFD	National Digital Forecast Database
NOAA	National Oceanic and Atmospheric Administration
NSAS	New Simplified Arakawa-Schubert cumulus parameterization
NWP	Numerical Weather Prediction
PBL	Planetary Boundary Layer
PSP	Precision Spectral Pyranometer
PST	Pacific Standard Time
PV	Photovoltaic
QC	Quality Control
RAP	Rapid Refresh Model
rMAE	Relative Mean Absolute Error
rMBE	Relative Mean Bias Error
rRMSE	Relative Root-Mean Squared Error
RMSE	Root-Mean Squared Error
RPS	Renewable Portfolio Standards
RR	Ramp Rate
RRTM	Rapid Radiative Transfer Model
rSTDERR	Relative Standard Error
RTM	Radiative Transfer Model
RUC	Rapid Update Cycle
RUC-LSM	Rapid Update Cycle Land-Surface Model
SAS	Simplified Arakawa-Schubert
STDERR	Standard Error
SURFRAD	Surface Radiation Budget Network
TKE	Turbulent Kinetic Energy
UTC	Universal Coordinated Time
WRF	Weather Research and Forecasting Model
WRF-ARW	Advanced Research WRF
WRF-CLDDA	WRF-Cloud Data Assimilation
WRF-NMM	WRF-Nonhydrostatic Mesoscale Model
WRF-SRAF	WRF-Solar Resource Assessment and Forecasting

LIST OF SYMBOLS

A	Scale area of domain discretization
β	Bowen ratio
C	Clear Sky Model
CDF_{CSK}	CDF of clear sky irradiance ramp rates
$CDF_{Obs.}$	CDF of observed irradiance ramp rates
$c_{p,B}$	Bulk specific heat of air in the planetary boundary layer
$\Delta\gamma(q_g)$	Change in ground water mixing ratio according to background uncertainty
Δt	Time-step size
Δx	Horizontal discretization size
Δz	Vertical discretization size
E	ECMWF Forecast
E_c	ECMWF Forecast – MOS Corrected
ε	Ratio of moist- to dry-air gas constants
e_s	Saturation water vapor pressure
G	GFS Forecast
G_c	GFS Forecast – MOS Corrected
GHI_c	Corrected global horizontal irradiance at the surface
GHI_{CSK}	Clear-sky global horizontal irradiance at the surface
$GHI_{Obs.}$	Observed global horizontal irradiance at the surface
k	Radiative absorption coefficient
KSI_{CSK}	KSI statistic between observation and clear sky irradiance
kt^*	Forecast clear sky index
kt_m	Observed clear sky index
LCL	Lifting condensation level
L_v	Latent heat of vaporization for water
m_{PBL}	Air mass of planetary boundary layer
N	NAM Forecast
N_K	NAM Forecast – kt^* Interpolated
$N_{K,c}$	NAM Forecast – MOS Corrected
P	Atmospheric pressure
P_1	Persistence Forecast – 1 Hour
P_{24}	Persistence Forecast – 24 Hour Persistence Forecast
P_{10}	Irradiance/power forecast that 10% of observations will exceed
P_{50}	Irradiance/power forecast that 50% of observations will exceed (median)
P_{90}	Irradiance/power forecast that 90% of observations will exceed (median)
Q_E	Latent heat flux at surface
Q_H	Sensible heat flux at surface
Q_T	Total upward moisture flux at surface
Q_U	Total upward heat flux at surface
q_g	Ground water mixing ratio
q_i	Ice water mixing ratio
q_L	Liquid water mixing ratio
q_s	Saturation water vapor mixing ratio
q_T	Total water mixing ratio

q_v	Water vapor mixing ratio
ρ_B	Bulk density of planetary boundary layer
$RR_{\Delta t}$	Irradiance ramp rates for timescale Δt
R_v	Gas constant for moist air
T	Temperature
T_B	Bulk temperature of planetary boundary layer
θ_L	Liquid-Water Potential Temperature
u	Wind velocity in x-direction
u_g	E-W Geostrophic wind velocity
V	Variability ratio
$w'\theta_L'$	Vertical turbulent heat flux
$z_{c,base}$	Cloud Base Altitude
z_i	Inversion altitude

LIST OF FIGURES

Fig. 1.1: Average observed percent clear sky irradiance (GHI_{CSK}) for June 2010 at 0630 PST from the SolarAnywhere dataset. Black circles represent major CSI rooftop PV installations. 3
Fig. 1.2: Classification of forecast methodologies by spatial and temporal resolution (from Diagne *et al.*, 2013). 4
Fig. 1.3: NAM GHI forecast (W m^{-2}) for 4/10/2010 at 2000 UTC for the NAM domain over North America. 8
Fig. 2.1: A schematic depicting the formation of marine layer stratocumulus clouds (from Bennetts *et al.*, 1986). 19
Fig. 2.2: Example of a distinct Catalina Eddy event and its effect on MLS in southern California. The satellite image is taken from Mass and Albright (1989). 21
Fig. 2.3: Normalized GHI observations (% of instantaneous clear sky irradiance) at the University of California, San Diego (-117.23° W, 32.88° N, approximately 1 km from the Pacific Ocean). Observed irradiance is lowest during the mornings in the months of May-September corresponding with the occurrence of marine layer stratocumulus clouds. 23
Fig. 2.4: Average MLS dissipation time as measured by SolarAnywhere for days in which MLS clouds were observed in May and June, 2011. 23
Fig. 2.5: Schematic of water mixing ratios within the well-mixed layer (a) showing total water mixing ratio (q_T, solid black line), saturation mixing ratio (q_S, dashed black line), water vapor mixing ratio (q_v, solid blue line), liquid (cloud) water mixing ratio (q_L, shaded-lined area), lifting condensation level (LCL, z_b, red dashed line) and temperature inversion (z_i, red solid line). Fig. 2.5b shows the effect of an upward latent heat flux (Q_E) on the cloud layer (q_T increases) while Fig. 2.5c shows how an upward sensible heat flux (Q_H) influences the cloud layer (q_S decreases). In b and c the original q_S and q_T are shown as thin black lines and the original q_v is a thin blue line. 25
Fig. 3.1: GHI forecasts compared against Desert Rock, NV SURFRAD ground measurements on July, 17th 2010. *N*: linear interpolated NAM; N_K: clear sky index interpolated NAM; *G*: GFS three hour constant clear sky index; *E*: ECMWF three hour constant clear sky index; *P*: persistence; *C*: clear sky forecast. 38
Fig. 3.2: N_K MAE (W m^{-2}) as a function of measured clear sky index (kt_m) for different averaging radii of the NAM model. 50, 100, and 200 km averaging radii correspond to approximately 80, 300, and 1250 grid points, respectively. 42
Fig. 3.3: NWP forecast MBE (W m^{-2}) as a function of SZA and measured clear sky index for all SURFRAD stations for a) N_K; b) *G*; c) *E*. 44
Fig. 3.4: CIMIS weather station locations for California. Black triangles are stations 75 km or more from the coast and red triangles are stations within 25 km of the coast. 45
Fig. 3.5: N_K bias error distribution for coastal (black solid line, distance to Pacific Ocean < 25 km) and inland (blue dashed line, distance to Pacific Ocean > 75 km) CIMIS stations for (a) May – July 2010 and (b) November 2010 – January 2011. 47
Fig. 3.6: N_K MBE (W m^{-2}, top) and STDERR (W m^{-2}, bottom) compared to SolarAnywhere data for May, June, and July, 2010 (a/c) and November and December 2010 (b/d). 47
Fig. 3.7: N_K 90% forecast interval for coastal CIMIS Station 173 (a, San Diego, CA) and inland CIMIS Station 128 (b, Salton Sea, CA) based on the historical bias error distribution from summer 2010 (Fig. 3.5a). 48
Fig. 4.1: Histogram as a function of solar zenith angle (*SZA*) and clear sky index (*kt**) for a) N_K; b) *G*; c) *E*. Data is presented in $\log_{10}$ format, i.e. a value of 2 indicates 100 observations. All data to the left of the black line (*SZA* > 75°) were not used in the MOS analysis. 53

Fig. 4.2: MBE (W m^{-2}) of N_K (a), G (b), and E (c), as a function of solar zenith angle (SZA) and forecasted clear sky index (kt^*) compared to SURFRAD measurements: i) raw data, ii) polynomial fit to the data (Eq. 4.1); iii) MBE of the corrected forecasts: $N_{K,c}$, G_c, and E_c 54
Fig. 4.3: RMSE (W m^{-2}) as a function of measured clear sky index (kt_m): a) (N_K, G, E, P_1, P_{24}, and C); b) ($N_{K,c}$, G_c, E_c, P_1, P_{24}, and C); c) Change in RMSE due to MOS correction. 56
Fig. 4.4: N_K STDERR (a, W m^{-2}) and rSTDERR (b, [% Clear Sky]) as a function of 700 mb geostrophic wind direction and velocity (m s^{-1}) for coastal CIMIS stations between May 1st, 2011 and July 31st, 2011. Velocity ranges from 0 m s^{-1} (center) to 11 m s^{-1} (outside edges). 58
Fig. 4.5: rMBE 5% (a) and 95% (b) interval limits (% of clear sky GHI) averaged over all CIMIS stations for May 1st, 2011 – July 31st, 2011. 59
Fig. 4.6: May 3rd, 2011 700 mb geopotential height anomaly (m) and corresponding N_K forecast interval for CIMIS station 173 compared against the intervals obtained by Lorenz *et al.* (2009). Westerly atmospheric flow conditions (a) correspond with likely cloudy conditions. 60
Fig. 5.1: WRF-CLDDA nest configuration (Δx = 12 km, 4 km, 1.3 km) centered at the University of California, San Diego using Google Earth. 64
Fig. 5.2: WRF-CLDDA direct cloud assimilation system overview. 65
Fig. 5.3: a) GOES cloud mask, where green is cloudy and white is clear and b) Δq_v (kg kg^{-1}) for assimilated initial conditions on 6/13/2011. 68
Fig. 5.4: NAM (left) and WRF-CLDDA (right) cross-sections for 6/13/2011 depicting cloud extent (green) and temperature inversion height (dashed red line). The black vertical line marks the location of UCSD. For all forecasts, marine layer cloud cover extent is greatest in the early morning (0600 PST). As temperature near the surface increases, the temperature inversion rises and marine layer clouds over land dissipate until 1200 PST. 69
Fig. 5.5: Time-series of 5-min. observed (black), hourly NAM-predicted (blue), and 5-min. WRF-CLDDA-predicted (red line) GHI for 6/13/2011. 70
Fig. 5.6: Map of WRF-CLDDA grid cells (Δx = 1.3 km) and DEMROES pyranometer locations (red circles). Blue circles show DEMROES sites that were not analyzed and the black line demarks the Pacific coast. 71
Fig. 5.7: Joint clear sky index (kt_m/kt^*) and time of day (hr PST) histogram for observations (a), NAM (b) and WRF-CLDDA (c) intra-day and day-ahead forecasts for UCSD in May and June 2011. 72
Fig. 5.8: rMAE (% GHI_{CSK}) of NAM (left) and WRF-CLDDA (right) forecasts compared to SolarAnywhere data at several times of day. In early morning hours, NAM forecasts are much less accurate, especially over oceanic and coastal regions, indicating a deficiency in predicting marine layer cloud cover. 76
Fig. 5.9: KSI_{CSK} examples for a clear day (5/1/2011, a) and a highly variable day (5/18/2011, b). The main plots compare the CDF of observed (black line) and clear sky (green line) RR with KSI_{CSK} equal to the shaded area. Insets show the instantaneous 5-min. RR. 78
Fig. 5.10: Variability ratio (V, Eq. 5.6, y-axis) as a function of the daily variability statistic ($KSI_{CSK} \cdot \Delta t$) for NAM and WRF-CLDDA 60 min. ramp rates. Each dot represents a single day. Lines and bars indicate the mean and standard deviation of V in bins of 20 W m^{-2} on the x-axis. 79
Fig. 5.11: Variability ratio as a function of the daily variability statistic ($KSI_{CSK} \cdot \Delta t$) for WRF-CLDDA ramp rates of Δt = 5 min. (a), Δt = 10 min. (b), and Δt = 30 min. (c). Dots represent single days. 81
Fig. 6.1: WRF domain configuration (Δx=2.5 km) centered at the University of California, San Diego. Image created using Google Earth. 87
Fig. 6.2: Simulated vertically-averaged cloud water mixing ratio (a, $<q_L>$) as a function of time and Bowen ratio (β, legend) and simulated horizontally-averaged $w'\theta_L'$ heating profiles (b, at

1200 PST) using the simplified 2-D WRF model. Near the surface, inhomogeneous heating occurs for large β. 91
Fig. 6.3: WRF-simulated $d\langle q_L \rangle dt^{-1}$ compared to analytical $d\langle q_L \rangle dt^{-1}$ as derived from the mixed layer model (Eq. 2.19) for vertically-averaged PBL variables for all data in Fig. 6.2a. Inset (same axes) shows the average values over the period of cloud dissipation (maximum to minimum in Fig. 6.2), where labels indicate the Bowen ratio of the simulation. 92
Fig. 6.4: WRF-simulated vertically-averaged potential temperature tendency ($d\langle \theta \rangle dt^{-1}$) and corresponding liquid water tendency ($d\langle q_L \rangle dt^{-1}$) partitioned by source for the ocean (a/c) and land (b/d) on 15 June 2011 with average Bowen ratios of ≈1.5 (land) and ≈0.6 (water). Over land, cloud dissipation occurs at 1100 PST. 94
Fig. 6.5: Median bias (WRF – satellite observed) of cloud dissipation time (a, hr) and average cloud dissipation rate (b, kg kg^{-1} hr^{-1}) for MLS days in May and June, 2011. For days and locations in which no clouds are observed or simulated, no dissipation rate is calculated. Oceanic data and locations with no cloud cover were ignored (white areas). 96
Fig. 6.6: May and June 2011 error distribution of β (a-c) and q_g (m^3 m^{-3}, d-f) at three γ (percentile) levels: 10% (a/d), 50% (b/e), and 90% (c/f). Dashed contours (d-f) show distance-averaged Δq_g. Negative $\Delta_\gamma q_g$ indicate that the soil is too dry. 97
Fig. 6.7: Example columnar cloud water content (a, kg) and resulting irradiance (b, W m^{-2}) forecast for 15 June 2011 at La Jolla, CA (117.23° W 32.88° N – red circle in Fig. 6.9, later) using the WRF cloud lifetime ensemble. 100
Fig. 6.8: Cumulative distribution functions (CDFs) of simulated β (a), vertically-averaged relative humidity (b), vertically-averaged potential temperature (c), and vertically-average cloud-water mixing ratio (d) for original forecasts with NAM-provided soil moisture contents (black thick-solid line) compared to ensemble members with adjusted soil moisture contents. Only locations within 30 km of the coast were considered. 101
Fig. 6.9: MAE (W m^{-2}) of WRF forecasts with NAM-provided soil moisture contents (a) and ΔMAE for P_{10} (b), P_{50} (c), and P_{90} (d) forecasts on MLS days in May and June, 2011. Forecast improvement is largest within 15 km of the coast. Red circles denote La Jolla, CA. 101
Fig. 6.10: The dissipation timing bias cumulative distribution functions (CDFs) for original forecasts with NAM-provided soil moisture contents (blue thin-dashed line) and the P_{50} ensemble member with adjusted soil moisture contents (red thin-solid line) for all locations (e.g. Fig. 6.5). 103
Fig. 6.11: Forecast clear sky index spread ($P_{10} - P_{90}$) as a function of time of day and distance to coast. 104

LIST OF TABLES

Table 3.1: Comparison of the forecast timesteps over a single day. Boxes represent averaging periods of constant clear sky index kt^* (kt_m for P_1 and P_{24}). N_K is interpolated from hourly instantaneous values and assumed to apply over the entire hourly interval. The GFS provides a combination of 3 and 6-hour interval forecast, from which 3-hour forecasts can be back calculated (striped box). 40
Table 3.2: Normalized frequency of clear and cloudy forecasts and observations for each NWP model. The threshold to distinguish between cloudy and clear conditions is a clear sky index of 0.8. 43
Table 4.1: MBE and RMSE for NWP forecasts before and after MOS correction averaged across all sites. 61
Table 5.1: Summary of hourly-average error metrics for persistence, NAM, and WRF-CLDDA irradiance forecasts at UC San Diego. 73
Table 5.2: Error summary (% GHI_{CSK}) as divided by month. 73
Table 5.3: rMBE and rRMSE error summary (% GHI_{CSK}) as divided by clear sky index. Lara-Fanego *et al.*, 2011 values are reported as the range of annual error between observation sites... 75
Table 5.4: rMBE and rRMSE error summary as a percentage of persistence error as divided by clear sky index. 75
Table 6.1: Summary of WRF Configuration 89
Table 6.2: Vertically averaged liquid water tendency ($d\langle q_L \rangle\, dt^{-1}$) partitioned by source for 15 June 2011 between 0400 and 1100 PST. Percentages are calculated by taking the absolute values of the $\langle q_L \rangle$ tendencies. 94

ACKNOWLEDGEMENTS

First and foremost I would like to thank the many people whose helpful discussions were more valuable to the completion of this dissertation than any single course or presentation. Without the countless number of hallway conversations and impromptu brainstorm sessions none of this work would have been possible. Notably, Brian D'Agostino and Steve Vanderburg of San Diego Gas and Electric provided meteorological expertise and were exceptionally welcoming, having hosted numerous meetings at their weather center. Furthermore, SDGE provided the essential computational resources used for this dissertation. Rachel Schwartz and Joel Norris of the Scripps Institute of Oceanography and Israel Lopez-Coto, Mohamed Ghonima, and Bryan Urquhart of UCSD provided insightful discussions that lead to several key developments in the project. Joseph Olson, John Brown, and others at the Earth Systems Research Laboratory provided in-depth explanations of WRF physics parameterizations and had many research suggestions. Lastly, I would like to thank Roy Rasmussen of NCAR, whose astute comments at the Southern California Modeling Workshop on June 3rd, 2013 sparked the pivotal developments of the final tasks of this dissertation.

Additionally, I would like to thank Craig Collier, Patrick Shaw, and Daran Rife of GL-Garrad Hassan for assistance in WRF modeling and for giving me the opportunity to apply this work in an operational setting. Their support over the last two years has been outstanding. I would like to also acknowledge advising and funding support from Jan Kleissl and the Mechanical and Aerospace Engineering department at the University of California, San Diego.

Finally, portions of this work have been previously published. Chapter 2.1 and 2.2 contains material from Mathiesen *et al.*, 2013b and Mathiesen *et al.*, 2014. Chapter 2.3 uses published material from Mathiesen *et al.*, 2013a and Chapter 2.4 is based off of Mathiesen *et al.*, 2014. Chapter 3, sections 1-3 are based off of Mathiesen and Kleissl, 2011 while section 4 is

from Mathiesen *et al.*, 2013a. Chapter 4.1 uses work from Mathiesen and Kleissl, 2011 and Chapter 4.2 is based off of Mathiesen *et al.*, 2013a. Chapter 5, in full, has been previously published as Mathiesen *et al.*, 2013b. Finally, Chapter 6, in full, has been submitted for publication as Mathiesen *et al*., 2014. For each of these, the dissertation author was the primary investigator and author. I would like to thank each of my previous co-authors for their contributions and for their permission to reproduce this work in this dissertation.

VITA

2009 Bachelor of Science, University of Minnesota, Twin Cities

2010 Master of Science, University of California, San Diego

2013 Doctor of Philosophy, University of California, San Diego

PUBLICATIONS

Mathiesen, P., J. Norris, I. Lopez-Coto and J. Kleissl, 2014: Development of a cloud lifetime ensemble for solar irradiance forecasting. Submitted to *Monthly Weather Review*, October 2013.

Lopez-Coto, I., **P. Mathiesen**, and J. Kleissl, 2014b: Deterministic prediction using various post-processing methods for solar irradiance forecasting. In preparation.

Lopez-Coto, I., **P. Mathiesen**, J.L. Bosch, and J. Kleissl, 2014a: Comparison between several parameterization schemes in WRF for solar forecasting in coastal zones. In perparation.

Mathiesen, P., C. Collier, and J. Kleissl, 2013c: Case studies of solar forecasting with the weather research and forecasting model at GL-Garrad Hassan in *Solar Energy Forecasting and Resource Assessment, 1st Ed.*. Editor: Jan Kleissl. Elsevier Publishing, 2013.

Mathiesen, P., C. Collier, and J. Kleissl, 2013b: A high-resolution, cloud-assimilating numerical weather prediction model for solar irradiance forecasting. *Solar Energy*, **92**, 47-61.

Mathiesen, P., J.M. Brown, and J. Kleissl, 2013a: Geostrophic wind dependent probabilistic irradiance forecasts for coastal California. *IEEE Transactions on Sustainable Energy*, **4** (2), 510-518.

Mathiesen, P., and J. Kleissl, 2011: Evaluation of numerical weather prediction for intra-day solar forecasting in the continental United States. *Solar Energy*, **85** (5), 967-977.

FIELDS OF STUDY

Major Field: Mechanical Engineering, Atmospheric Science, Fluid Dynamics

ABSTRACT OF THE DISSERTATION

Advanced Numerical Weather Prediction Techniques for Solar Irradiance Forecasting: Statistical, Data-Assimilation, and Ensemble Forecasting

by

Patrick James Mathiesen

Doctor of Philosophy in Engineering Sciences (Mechanical Engineering)

University of California, San Diego, 2013

Professor Jan Kleissl, Chair

To effectively manage the growing density of solar power installations, grid operators are increasingly relying on solar forecasts to predict irradiance and power from minutes to days ahead. For forecast horizons of five hours or greater, large-scale computational fluid dynamics models known collectively as numerical weather prediction (NWP) is the most accurate method of predicting solar irradiance. Though more accurate than statistical regression or imagery based techniques, NWP is consistently erroneous and generally under-represents cloud cover; approximately half of all cloudy days are incorrectly forecast as clear. Furthermore, these errors are exacerbated for regions with dynamic cloud cover such as the California coast. On average, this results in irradiance over-predictions of 20-25%. Overall, these weaknesses limit NWP's

utility for solar power forecasting. However, by coupling meteorological theory with statistical techniques and model improvements, a specialized forecasting system can be developed that significantly improves forecast accuracy.

In this study, several advanced NWP techniques are implemented to improve forecast accuracy. First, the accuracy of the existing operational NWP is evaluated. By relating forecast accuracy to meteorological regime, model-output-statistics (MOS) is used to bias-correct forecasts and improve mean absolute error (MAE) by approximately 5%. Additionally, MOS was used to characterize forecast certainty; meteorological regimes with historically erroneous forecasts were prescribed with wider confidence intervals. Though valuable for operational forecasting, statistical models such as these fail to address the model weaknesses that prevent the accurate simulation of clouds.

To directly improve cloud simulations, a high-resolution NWP specialized for solar irradiance forecasting in coastal areas was developed and implemented operationally (WRF-SRAF). Using Weather Research and Forecasting Model (WRF) architecture, WRF-SRAF was used to predict solar irradiance for days in which marine layer stratocumulus (MLS) clouds were observed in San Diego, CA. In general, it was found that simulated MLS clouds dissipated 1.9 hours earlier than observed and that model error was primarily attributed to inaccurate initial conditions and incorrect treatment of the surface energy balance. To improve model initializations, a method of direct-cloud assimilation was implemented. In this method, satellite observations were co-located with the model domain. For areas with observed cloud cover, modeled water vapor was raised to super-saturation, populating clouds in the initial conditions.

Lastly, a cloud dissipation model was derived in order predict the influence of the surface heat fluxes on cloud evaporation. It was found that, due to extraordinarily dry boundary conditions, simulated sensible heat fluxes were 2-3 times larger than observed. Subsequently, a background uncertainty in the surface boundary conditions was established and used to motivate

a systematic perturbation to future simulations. Using this surface modification in an ensemble setting, solar forecast accuracy improved by over 7% and the dissipation of MLS clouds was more accurately characterized.

.

Chapter 1 Introduction

1.1 Challenges of Renewable Energy Integration

To meet the rising demand for clean, renewable energy and to combat the emission of greenhouse gasses into the atmosphere, states have implemented Renewable Portfolio Standards (RPS) which dictate the amount of renewable energy that must be integrated into the electricity grid. In California, the current RPS calls for 33% of all energy to be provided by renewable sources by the year 2020 (Peterman, 2012), the majority of which is expected to come from variable sources such as wind and solar power. Integration of this penetration of renewable resources into the energy production portfolio would reduce carbon dioxide emissions by approximately 25% (Lew and Piwko, 2010).

However, several challenges exist to meet this goal. When no sources of renewable energy are implemented, energy production is steady and consistent. The entity in charge of balancing energy supply and demand, the independent system operator (ISO), must only predict demand and appropriately dispatch load-following power plants. When renewable sources are included, however, their uncertain and variable nature complicates grid management. For instance, since exact production is unknown in advance, the deviation between supply and demand is unknown and potentially very large. As such, extra reserve power plants must be kept on standby and ready to deploy in the event of an energy shortfall. Additionally, short-term fluctuations in renewable energy production (such as when a cloud field suddenly covers a solar power plant) increase short-term regulation requirements. Overall, load-following capacity requirements increase by 12-14% on average when renewable resources are included in the energy portfolio (Venkataraman *et al.*, 2010).

To mitigate this effect, energy production forecasts are utilized. Forecasts are used by the ISO to determine scheduling for load-following power plants and energy transmission. By

reducing the uncertainty in energy production estimates, accurate production forecasts reduce the required capacity of deployable energy reserves. Furthermore, by predicting production variability, intermittent shortfalls and excesses in energy production can be effectively managed well in advance. Using current forecasting methods, grid-management operating costs can be reduced by up to 14%. Perfect forecasts, however, could potentially reduce costs by an additional $500M/year (Lew and Piwko, 2010). Thus, improving on the operational methods of renewable energy forecasting is an important and monetarily significant subject of research.

In California, a large portion of the RPS is fulfilled by rooftop solar photovoltaic (PV) generation. This presents special challenges as the majority of these installations are co-located with the ubiquitous marine layer stratocumulus (MLS) clouds found in coastal California (Fig. 1.1). MLS clouds are low-level, optically thick clouds that can reduce irradiance at the surface by up to 70% (Chapter 2) and are notoriously difficult to predict. Spatially, MLS conditions are limited by topography and they rarely penetrate inland further than 30 km. Additionally, their dissipation is spatially correlated. Thus, if neighboring residential units install rooftop PV systems on a common distribution feeder, these cloud systems can cause localized production ramps that are especially difficult to manage. Fig. 1.1 shows the average clear sky index (kt_m, observed irradiance normalized by the expected clear sky irradiance) for June 2010 at 0630 PST. Here, black circles represent participants in the California Solar Initiative (CSI) program and locations of installed rooftop PV.

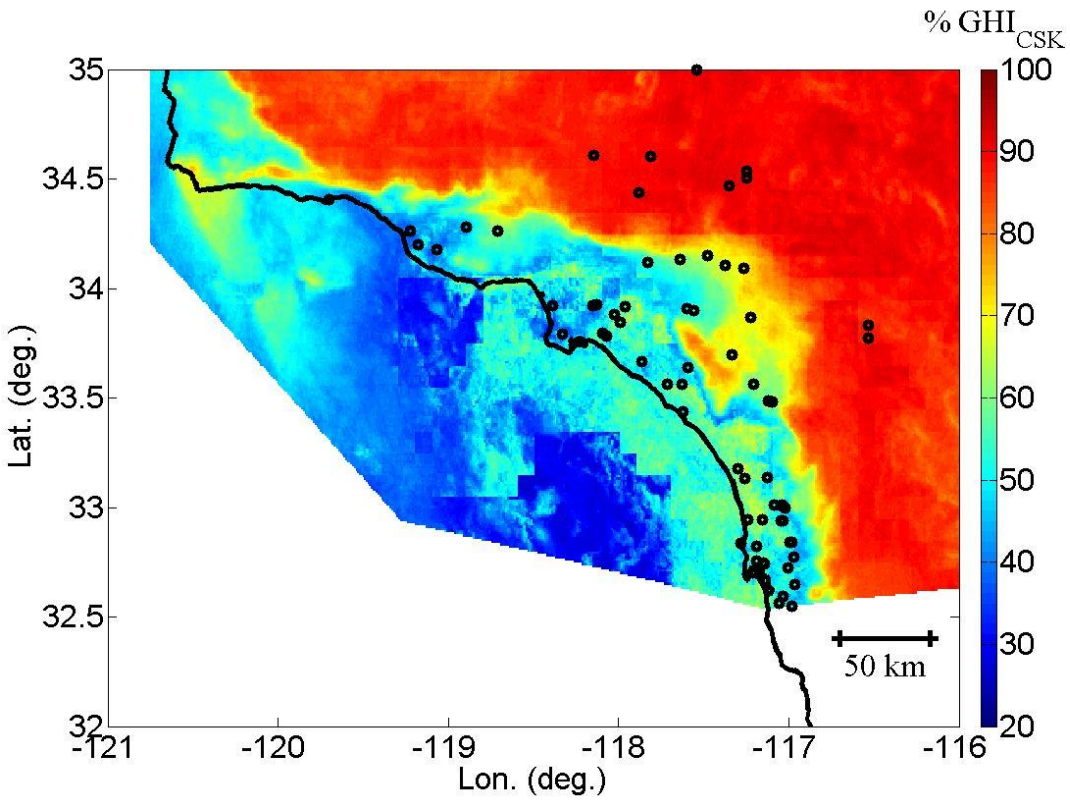


Fig. 1.1: Average observed percent clear sky irradiance (GHI_{CSK}) for June 2010 at 0630 PST from the SolarAnywhere dataset. Black circles represent major CSI rooftop PV installations.

1.2 Solar Forecasting Overview

Several methods of solar forecasting have been developed to accurately predict global horizontal irradiance (GHI) at the surface. In general, solar forecasting methods can be characeterized by their spatial and temporal scales (Fig. 1.2). At very short horizons (less than one hour), grid operators require precise forecasts for real-time energy dispatching. In this regime, statistical autoregressive models based on recent observations of irradiance and other meteorological variables are generally the most accurate. Alternatively, sky-imagery, in which a network of cameras is used to characterize the exact cloud condition and predict cloud movement, is also often employed. Though very accurate, these methods are only valid for short forecast horizons (sometimes as small as 15 minutes) and their spatial coverage is poor. For slightly

longer forecast horizons (1 to 5 hrs), satellite-based imagery techniques are generally the most accurate. Here, the satellite-observed cloud field is frozen and advected based on observed or derived cloud wind speeds. Since satellite spatial coverage is excellent, this method is often accurate over very large spatial scales (> 100 km) especially for static or well developed cloud fields. However, imagery-based techniques are incapable of predicting cloud formation or dissipation. As such, their accuracy diminishes after several hours. For longer forecast horizons (greater than 5 hours), physics-based weather models (numerical weather prediction (NWP)) are generally the most accurate method (Perez et al., 2010). Since NWP directly simulate the atmospheric thermodynamics that govern cloud cover, cloud formation and dissipation is intrinsically predicted and GHI is accurately characterized. Overall, a robust solar forecasting system will combine different methods to provide accurate energy forecasts at different spatial and temporal scales.

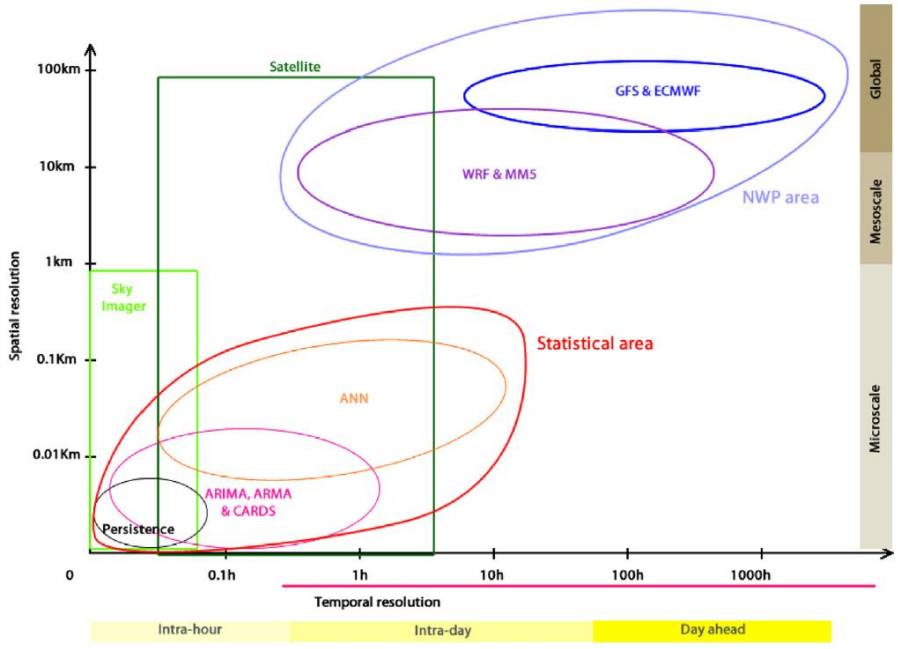


Fig. 1.2: Classification of forecast methodologies by spatial and temporal resolution (from Diagne *et al.*, 2013).

1.3 Solar Forecasting Techniques

1.3.1 Statistical Techniques

Since weather conditions change very little over short time scales, statistical techniques based on recent observations are the most accurate method for solar irradiance forecasting. In general, these methods can be divided into two primary groups: Regressive and Artificial Intelligence Models. Complete overviews of these methods are provided in the comprehensive solar forecasting reviews by Inman *et al.* (2013) and Diagne, *et al.* (2013).

Assuming that clouds and their effect on irradiance are static forms the basis of the simplest regressive-based forecast, the *persistence* forecast. Here, recent observations are assumed to 'persist' into the future. However, irradiance does not remain constant, even in the absence of clouds. As such, recent GHI observations are not ideal for persistence forecasts. Instead, the clear sky index (kt_m, Eq. 1.1) is generally used.

$$kt_m = \frac{GHI_{Obs.}}{GHI_{CSK}} \qquad \text{Eq. 1.1}$$

kt_m is a semi-stationary signal (Hansen *et al.*, 2010) that describes the GHI as normalized by the expected irradiance under clear conditions (GHI_{CSK}). *G*iven a time, location, and altitude, GHI_{CSK} is calculated using the Ineichen clear sky model (Ineichen and Perez, 2002) which accounts for climatological changes in local turbidity using aerosol, ozone, and water vapor from the 8 km SoDa gridded solar radiation project (Wald *et al.*, 2000). The persistence forecast is calculated by multiplying the previously observed kt_m with future GHI_{CSK}. In general, persistence represents the simplest possible forecast and provides a baseline for forecast skill from which new techniques or models can compare to.

Expanded from simple persistence techniques are more robust stochastic models. Auto-regressive (AR) models use a linear combination of recent observations (generally of kt_m) to

predict future irradiance (Box *et al.*, 2008). AR models can be extended to include a moving average (MA) component (a linear combination of historical forecast deviations) to form the well known ARMA and ARIMA models (Box *et al.*, 2008, Reikard, 2009, Marquez and Coimbra, 2011, Coimbra and Pedro, 2013). Similarly, artificial intelligence models are often employed for short time scales. Artificial neural networks (ANNs) pass multiple input data through transfer functions, which are subsequently weighted and combined to produce a forecast (Inman *et al.*, 2013). Alternatively, k-NN (k-Nearest-Neighbor) algorithms assume that future conditions can be represented by historical observations. For example, on a given day in San Diego a marine layer stratocumulus cloud may dissipate at 10 AM. The observed irradiance signal from this day could then be used to forecast irradiance for future dates in which it is determined likely that a morning marine layer dissipation would occur. To determine which days are most analogous, other meteorological forecasts such as temperature, relative humidity, and pressure patterns are used. Compared to other forecasting methodologies, the analogues technique (Lopez-Coto *et al.*, 2014b) is most accurate. Several other studies have been performed that evaluate the relative accuracy of statistical based models (Reikard, 2009, Sfetsos and Coonick, 2000). In general, statistical and artificial intelligence techniques fill the important short-time scale role in a solar forecasting system.

1.3.2 Imagery-Based Techniques

For physics-based forecasting, imagery-based cloud-advection techniques provide excellent characterizations of cloud fields and their motion. In these methods, ground or satellite camera systems capture images of cloud fields. After a cloud mask or classification is assigned, cross-correlation is used between successive images to obtain cloud velocity. Subsequently, the observed cloud field is advected, forecasting its future location. Combined with a radiative transfer model or clear-sky index assumptions, a forecast of irradiance can be made.

For very short forecast horizons, sky-imagery (Chow *et al.*, 2011, Ghonima *et al.*, 2012, Urquhart *et al.*, 2013, Urquhart *et al.*, 2014) is the most accurate method for predicting cloud location. Using domed-mirror or fish-eye lens cameras, sky-imagers capture cloud fields at high spatial (meters) and temporal resolution (sub-minutely). This provides the fidelity necessary to accurately predict the variable irradiance ramps that are characteristic to intermittent cloud fields. Additionally, recent advances have allowed for stereographic sky-imagers to detect cloud-height in addition to multiple cloud levels and cloud type. However, sky-imager techniques currently are unable to predict cloud dynamics and have limited spatial range (< 5 km). As such, their utility is limited to forecast horizons of less than 15 minutes. For slightly longer forecast horizons (15 minutes to 5 hours), satellite-based imagery techniques are more accurate (Perez *et al.*, 2010, Miller *et al.*, 2013). Here, cloud fields over large geographic regions can be captured, but at much lower spatial resolutions (≈ 4 km). Like sky-imagery, satellite-based frozen-cloud advection techniques do not account for cloud dynamics. Since cloud fields are likely to change over the course of a few hours, accuracy diminishes with forecast horizon.

1.3.3 Numerical Weather Prediction (NWP)

For longer forecast horizons, numerical weather prediction (NWP) is the most accurate method for predicting solar irradiance (Perez *et al*, 2010). NWP are large-scale computational fluid dynamics (CFD) models in which the Euler equations of motion and energy are numerically solved on a discretized grid. Here, velocity, pressure, temperature, and water constituents are the native variables which are predicted at each time step. Other variables, such as irradiance and surface heat fluxes, are calculated from secondary physics modules and used to drive the surface boundary conditions. Initialized by a combination of larger scale models and observations, NWP provide full-atmosphere solutions for forecast horizons of up to 7 days in advance. Typical grid resolutions range from 1 km for localized, high-resolution simulations to 100 km for global

models. At these length scales, flow is considered inviscid, yielding the Euler equations in place of the Navier-Stokes. However, several forcing terms are calculated by physics parameterizations and added to the Euler equations to account for the effect of viscosity in the boundary layer, sub-grid scale turbulence, and atmospheric thermodynamics. Fig. 1.3 shows an example GHI forecast for the North American Mesoscale Model (NAM).

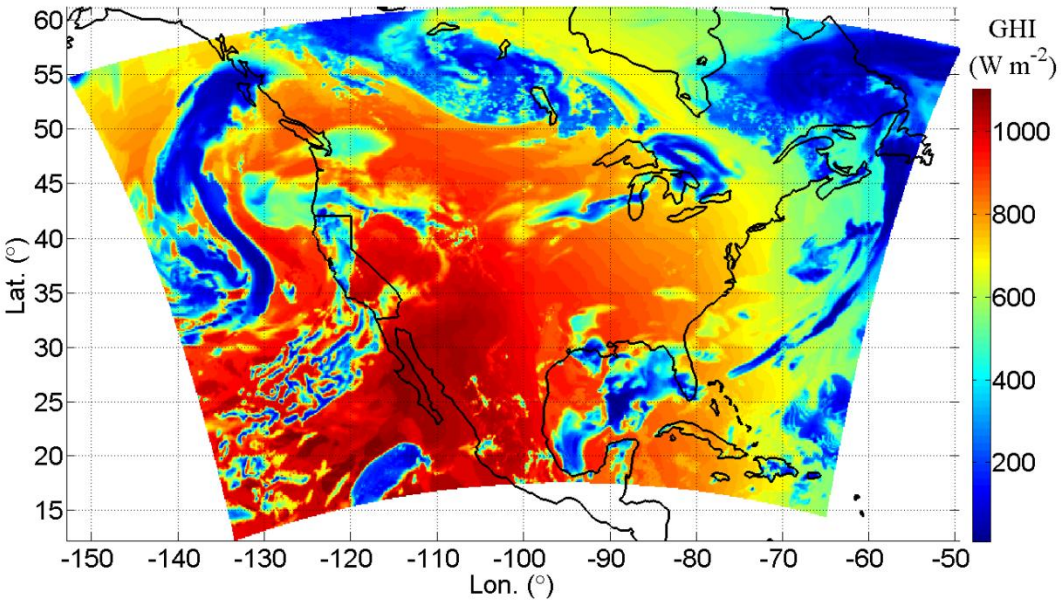


Fig. 1.3: NAM GHI forecast (W m^{-2}) for 4/10/2010 at 2000 UTC for the NAM domain over North America.

For solar forecasting, the prediction of clouds and irradiance at the surface is critical. In NWP, cloud dynamics are predicted via the microphysics parameterization. This physics module calculates the tendencies of each water specie, including transport and phase change. In the operational models, the number of water species is limited (e.g. within the NAM there are only two water species: water vapor and a single condensate variable representing cloud water, cloud ice, rain, graupel, and snow). However, using the Weather Research and Forecasting (WRF) model, more complicated microphysics parameterizations are available which prognostically predict the mixing ratio and number concentration for all water species.

In NWP, GHI is a non-native forecast variable that is primarily used to drive the surface energy budget. To calculate GHI, NWP use columnar radiative transfer models (RTMs) that assume that the primary source of radiative absorption, reflection, and scattering in the atmosphere is from concentrations of large particles such as water vapor and clouds. In general, cloud optical properties, such as optical depth and albedo, are calculated from prognostic numerical variables such as cloud water mixing ratio, temperature, and pressure (Stephens, 1978, Stephens, 1984). Additionally, the effect of background atmospheric constituents such as carbon dioxide, ozone, methane, and aerosols is calculated based on climatological look-up tables. Simple RTM like the new Goddard (Chou and Suarez, 1999, Chou and Suarez, 2001) or the Eta Geophysical Fluid Dynamics Laboratory shortwave model (GFDL-SW, Lacis and Hansen, 1974) assume that optical properties are horizontally and spectrally homogeneous. Using the two-stream adding method and assuming a surface albedo, radiative transmission, absorption, and reflection are calculated for each layer and surface irradiance prescribed. However, broadband assumptions for radiative properties are incomplete. Water vapor, for instance, absorbs radiation in narrow bands (such as 900 nm) and is largely transparent in others. To account for the spectral dependence of the radiative absorption, reflection, and transmission coefficients, line-by-line (LBLRTM, Clough *et al*., 1992) and correlated-*k* (rapid radiative transfer model, RRTM, Mlawer and Clough, 1997, Mlawer, *et al*., 1997) radiative transfer models have been developed and implemented in many NWP. Additionally, RTMs are responsible for calculating the effect of long-wave radiation. Particularly for marine-layer stratocumulus, long-wave cooling at the cloud top drives cloud dynamics. As such, its accurate prediction is critical to accurate cloud and solar irradiance forecasts. Lastly, since RTM are computationally expensive, they are called infrequently; rarely are RTM called more often than every 5 minutes.

Additionally, several other physics parameterizations affect simulated cloud fields. Since horizontal grid resolutions are small, sub-grid scale convection is unresolved. To increase

vertical mixing, cumulus parameterizations are employed. In the lower atmosphere, turbulent mixing propagates energy and moisture from the surface throughout the planetary boundary layer (PBL). However, due to the inviscid assumption and coarse vertical discretizations, NWP resolve no turbulent mixing. To account for this, turbulent production, dissipation, and transport are parameterized via the PBL scheme. Typically, turbulent kinetic energy (TKE) is calculated as a function of the vertical gradients of temperature and velocity (Nakanishi and Niino, 2006) and can be customized through the modification of several mixing lengths (L_T, L_B, L_S). Since horizontal gradients are orders of magnitude smaller than vertical, horizontal turbulent mixing is ignored. The PBL is coupled to the surface through sensible and latent heat fluxes. These are calculated using a land-surface model (LSM) such as the six-layer Rapid Update Cycle Land-Surface Model (RUC-LSM, Smirnova *et al.*, 1997) which is responsible for maintaining the surface energy and moisture budgets. The interaction between the surface energy budget and cloud formation/dissipation will be discussed at length in Chapter 6. For further information, an overview of the operationally available NWP and their accuracy for predicting solar irradiance is available in Chapter 3.

1.4 NWP Error Sources

Despite its advantages, NWP is systematically erroneous for solar irradiance forecasting (Chapter 3). Generally, model error can be divided into three primary sources: Insufficient model resolution, inaccurate physics parameterizations, and poor initial or boundary conditions. By addressing each of these sources of error, model performance and forecast accuracy can be improved.

Since the governing equations are discretized, their numerical representations are inexact. Spatially, NWP use at least 2nd order spatial discretizations (Skamarock *et al.*¸ 2008) to represent the divergence and gradient terms of the Euler equations. As such, their accuracy is limited by

$1/(\Delta x)^3$, where Δx is the horizontal resolution. For WRF, the maximum spatial discretization scheme is 6th order. Similarly, temporal discretizations are limited by $1/(\Delta t)^{n+1}$ where n is the order of the integration scheme and Δt is the time step size. Using a third-order Runga-Kutta scheme for numerically integration, WRF is accurate to $1/(\Delta t)^4$. Δt, however, is also limited by the horizontal discretization size via the Courant-Freidrichs-Lewy (CFL) criterion (Eq. 1.2).

$$u\frac{\Delta t}{\Delta x} \leq CFL \qquad \text{Eq. 1.2}$$

Conceptually, the speed of advection (u) multiplied by the time step size (Δt) cannot exceed the horizontal discretization size (Δx) to maintain numerically stability. Practically, smaller CFL criterions result in more accurate results. To increase the accuracy of the spatial and temporal discretization schemes, finer resolutions (Δx and Δt) can be used.

In addition to reducing numerical error, finer resolutions generally result in more accurate physical representations in NWP. For instance, for identical forcing conditions, near-surface wind velocities are largely dependent on topography. Coarse-scale NWP use spatially averaged topography that makes it impossible to accurately resolve local wind vectors. Additionally, vertical mixing is better resolved at finer resolutions, making NWP less reliant on convective physics parameterizations. For solar forecasting, it was previously found that the minimum cloud size resolved by WRF is directly related to the horizontal discretization size (Eq. 1.3, Mathiesen *et al.*, 2013b).

$$\Delta x_{Cloud,Min.} \approx 5 \cdot \Delta x \qquad \text{Eq. 1.3}$$

Similarly, vertical resolution plays an important role in forecast accuracy, especially for solar forecasting. In general, finer vertical resolution results in more accurate cloud field simulations (Tselioudis and Jakob, 2002, Mathiesen *et al.*, 2013b) due to better representation of vertical mixing. This is especially true for forecasts in which low-altitude clouds are expected. Overall, however, resolution errors, especially those related to the accuracy of the discretization scheme

are lower than errors from inaccurate physics parameterizations or poor initial/boundary conditions.

Since NWP physics parameterizations are not exact mathematical representations of sub-grid scale processes, they too introduce error into the forecast. There are five primary physics models in NWP: Microphysics, radiative transfer (RTM), cumulus (convection), land-surface (LSM), and the planetary boundary layer (PBL, Section 1.3). Within each are multiple relationships that are derived from inexact empirical fits with data or high-resolution large eddy simulation (LES) or direct numerical simulation (DNS) modeling. For instance, turbulence in the PBL is parameterized as a function of mixing length, stability function, and the vertical gradient of temperature or wind velocity. Even if temperature and wind-velocity profiles are perfectly simulated, the empirically-derived stability functions and mixing lengths result in imperfect TKE calculations. Subsequent time-steps would have incorrect mixing which negatively influence the temperature and wind-velocity profiles. This feedback results in errors that grow with time. Similarly, cloud optical properties are parameterized based on the cloud water mixing ratio, temperature, and pressure. Since this is inexact, the amount of radiation reaching the surface cannot be perfect, which subsequently influences the surface heat budget and the formation/dissipation of cloud cover. Previously, Otkin and Greenwald (2008) documented how cloud field simulations change based on the choice of physics parameterization. Additionally, Lopez-Coto *et al.* (2014a) performed a sensitivity analysis of the different physics parameterizations and determined that the cumulus parameterization and RTM were the two most influential parameterizations on clouds and GHI.

Lastly, the largest source of NWP error is from the inaccurate specification of the initial and boundary conditions. For non-global NWP, initial and boundary conditions are derived from large-scale NWP models. As such, parent-model error will be inherited by the smaller-scale NWP. To minimize this error source, observation data can be assimilated into the initial

conditions. Data assimilation is the specification of model initial conditions using the optimal combination of coarse-scale model output and observations. For instance, the NAM uses three-dimension variational (3DVAR) grid-point statistical interpolation (GSI, Rogers *et al.*, 2009) to assimilate temperature, pressure, relative humidity, and wind magnitudes/directions as determined from radiosonde, satellite, and other observations (Wu *et al.*, 2002). However, since most operational data-assimilation techniques omit cloud observations, benefits of data assimilation for cloud-cover and irradiance forecasting are unknown. Notably, the Rapid Update Cycle (RUC, Benjamin *et al.*, 2004a) uses a cloud-analysis system to assimilate cloud observations into the model initial conditions. In this system, satellite imagery, radar data, and local cloud cover reports are used to construct a three-dimensional observed cloud field matrix. Clouds are built into the initial conditions by directly modifying the model hydrometeors (cloud and water mixing ratios) and the state variables which support them (Benjamin *et al.* 2002, Benjamin *et al*., 2004b, Weygandt *et al.*, 2006, and Hu *et al.*, 2007). Similar systems (Albers *et al.*, 1996) are in use in the Center for Analysis and Prediction of Storms' (CAPS) Advanced Regional Prediction System (ARPS, Xue *et al.*, 2003).

Alternatively, ensemble forecasting can be used to mitigate initialization error. Generally, ensemble forecasts are created by running multiple iterations of a forecast model, each with independently perturbed initial conditions. Simulation of the entire ensemble produces a diverse set of solutions that is representative of the model uncertainty (Toth and Kalnay, 1993). Generally, the combination of ensemble members produces a more accurate forecast than any single deterministic member (Lopez-Coto *et al*., 2014b).

1.5 Project Overview

The goal of this study is to identify and address the primary weaknesses of the operational numerical weather prediction models for solar irradiance forecasting. In doing so,

this study will lay the foundation for the creation of a new numerical forecasting system that is specifically designed for cloud prediction in sub-tropical coastal regions (WRF-SRAF). Three advanced error mitigation techniques will be employed: Statistical correction techniques, data-assimilation methods, and ensemble forecasting. Overall, this system will outperform the available NWP and be implemented operationally to inform energy deployment decisions in San Diego County.

First, the meteorological conditions of San Diego County are discussed (Chapter 2). Particularly, the climatology, formation, and dissipation of marine layer stratocumulus (MLS) clouds are investigated. Using several conceptual models (Leipper, 1948, Lilly, 1968), the structure of MLS clouds is reviewed. Furthermore, using the simple mixed-layer model an analytical expression for cloud dissipation rate is derived. Later (Chapter 6), this expression serves as the basis for the ensemble portion of the WRF-SRAF system.

Next, the operational NWP and their accuracy for solar irradiance forecasting are investigated (Chapter 3). Specifically, the NAM, Global Forecast System (GFS), and European Centre for Medium Range Weather Forecasts (ECWMF) models are introduced. For solar irradiance forecasting, a comprehensive literature review of previous studies is provided. Furthermore, NAM, GFS, and ECMWF irradiance forecasts are validated for the high-accuracy Surface Radiation Budget Network (SURFRAD) across the continental United States. In general, it is shown that the operational NWP over-predict irradiance for nearly all locations and meteorological conditions. This error is consistent and systematic; the frequency of cloud cover is under-predicted for 20% of observations. Furthermore, this error is spatially dependent and generally exacerbated in regions of frequent cloud cover. Compared against the California Irrigation Management Information System (CIMIS) pyranometer network and SolarAnywhere (SolarAnywhere, 2013) irradiance data, NAM forecasts have mean bias errors (MBE) 100 W m^{-2}

higher within 30 km of the coast. This error is attributed to the frequent MLS clouds that are observed in the region.

To improve forecast accuracy in the operational models, two statistical post-processing techniques are introduced (Chapter 4). First, model-output-statistics (MOS) is used to bias-correct the NAM, GFS, and ECMWF irradiance forecasts (Lorenz *et al*¸ 2009). Related to historical MBE by solar zenith angle (SZA) and forecast clear sky index (kt^*), a dynamic function is calculated and applied. For out of sample forecasts, this method eliminated MBE and reduced root mean square error (RMSE) by up to 26.1 W m^{-2}. Second, a regime-based method is employed to assign forecast uncertainty based on the expected meteorological conditions. Since MLS conditions are more common for on-shore geostrophic flow, NWP are historically less accurate. Therefore, forecast uncertainty can be directly related to the geostrophic wind direction. Using this principle, uncertainty intervals were assigned to NAM forecasts for May and June of 2011. Overall, the uncertainty interval contained 80.4% of observations and interval width was reduced when compared to similar methods.

However, statistical corrections do not address the fundamental error sources within NWP. To further improve numerical irradiance forecasting, a new, high-resolution, cloud-assimilating NWP model is developed and tested at the University of California, San Diego (UCSD) for solar irradiance forecasting (WRF-CLDDA, Chapter 5). Using fine spatial resolution, physics parameterizations that promote cloud-cover formation, and a cloud-assimilation system, this model is specifically designed to minimize the errors typically associated with NWP irradiance forecasts. Using WRF-CLDDA, irradiance forecasts are produced for the May/June 2011 and validated against the dense UCSD pyranometer network. Additionally, the ability of WRF-CLDDA to resolve detailed, high-resolution cloud fields is tested by comparing forecast irradiance variability, expressed as a ramp-rate distribution, to observed variability. Overall, it is shown that clouds are successfully populated into the initial

conditions and that WRF-CLDDA irradiance forecasts are significantly more accurate than the NAM, especially during marine layer cloud conditions.

Finally, a WRF-based ensemble forecasting system is established (Chapter 6) that corrects model bias and characterizes the uncertainty in marine layer stratocumulus (MLS) dissipation rate to produce a dispersive set of irradiance signals useful for solar power forecasting. Using a two-dimensional idealized WRF configuration, the cloud dissipation model (Chapter 2) is validated for a variety of surface conditions, such as temperature and soil moisture. Additionally, MLS dissipation timing uncertainty is expressed as a function of the soil moisture and used to produce forecasts for 30 days where MLS clouds were observed. Validated using SolarAnywhere satellite solar irradiance data, it is shown that the median ensemble member (P_{50}) improves coastal irradiance forecasts by up to 25 W m^{-2} and reduces the dissipation timing bias by 0.5 hours in coastal areas.

Together, the collection of advanced numerical techniques discussed in this study form the basis of the comprehensive numerical solar forecasting system at UCSD (WRF-SRAF). Operationally, three surface-ensemble members in addition to a single cloud-assimilation member are running at UCSD. Furthermore, other studies (Lopez-Coto *et al.*, 2014b) have explored methods for combining the ensemble suite (both statistically corrected and unaltered) to produce the ideal forecast. Overall, this system provides vital information that is critical for making decisions on the San Diego County electric grid.

Chapter 2 Marine Layer Meteorology

2.1 Marine Layer Stratocumulus Overview

In coastal California, the dominant weather features affecting solar irradiance at the surface are marine layer stratocumulus clouds (MLS). Generally, these ocean-bound cloud systems are uniformly thick and spatially expansive while over land their extent is limited by topography. Since their dissipation is spatially correlated, large positive irradiance ramps can occur simultaneously over large areas, making their prediction essential for regions of high-density PV.

The definitive characteristic of MLS is the presence of an atmospheric temperature inversion. Typically, temperature decreases with altitude at a rate of approximately 6.5 K km^{-1}. Defined as an *increase* in temperature with altitude, temperature inversions are stable atmospheric structures that inhibit mixing across their interface. As such, temperature inversions confine moist, oceanic air near the surface and restrict mixing with dry, warm air aloft. Without a temperature inversion, dry air aloft mixes downward and prevents the formation of cloud cover. In coastal California, summertime temperature inversions are common and historically have been known to be related to the presence of low-level cloud cover (Blake, 1928). Marine temperature inversions are formed when the combination of the North Pacific High, the North American Monsoon (low pressure center in northern Mexico), and descending Hadley circulations create strong atmospheric subsidence. Under these synoptic conditions, the high-altitude geostrophic wind is north-easterly in California and drive warm, dry air to sea. Within the descending air mass, atmospheric pressure increases and adiabatic heating warms the air. At the ocean's surface, coastal upwelling results in relatively cold surface temperatures that cool the lower atmosphere. In conjunction with the warm subsiding air mass, a temperature inversion is formed. As the synoptic pressure patterns evolve and subsidence weakens or strengthens, the height of the

temperature inversion will increase or decrease (Leipper, 1948, Leipper, 1994 and Pilié *et al*., 1979).

Marine layer clouds form when moist air near the ocean surface is mixed vertically (Pilié *et al.*, 1979) to the temperature inversion. As the air rises, it expands and cools. Consequently, the saturation water vapor mixing ratio (q_s, Eq. 2.1) is reduced and relative humidity approaches 100%. If the temperature inversion is above the level at which water vapor condenses (the lifting condensation level, LCL) marine layer clouds will form. Overall, the altitude of the temperature inversion determines the altitude and thickness of the clouds.

$$q_s = \varepsilon \frac{e_s}{P - e_s} \qquad \text{Eq. 2.1}$$

Here, P is pressure, ε is the ratio of the gas constants of moist and dry air, and e_s is the saturation vapor pressure as defined by the Clausius-Clapeyron Equation (Eq. 2.2, in hPa) where L_v is the latent heat of vaporization, R_v is the gas constant for moist air, and T is the air temperature in K.

$$e_s = 6.11 \exp\left[-\frac{L_v}{R_v}\left(\frac{1}{277.16} - \frac{1}{T} \right) \right] \qquad \text{Eq. 2.2}$$

Below the temperature inversion, turbulent mixing is primarily driven by buoyant production. Though shear generated turbulence is significant near the surface, typical Monin-Obhukov lengths are much shorter than usual inversion altitudes. As such, shear turbulent production alone is insufficient to vertically mix the cloud layer (Lilly, 1968). Instead, buoyant production, in particular, cloud-top radiative cooling, drives the mixing below the temperature inversion (Lilly, 1968, Wood, 2012). At the cloud-top, a net loss in longwave radiation cools the layer, resulting in strong negative buoyancy that sinks air parcels to the surface where moisture is absorbed. Displaced by sinking air structures, moist air is driven upward, transporting moisture to the cloud layer. This coherent turbulent structure couples the cloud to the surface and

promotes the well-mixed conditions in the boundary layer that forms the basis of the mixed-layer theory for stratocumulus clouds (Lilly, 1968, Paluch and Lenschow, 1991, Chapter 2.4). Similarly, a reversed but smaller effect occurs at the cloud base due to radiative heating from the Earth's surface and the latent heat release from condensation (Cotton *et al.*, 2011). A schematic of these processes is presented in Fig. 2.1.

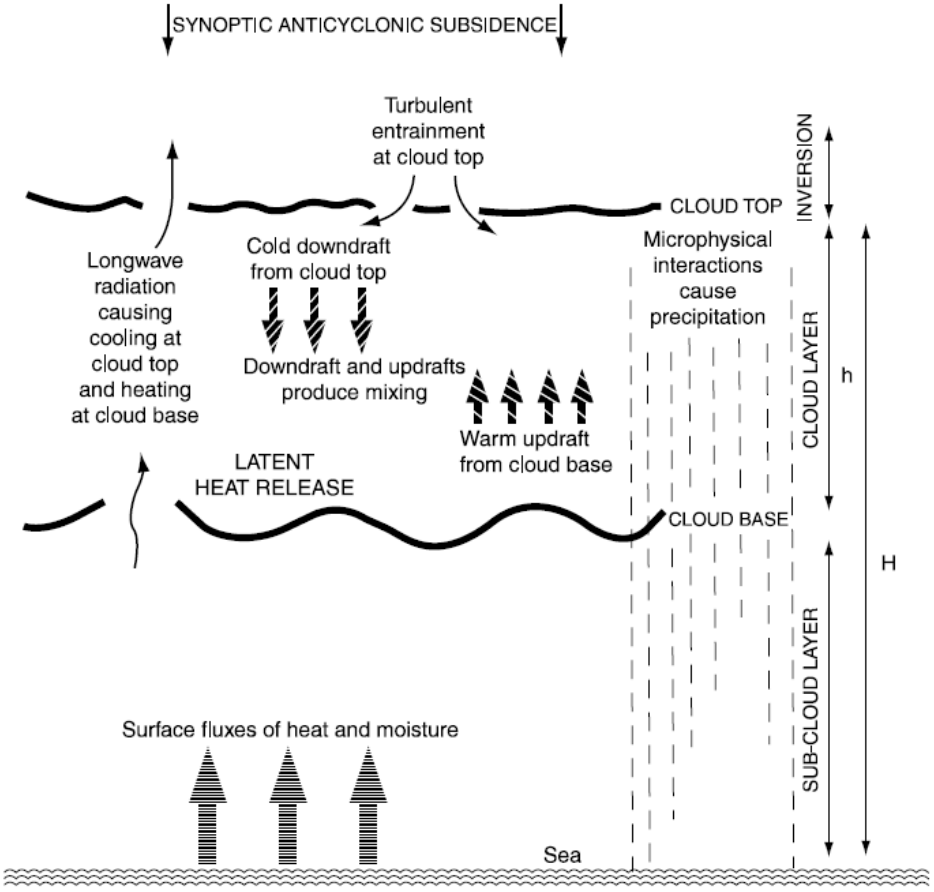


Fig. 2.1: A schematic depicting the formation of marine layer stratocumulus clouds (from Bennetts *et al.*, 1986).

MLS clouds observe a consistent diurnal pattern. Shortly before sunrise, spatial extent and cloud water content is at a maximum (Rozendaal *et al.*, 1995, Wood, 2012). Over land, their extent is limited by topography; MLS clouds will only occur in areas with elevations below the temperature inversion (Schwartz *et al.*, 2012). As such, their concentration is greatest near the

coast, occurring in over 70% of summer mornings. After sunrise, short-wave absorption within the cloud layer reduces the net cooling effect at the cloud top. As buoyant turbulent production at the cloud top decreases, sinking air parcels no longer reach the surface and the cloud becomes decoupled (Turton and Nicholls, 1987, Cotton *et al.*, 2011). Over the ocean, the moisture supply from the surface can no longer reach the cloud and dissipation occurs. Additionally, short-wave absorption by water vapor enhances heating within the cloud layer and intensifies cloud dissipation (Wood, 2012). Over land, however, surface buoyant production is as large as cloud-generated turbulence (Atkinson and Zhang, 1996, Wood, 2012). After sunrise, heat is efficiently transported from the warm surface throughout the PBL regardless of cloud-top turbulent production. As the PBL warms, the saturation water vapor mixing ratio increases and cloud water mixing ratio decreases (Tjernström and Rogers, 1995).

There are several other mechanisms for which decoupling can occur (Nicholls, 1984). First, buoyant fluxes may simply decrease due a change in the temperature differential between the air and the ocean surface, preventing a transfer of moisture from the surface to the lowest levels of the atmosphere. Second, if precipitation occurs, some falling water droplets will inevitably evaporate, absorbing heat from the lower atmosphere and reducing air temperature. The net cooling effect in the lower atmosphere has a stabilizing effect which reduces vertical mixing. Lastly, if a significant amount of warm, dry air is entrained, buoyancy will be reduced and cloud cover dissipated.



Fig. 2.2: Example of a distinct Catalina Eddy event and its effect on MLS in southern California. The satellite image is taken from Mass and Albright (1989).

Several other meteorological factors influence the thickness and location of marine layer cloud cover. Most notably, the strength and position of the Catalina Eddy (CE) can influence cloud cover in the southern California bight (Fig. 2.2). In Fig. 2.2, a distinct CE and its affect on MLS is visible off the southern California coast. Here, southerly winds along the coast pull cloud cover northward. CE occur when strong northerly flow develops off-shore of Point Conception. Due to the considerable size of the Santa Ynez Mountains at Point Conception, the northerly flow creates an area of localized low pressure on their leeward side (Bosart, 1983) resulting in a positive pressure gradient between Point Conception and San Diego. The CE is strongest when the northerly flow off shore of Point Conception is enhanced by a low-pressure center over the western United States. Since the San Diego mountain ranges (east of the coast by ~30 km) prevent geostrophic balance from occurring, air flows directly from regions of high (San Diego) to low (Point Conception) pressure and southerly winds appear (Mass and Albright, 1989).

In general, CE events are characterized by ageostrophic southerly flows at the San Diego coast. Often, this corresponds to a lifting of the marine temperature inversion and a subsequent thickening of coastal clouds. Occasionally, stratocumulus clouds will be advected northward along the coast while at-sea conditions remain clear, resulting in a narrow band of coastal cloud cover (sometimes referred to as a 'coastal surge'). The pressure gradient and subsequent winds are generally largest during the night and early morning hours. During the day, when the land-sea thermal circulations force the local flow, the wind pattern of the CE can be significantly disrupted (Mass and Albright, 1989). Similar effects can be seen in cases of coastally trapped disturbances (CTDs, Bond *et al.*, 1996, Skamarock *et al.*, 2002) which are general coastal wind reversals that are not specifically due to the CE. For both CTD and the CE, the local wind conditions affect mixing, low-level convergence, and the thermodynamic properties of air that influence cloud characteristics (Thompson and Burk, 2005).

2.2 Climatology

At UCSD, marine layer cloud cover is common for morning hours between May and September. Before 08 PST in June, for instance, observed irradiances are less than 30% of clear sky ($GHI_{CSK,}$ Fig. 2.3). By 11 PST for all months, however, marine layer cloud cover has completely dissipated and observed irradiance is larger than 90% of GHI_{CSK}. Commonly, in summer, MLS return in the evening (> 16 PST) as atmospheric temperatures cool. Furthermore, MLS dissipation time is related to coastal distance (Fig. 2.4). Furthest inland, MLS clouds dissipate before 8 PST. As time contours are generally constant with coastal distance, it can be concluded that MLS dissipation is spatially correlated, essentially moving as a coherent line towards the coast.

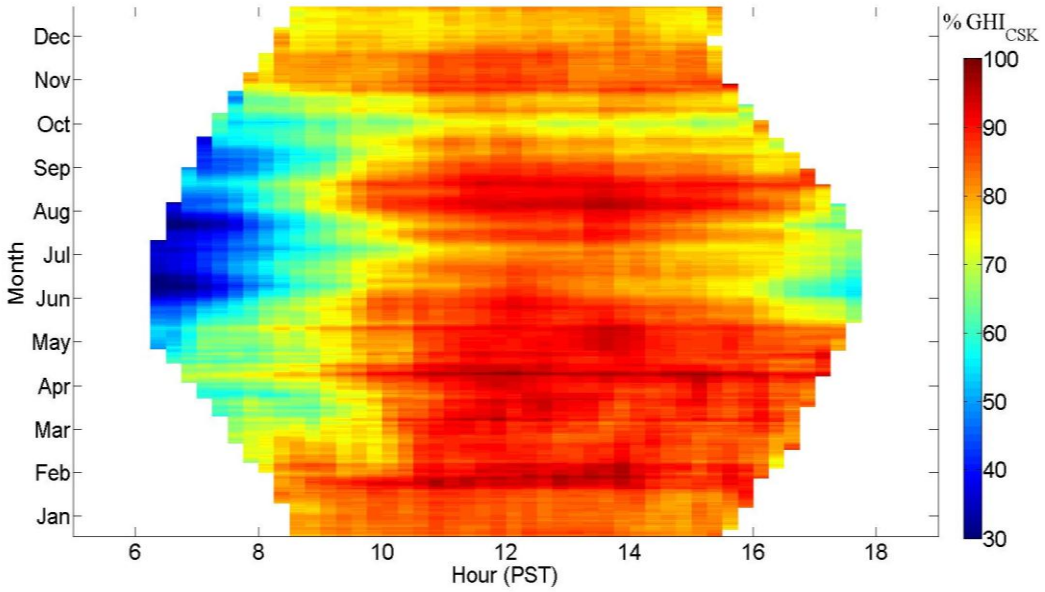


Fig. 2.3: Normalized GHI observations (% of instantaneous clear sky irradiance) at the University of California, San Diego (-117.23° W, 32.88° N, approximately 1 km from the Pacific Ocean). Observed irradiance is lowest during the mornings in the months of May-September corresponding with the occurrence of marine layer stratocumulus clouds.

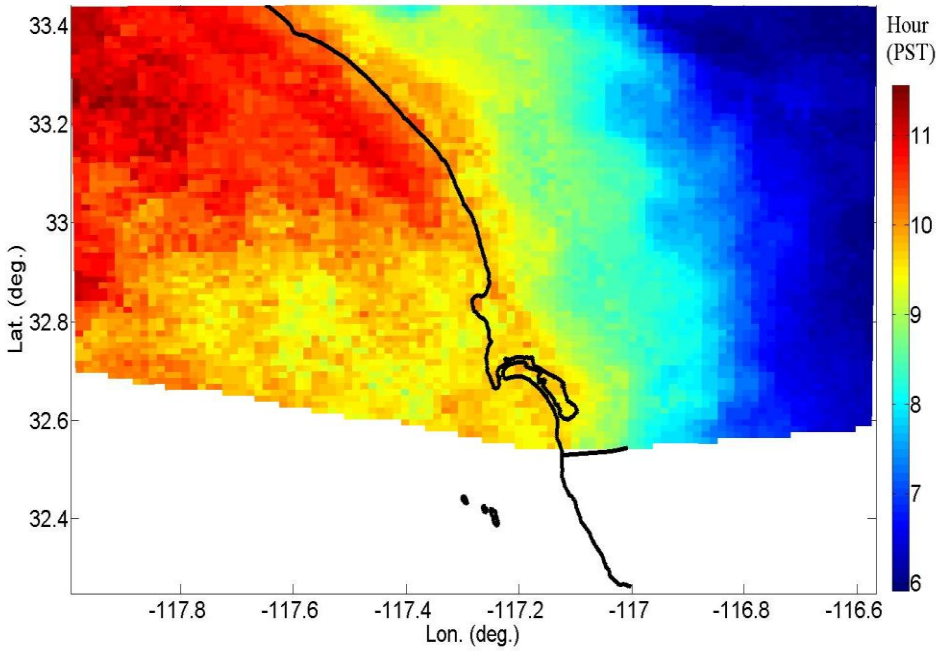


Fig. 2.4: Average MLS dissipation time as measured by SolarAnywhere for days in which MLS clouds were observed in May and June, 2011.

2.3 Leipper Cycle

The Leipper cycle is simplified model describing the evolution of fog and marine layer stratocumulus on the California coast. As previously described by Leipper (1948, 1994, 1995) and Pilié *et al.* (1979), the presence of marine layer fog and stratocumulus systems can be predicted by the boundary layer inversion height and synoptic atmospheric flow conditions. Leipper describes the formation of fog and stratocumulus to occur in several phases. First, easterly (off-shore) winds are generated by a strong high pressure center over the Pacific Northwest. During this period, flow emanates from mountainous inland regions and drives dry, warm air to sea. Atmospheric subsidence (downward vertical motion) is strong and skies are generally clear. As the high pressure center shifts inland, however, easterly winds and subsidence weaken. Off the coast, the previously warm air is significantly cooled by the ocean surface, creating a strong temperature inversion (increase of temperature with height) near the surface. Under these conditions, marine fog is likely to form. After formation, fog-top radiation cooling produces internal instabilities which promote mixing. This results in fog thickening and an increase in the depth of the marine layer. Combined with weakened subsidence, local mixing and entrainment extends fog vertically, eventually resulting in MLS conditions. Finally, clear conditions and offshore flow return as a new high-pressure system centers over northern California.

The basic premise of the Leipper cycle is that MLS clouds are more likely to form under on-shore (westerly) flow conditions while off-shore (easterly) winds generally result in clear skies in California. Using this tenet, regime-based statistical uncertainty functions can be created (Chapter 4).

2.4 Mixed-Layer Cloud Dissipation Model

Within a well-mixed layer, the liquid water potential temperature (θ_L) and the total water mixing ratio (q_T, solid black line in Fig. 2.5) are constant with height. Below the cloud layer, the water vapor mixing ratio (q_v, solid blue line) is equal to q_T and liquid water mixing ratio (q_L, shaded-lined area) is zero. Within the cloud layer, however, water vapor is at saturation ($q_v = q_S$) and $q_L = q_T - q_S$. In general, temperature and q_s decrease with altitude. Correspondingly, q_L increases within the cloud layer and is largest at the cloud top. Vertically integrating q_L yields the total amount of liquid water in the cloud, often called liquid water path (LWP).

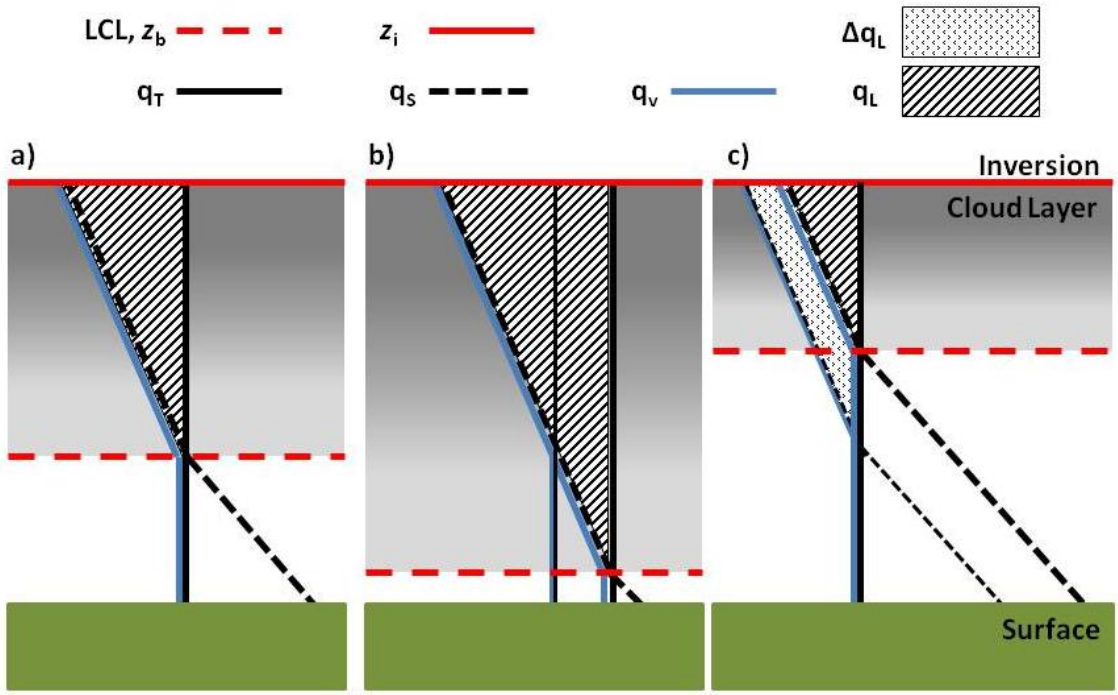


Fig. 2.5: Schematic of water mixing ratios within the well-mixed layer (a) showing total water mixing ratio (q_T, solid black line), saturation mixing ratio (q_S, dashed black line), water vapor mixing ratio (q_v, solid blue line), liquid (cloud) water mixing ratio (q_L, shaded-lined area), lifting condensation level (LCL, z_b, red dashed line) and temperature inversion (z_i, red solid line). Fig. 2.5b shows the effect of an upward latent heat flux (Q_E) on the cloud layer (q_T increases) while Fig. 2.5c shows how an upward sensible heat flux (Q_H) influences the cloud layer (q_S decreases). In b and c the original q_S and q_T are shown as thin black lines and the original q_v is a thin blue line.

A general relationship for the cloud dissipation rate within the well-mixed layer can be analytically derived. Assuming that the saturation and liquid-water mixing ratios vary linearly with height (Nicholls, 1984), the vertically averaged q_L in the cloud (designated as $\langle q_L \rangle$) is equal to half the value of q_L at cloud top (Eq. 2.3).

$$\langle q_L \rangle = \frac{1}{2} q_L(z_i) = \frac{1}{2}(q_T - q_S(z_i)) \quad \text{Eq. 2.3}$$

Multiplying Eq. 2.3 by cloud thickness $z_i - z_b$, where z_i and z_b are the heights of cloud top and cloud base, respectively, results in the LWP (Eq. 2.4).

$$LWP = \frac{1}{2}(z_i - z_b)(q_T - q_S(z_i)) \quad \text{Eq. 2.4}$$

Taking the time-derivative of Eq. 2.4 gives the change in LWP with respect to time (Eq. 2.5).

$$\frac{\partial LWP}{\partial t} = \frac{1}{2}(z_i - z_b)\left[\frac{\partial q_T}{\partial t} - \frac{\partial q(z_i)}{\partial t}\right] - \frac{1}{2}\frac{\partial z_b}{\partial t}[q_T - q_S(z_i)] \quad \text{Eq. 2.5}$$

Here, it is assumed that the cloud top height (inversion base height), z_i, does not change with time. Eq. 2.5 can further be partitioned by its primary components (Eq. 2.6, Eq. 2.7, and Eq. 2.8).

$$\frac{1}{2}\frac{\partial q_T}{\partial t}(z_i - z_b) \quad \text{Eq. 2.6}$$

$$-\frac{1}{2}\frac{\partial q_S(z_i)}{\partial t}(z_i - z_b) \quad \text{Eq. 2.7}$$

$$-\frac{1}{2}\frac{\partial z_b}{\partial t}[q_T - q_s(z_i)] \quad \text{Eq. 2.8}$$

Here, Eq. 2.6 represents the change in LWP due to a change in total water mixing ratio (q_T) within the cloud ($\partial q_T\, \partial t^{-1}$, Fig. 2.5b). The change is the sum of all sources (e.g. advection, the surface latent heat flux) and sinks (e.g. precipitation, advection, dry-air entrainment) of water in the atmosphere (Fig. 6.4c/d, later). Eq. 2.7 is the change in LWP due to a change in q_S in the

cloud layer ($\partial q_S\ \partial t^{-1}$) as temperature varies. For example, as q_S increases with temperature, LWP decreases (e.g. Fig. 2.5c). Similar to Eq. 2.6, Eq. 2.7 represents the change in LWP due to all sources of temperature change (e.g. advection, radiative cooling, phase-change latent heating, etc., Fig. 6.4a/b, later). Finally, Eq. 2.8 describes the change in LWP due to a change in cloud geometric thickness. Since it is assumed that z_i does not vary with time, Eq. 2.8 results only from a change in cloud base height. As cloud base rises, LWP will decrease.

Assuming the vertical gradient of saturation water mixing ratio does not change with time, a simple relationship for $\partial z_b\ \partial t^{-1}$ is obtained (Eq. 2.9).

$$\frac{\partial z_b}{\partial t} = \frac{\dfrac{\partial q_T}{\partial t} - \dfrac{\partial q_s(z_i)}{\partial t}}{\dfrac{dq_s}{dz}} \qquad \text{Eq. 2.9}$$

As Fig. 2.5 indicates, a change in total water- or saturation vapor mixing ratio produces a change in cloud base height according to the vertical slope of q_S ($dq_S\ dz^{-1}$). The vertical slope of q_S in the cloud layer may be expressed as Eq. 2.10 recognizing that $q_S = q_T$ at the cloud base.

$$\frac{dq_S}{dz} = \frac{q_S(z_i) - q_S(z_b)}{z_i - z_b} = \frac{q_S(z_i) - q_T}{z_i - z_b} \qquad \text{Eq. 2.10}$$

By combining Eq. 2.9 and Eq. 2.10, substituting in Eq. 2.5, and dividing by the width of the cloud layer ($z_i - z_b$) to convert back to $\langle q_L \rangle$, $\partial z_b\ \partial t^{-1}$ is eliminated to obtain Eq. 2.11.

$$\frac{\partial \langle q_L \rangle}{\partial t} = \frac{\partial q_T}{\partial t} - \frac{\partial q_s(z_i)}{\partial t} \qquad \text{Eq. 2.11}$$

Furthermore, the condition of a well-mixed PBL necessitates that the rate of change of q_L at every level in the cloud is the same as the rate of change of the vertically averaged $\langle q_L \rangle$. Since $\partial q_T\ \partial t^{-1}$ is independent of temperature, Eq. 2.11 can be expressed as Eq. 2.12.

$$\frac{\partial \langle q_L \rangle}{\partial t} = \frac{\partial q_T}{\partial t} - \frac{\partial q_s}{\partial T} \cdot \frac{\partial T}{\partial t}\bigg|_{z_i} \qquad \text{Eq. 2.12}$$

Here, $\partial T\, \partial t^{-1}$ is the rate of temperature change at cloud top and $\partial q_S\, \partial T^{-1}$ is the change in saturation mixing ratio with respect to temperature. Eq. 2.12 provides a general expression for the change in vertically averaged cloud LWP due to changes in total water content (Fig. 2.5b) and temperature (Fig. 2.5c). Outside of advection, contributions from the surface turbulent fluxes have the largest influence on cloud dissipation rate over land, as will be subsequently shown in Table 6.2. In terms of the surface fluxes, $\partial q_T\, \partial t^{-1}$ is a function of latent heat flux (Q_E) and is independent of the sensible heat flux (Q_H). The latent heat flux describes the amount of energy transferred from the surface to the atmosphere in the form of water transport and is proportional to the total evapotranspiration divided by the latent heat of vaporization for water, L_V. Assuming a vertically-averaged density ρ_B over the entire PBL (which is usually less than 1500 m deep), $\partial q_T\, \partial t^{-1}$ is expressed as Eq. 2.13.

$$\frac{\partial q_T}{\partial t} = \frac{Q_E}{L_v \rho_B z_i} \qquad \text{Eq. 2.13}$$

Since the PBL is assumed to be well mixed, water added from the surface is evenly distributed over the entire PBL and q_T is increased (solid black line in Fig. 2.5b). If q_S is constant, the rate of change of q_L equals the rate of change of q_T within the cloud layer (Eq. 2.11). Therefore, a positive surface latent heat flux delivers moisture to the PBL, increases cloud LWP, lowers the LCL (z_i, cloud base), and increases cloud lifetime (Fig. 2.5b). Conversely, a positive sensible heat flux warms the PBL, which increases q_S and the rate of cloud dissipation.

The rate of liquid water potential temperature change ($\partial \theta_L\, \partial t^{-1}$) is related to Q_H by Eq. 2.14 where c_p is the vertically-averaged specific heat for the PBL.

$$\frac{d\theta_L}{dt} = \frac{Q_H}{c_p \rho_B z_i} \qquad \text{Eq. 2.14}$$

For the unsaturated subcloud layer, the potential temperature is the same as the liquid water potential temperature. Noting that the PBL is shallow, we make the approximation that the rate of temperature change ($\partial T\, \partial t^{-1}$) is the same as the rate of potential temperature change ($\partial \theta\, \partial t^{-1}$). The rate of change of temperature in the cloud layer, however, is smaller than the rate of change of temperature in the subcloud layer. This is because evaporative cooling of cloud droplets partially offsets sensible heating of the cloud.

Temperature change in the cloud layer may be easily related to temperature change in the subcloud layer by recalling that the cloud base in a well-mixed layer always occurs at the temperature where the total water mixing ratio is equal to the saturation mixing ratio. If no water is added or removed from the PBL, sensible heating causes cloud base height to rise at a rate inversely proportional to the lapse rate. In a well-mixed layer, the lapse rate is at dry adiabatic (Γ_d) in the subcloud layer and moist adiabatic (Γ_m) in the cloud layer and can be related using Eq. 2.15 and Eq. 2.16.

$$\frac{dz_b}{dt} = \frac{1}{\Gamma_d}\frac{dT}{dt}\bigg|_{sub} = \frac{1}{\Gamma_m}\frac{dT}{dt}\bigg|_{cloud} \qquad \text{Eq. 2.15}$$

$$\frac{dT}{dt}\bigg|_{cloud} = \frac{\Gamma_m}{\Gamma_d}\frac{dT}{dt}\bigg|_{sub} \qquad \text{Eq. 2.16}$$

Here, the relatively small variation of $\partial q_S\, \partial T^{-1}$ and Γ_m with temperature is neglected. Noting that the rate of temperature change is vertically uniform within the cloud layer, Eq. 2.16 is substituted into Eq. 2.14 to obtain the relationship between sensible heat flux and the rate of change of temperature at the cloud top (Eq. 2.17).

$$\frac{dT}{dt}\bigg|_{z_i} = \frac{\Gamma_m}{\Gamma_d}\frac{Q_H}{c_p \rho_B z_i} \qquad \text{Eq. 2.17}$$

The ratio of moist to dry adiabatic lapse rates is approximately 0.5. Finally, Eq. 2.13 and Eq. 2.17 may be substituted into Eq. 2.12 to yield the total rate of change in vertically averaged liquid water mixing ratio (Eq. 2.18).

$$\left.\frac{d\langle q_L\rangle}{dt}\right|_{Sfc.} = \frac{1}{\rho_B z_i}\left[\frac{Q_E}{L_v} - \frac{Q_H}{c_p}\frac{\Gamma_m}{\Gamma_d}\frac{\partial q_S}{\partial T}\right] \qquad \text{Eq. 2.18}$$

By substituting the total turbulent energy flux ($Q_U = Q_H + Q_E$) Eq. 2.18 can be expressed as a function of Q_U and the Bowen ratio (Eq. 2.19).

$$\left.\frac{d\langle q_L\rangle}{dt}\right|_{Sfc.} = \frac{1}{\rho_B z_i} Q_U \frac{\beta}{1+\beta}\left[\frac{1}{L_v\beta} - \frac{1}{c_p}\frac{\Gamma_m}{\Gamma_d}\frac{\partial q_S}{\partial T}\right] \qquad \text{Eq. 2.19}$$

Q_U is independent of Bowen ratio and is determined by the surface energy balance. Since the energy balance must be satisfied, β essentially partitions Q_U into latent and sensible parts (ignoring the feedback between sensible heat flux, ground heat flux, and longwave radiation). As β increases, the sensible heat flux increases (last term) and results in a more negative cloud dissipation rate. Eq. 2.19 provides an analytic expression for the change in cloud water content as a function of the surface heat fluxes independent of additional factors such as the temperature change from radiative cooling, advection, and sinks of moisture such as precipitation.

2.5 Acknowledgements

Previously, section 1 and 2 have been published in Mathiesen *et al.*, 2013b and Mathiesen *et al.*, 2014. Section 3 was based off of Mathiesen *et al*, 2013a and Section 4 used material from Mathiesen *et al.*, 2014.

Chapter 3 Evaluation of Operational NWP for Solar Forecasting

This chapter discusses the operational numerical weather prediction (NWP) models and their accuracy for solar irradiance forecasting. Since these models are publicly available and easy to obtain, they form the basis of many operational forecasting systems. As such, an evaluation of their accuracy provides valuable information to many academic and private forecasting services. First, a general overview of each model is discussed. Here, model physics, discretization, and initialization techniques are discussed. Second, a literature review of previous NWP evaluations for solar forecasting is provided. Third, the NAM, GFS, and ECMWF forecasts are validated for the Surface Radiation Budget (SURFRAD) network. Finally, using the California Irrigation Management Information System (CIMIS) and SolarAnywhere satellite data, NAM irradiance forecasts are spatially validated in California. Overall, the error tendencies documented in this chapter will motivate the statistical correction methods described in Chapter 4.

3.1 Numerical Weather Prediction (NWP) Models

3.1.1 The North American Mesoscale Model (NAM)

One of several operational NWP models for the continental United States, the North American Mesoscale Model (NAM) is based on the Weather Research and Forecasting-Non-Hydrostatic Mesoscale Model (WRF-NMM) and is maintained by the National Centers for Environmental Prediction (NCEP) within the National Oceanic and Atmospheric Administration (NOAA). Covering the continental United Stations, the NAM uses 12 km horizontal resolution and 60 vertical hybrid sigma-level terrain-following coordinates. Temporally, the time step size is 30s and output is available hourly to a maximum forecast horizon of 36 hours. Additionally, the NAM forecast is available up to 84 hours ahead for a 3-hour temporal resolution. The NAM model is initialized by the NAM Data Assimilation System at 00, 06, 12, and 18 UTC daily using

observations and first-guess model output. Data is assimilated using the three-dimension variational (3DVAR) grid-point statistical interpolation (GSI) method (Rogers *et al.*, 2009). Assimilated data include temperature, pressure, relative humidity, and wind magnitudes/directions as determined from radiosonde, satellite, and other observations (Wu *et al.*, 2002). Initialized shortly before the North American sunrise, irradiance forecasts from the 12 UTC run are slightly more accurate and were exclusively used in this study. Full details of the NAM are available in Janjic *et al.*, 2010 and Janjic *et al.*, 2011.

For solar forecasting applications, the cloud microphysics, cumulus parameterization, and shortwave radiation models are especially important. NAM cloud microphysics are solved by the Ferrier microphysics scheme (Rogers *et al.*, 2001). Here, two prognostic water variables are used: water vapor and a total condensate variable. Mixed phased processes and the partitioning of the condensate into cloud water, cloud ice, rain, snow and graupel are calculated diagnostically. Additionally, vertical transport has a large impact on cloud formation. To account for sub-grid scale convective effects, shallow clouds, and resolve vertical transport, the Betts-Miller-Janjic (Janjic, 1994, and Janjic, 2000) cumulus parameterization is used. Finally, irradiance at the surface is calculated using the Geophysical Fluid Dynamics Laboratory Short Wave (GFDL-SW, Lacis and Hansen, 1974) radiative transfer model (RTM). For each vertical level, cloud radiative properties (albedo and optical depth) are parameterized based on prognostic variables such as water mixing ratios, temperature and pressure (Stephens, 1978; Stephens, 1984). Additionally, absorption and scattering by carbon dioxide and ozone are taken into account via climatological reference tables. As the RTM is computationally expensive, GHI is calculated every 120 time steps (once per hour). Since the GFDL-SW RTM is called only once per hour, the impact of intra-hour cloud cover variability on irradiance is unresolved. Lastly, since the GFDL-SW is a columnar RTM adjacent grid cells have no influence on surface irradiance. For this study, only the 12 UTC initialization time was used.

3.1.2 The Global Forecasting System (GFS)

As a global model, the GFS has worldwide coverage. Also published by NOAA through NCEP, the GFS model uses 35 km horizontal resolution and 64 vertical levels. Temporally, the time step size is 7.5 minutes. When output, however, data is spatially averaged to a resolution of 0.5° E-W by 0.5° N-S and temporally averaged to 3 hours. The 0.5° GFS is available up to 180 hours (7.5 days) ahead. Furthermore, GFS forecasts are reported as alternating 3 (1^{st}, 3^{rd}, etc. forecasts in a series) and 6-hour (2^{nd}, 4^{th}, etc.) averages. Consistent 3-hour resolution forecasts are calculated from the raw data. Every 6 hours, GFS forecasts are initialized using the Global Data Assimilation System (GDAS). Like the NAM, this system uses GSI to incorporate temperature, pressure, and relative humidity into the initial conditions. Since the GFS is a global model, periodic boundary conditions are implemented.

The SW radiative model used by the GFS is the rapid radiative transfer model (RRTM-SW, Mlawer and Clough, 1997, Mlawer, 1997). RRTM uses the correlated-*k* method to transform the spectral dependence of radiative absorption coefficients (*k*) into a continuous cumulative distribution function. The transformed space is subsequently discretized into 9 bands and characteristic *k* values calculated for each sub-interval. Hourly, a two-stream adding method is called in which radiative transfer calculations are performed independently for each sub-interval across all vertical layers. This is similar to the individual spectral-point line-by-line radiative transfer model (LBLRTM, Clough et al., 1992) calculations. Absorption effects from water vapor, ozone, oxygen, and methane are considered. Additionally, cloud optical depth, albedo, asymmetry factor, and effective particle radius contribute to layer radiative properties. Similar to the NAM, cloud properties are largely dependent on liquid water path (LWP), ice water path (IWP), temperature, pressure, and location (Slingo, 1989, Fu, 1996, Hou et al., 2002).

Additionally, the GFS uses the Simplified-Arakawa-Schubert (SAS) cumulus scheme to model sub-grid scale convection (Grell, 1993, Pan and Wu, 1995). This is a threshold-based scheme in which convection is only triggered under certain conditions. Finally, PBL turbulence is parameterized using the Medium-Range Forecast (MRF) scheme (Hong and Pan, 1996). Full details on the GFS are available online (NCEP, 2013).

3.1.3 The European Centre for Medium Range Weather Forecasts Model (ECMWF)

Like the GFS, the ECMWF is a global forecast model. Spatially, ECMWF data is available on a 0.25° E-W by 0.25° N-S grid. Temporally, ECMWF forecasts are output every 3 h up to 10 days in advance and initialized twice daily (00 UTC and 12 UTC) using 4D Variational Data Assimilation (4DVAR). Data is published as progressive averages (i.e. 3 h, 6 h, 9 h, etc.) for each series. From this, 3-hour resolution forecasts are calculated. For this study, only intra-day forecasts were considered (24-hour forecast horizon). Downward surface solar radiation data released at 12 UTC between September 1st, 2009 and August 31, 2010 were purchased.

The current operational ECMWF model contains the McRad radiation model (Morcette et al., 2007). The shortwave portion of McRad is based on RRTM. Constituents accounted for in McRad are water vapor, carbon dioxide, ozone, methane, nitrous oxide, aerosols, and various chlorofluorocarbons (CFCs). Similar to the GFDL-SW model, important forecast cloud properties are albedo and optical depth and are parameterized primarily from LWP and effective droplet radius (Slingo et al. 1989, Table 3 in Morcrette et al., 2007). From the radiative properties, a two stream adding method is used to solve the radiative model at each level, resulting in surface GHI. Cloud microphysics are based on the Tiedtke (1993) scheme. Here, six water constituents are prognostically calculated: water vapor, cloud water, cloud ice, cloud fraction, snow, and rain (ECMWF, 2012). Full details on the ECMWF model are available online (ECMWF, 2012).

3.2 Review of Previous Studies for Solar Irradiance Forecasting

Though generally more accurate than persistence or imagery based techniques, previous studies have demonstrably shown that NWP irradiance forecasts are systematically erroneous. Heinemann et al. (2006) showed that the MM5 mesoscale model can predict GHI in clear skies without mean bias error (MBE). However, this was highly dependent on cloud conditions; in overcast conditions, the MM5 model MBE was 129% (Heinemann et al., 2006). Perez et al. (2007) examined the accuracy of the National Digital Forecast Database (NDFD), a derivative of the operational NWP models published by the National Center for Environmental Prediction (NCEP). After a local correction function was applied, Perez et al. (2007) found that for 8 to 26-hour forecast horizons, the NDFD had a GHI rRMSE of 38%. This was more accurate than satellite derived forecasts for similar forecast horizons (rRMSE = 46%). Remund *et al.* (2008) found consistent under-predictions of cloud cover at three sites within the United States using three NWP sources: The National Digital Forecast Database (NDFD), the European Centre for Medium-range Weather Forecasts (ECMWF), and the Weather Research and Forecasting (WRF) model as initialized by the Global Forecasting System (GFS). Generally, mean bias errors (MBE) for day-ahead hourly forecasts were positive indicating a consistent under-prediction of cloud cover and/or cloud optical depth. Additionally, root mean square errors (RMSEs) ranged from 87 – 223 W m^{-2} and were generally smallest for the ECMWF forecast. Perez *et al.* (2010) expanded the NDFD comparison to seven ground measurement sites across the continental United States. Consistently, RMSE exceeded 150 W m^{-2} and generally increased with climatological cloudiness. Similarly, Mathiesen and Kleissl (2011) found a systematic under-prediction of cloud cover in NAM, GFS, and ECMWF irradiance forecasts. For all models, MBE exceeded 30 W m^{-2} and RMSE was larger than 110 W m^{-2}. Again, a general under-prediction of cloud cover was observed. Out of all cloudy observations, 52% of NAM, 54% of GFS, and 31% of ECMWF forecasts contained little or no clouds. Conversely, false-positive forecasts (a cloudy forecast

when clear-sky conditions are observed) were far less common, occurring in only 9% of NAM, 9% of GFS and 12% of ECMWF forecasts. Furthermore, Mathiesen *et al.* (2013a/2013b) showed that this error is exacerbated for coastal regions in California. Near the coast, where MLS clouds are common, NAM MBE was greater than 150 W m^{-2} in summer months. Inland, where clouds are infrequent, NAM MBE was less than 90 W m^{-2}.

Similar trends have been observed worldwide. Lorenz *et al.* (2009) found that the ECMWF model consistently over-predicted irradiance when compared to 200 meteorological stations in Germany. Mean bias errors (MBEs) for moderately cloudy forecast conditions were approximately 100 W m^{-2} while STDERR (the RMSE independent of MBE) exceeded 200 W m^{-2}. This error was generally attributed to the inaccurate characterization of cloud optical properties. Additionally, Pelland *et al.* (2011) found a general cloud under-prediction in Environment Canada's Global Environmental Multiscale (GEM) model; relative MBE (MBE normalized by the average observed irradiance) was 0 – 14%. Furthermore, using the Japan Meteorological Agency (JMA) mesoscale model to forecast irradiance for five stations in Japan, Ohtake *et al.* (2012) found that forecast accuracy was seasonally dependent. In winter, MBE was generally positive and errors were attributed to the inaccurate characterization of low-level stratocumulus clouds. In summer, however, the occurrence of cirrus clouds resulted in negative MBE. Moreover, Lara-Fanego *et al.* (2012) found MBE of 49 – 64 W m^{-2} for GFS driver WRF simulations in southern Spain. Finally, a comprehensive analysis of irradiance forecasts from ten models applied in a diverse set of meteorological conditions in the US, Canada, and Europe is available in Perez *et al.* (2013). Overall, these previous studies have conclusively demonstrated the limitations of the available NWP models for solar irradiance forecasting.

3.3 Evaluation of the NAM, GFS, and ECMWF for irradiance forecasting in the continental United States

This section focuses on the analysis of GHI forecasts from three operational NWP models within the continental United States (North American Model, NAM, GFS, and ECMWF). A fourth operational NWP model, the Rapid Update Cycle (RUC), was not evaluated. Here, all available operational NWP models are validated against a nationwide network of meteorological stations (Section 3.3.4) for up to 1 year. Consistent biases are shown as a function of measured and forecast clear sky index motivating the application of a MOS correction as a function of solar zenith angle and clear sky index (Chapter 4). Only intra-day (or hour-ahead) forecasts are considered since NWP forecast accuracy has been shown to be approximately constant over a 3 day horizon (Remund et al. 2008) and intra-day forecasts are relevant for energy markets.

3.3.1 SURFRAD Ground Measurement Network

Seven Surface Radiation Budget Network (SURFRAD) stations across the CONUS provide an accurate nationwide database to validate NWP forecasts. SURFRAD stations are equipped with Eppley Precision Spectral Pyranometers (PSP) (SURFRAD, 2009a) capable of measuring GHI to within ±2% (Campbell, 1992). The PSPs are calibrated through NOAA's Solar Radiation Facility. One minute GHI is reported as an average of sixty 1-sec instantaneous measurements. Due to pyranometer thermal offset, night time GHI values are generally negative (SURFRAD, 2009b). For this reason, all negative values of GHI were set to zero. Data flagged by the baseline quality control (QC) assessment function due to historically inconsistent, unphysical, and uncharacteristic data (SURFRAD, 2009b) were removed from this analysis. SURFRAD GHI data were aggregated to one hour averages for comparison with the (hourly or longer) output time-step of NWP forecasts.

3.3.2 Forecasting Methods

Fig. 3.1 depicts a sample time series of the forecast methods that will be evaluated. The most basic "forecast", *C*, is the Ineichen clear sky model (Ineichen and Perez, 2002). *C* primarily depends on location, time, and elevation. Additionally, *C* is dependent on atmospheric turbidity variations due to aerosols, ozone, and water vapor, which are input as monthly averages of the Linke turbidity from the SoDA database on an 8 km grid (Wald, 2002).

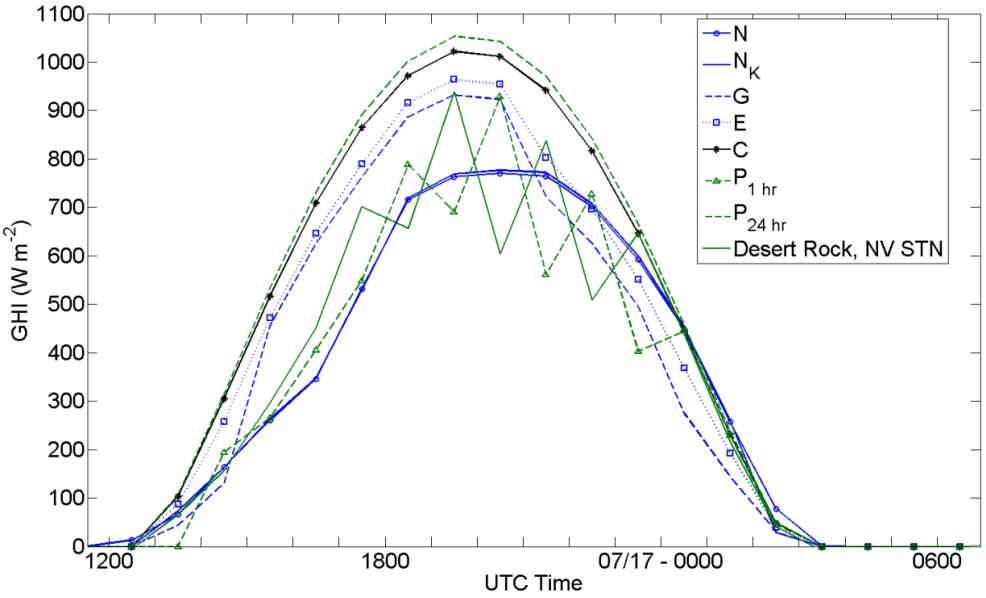


Fig. 3.1: GHI forecasts compared against Desert Rock, NV SURFRAD ground measurements on July, 17th 2010. *N*: linear interpolated NAM; N_K: clear sky index interpolated NAM; *G*: GFS three hour constant clear sky index; *E*: ECMWF three hour constant clear sky index; *P*: persistence; *C*: clear sky forecast.

The persistence forecasts, P_1 and P_{24}, assume static weather conditions. The measured clear sky index (kt_m) is defined by Eq. 1.1. P_{24} forecasts GHI by assigning the kt_m at solar noon of the previous day to the entire intra-day forecast (kt_P). P_{24} is calculated by multiplying kt_P with the clear sky model, *C*. The 1 hour persistence forecast, P_1 is calculated by multiplying kt_P (the measured clear sky index averaged over the previous hour) with *C*. In this way, P_1 is a 'best-case'

persistence forecast for hour-ahead forecasting, while P_{24} is a typical persistence forecast for day-ahead forecasting.

Forecasts originating shortly before the CONUS sunrise are the timeliest for planning intra-day power plant load-following. Thus, the only NWP forecasts considered for this study originate at 1200 UTC. As NWP forecast errors have been shown to be constant over a forecast horizon of 1 hour to 3 days (Perez et al. 2010), the results of this paper can also be considered applicable to day-ahead (i.e. next day) forecasts.

Interpolation of NWP output is necessary to temporally align NWP output and ground measurement data. Since sun position and solar zenith angle are non-linear functions of time, solar irradiance cannot be a linear or stationary process. Therefore, linear interpolation of GHI is inappropriate (*N*, Fig. 3.1). Instead, clear sky index *kt** interpolation should be used to produce a semi-stationary signal (Hansen *et al*, 2010). Since the clear sky model, *C*, is nearly linear over one hour, *N* and N_K produce essentially identical forecasts (Fig. 3.1). N_K is the physically correct forecast and will henceforth be considered the primary forecasting method for the NAM model.

For the GFS and ECMWF, GHI forecasts are *average* irradiances applicable to the entire forecast interval. 3-hour clear sky indices are calculated through Eq. 1.1 and multiplied by *C* to produce the hourly *G* and *E* forecasts. Table 3.1 compares each forecasting method for a single day forecast horizon.

Table 3.1: Comparison of the forecast timesteps over a single day. Boxes represent averaging periods of constant clear sky index kt^* (kt_m for P_1 and P_{24}). N_K is interpolated from hourly instantaneous values and assumed to apply over the entire hourly interval. The GFS provides a combination of 3 and 6-hour interval forecast, from which 3-hour forecasts can be back calculated (striped box).

UTC hour	12	13	14	15	16	17	18	19	20	21	22	23	24	1	2	3	4	5
NAM																		
GFS																		
ECMWF																		
P_1																		
P_{24}																		

3.3.3 Error Metrics

Eq. 3.1-Eq. 3.7 define error metrics used in NWP forecast evaluation: the mean bias error (MBE), mean absolute error (MAE), root mean square error (RMSE), and their relative analogues. Relative errors are obtained by using the deviation in clear sky index rather than irradiance. This provides a measure of error that is independent of time of day.

$$MBE = \frac{1}{N}\sum_{i=1}^{N}\left(GHI_{Forecast,i} - GHI_{Obs.i}\right) \quad \text{Eq. 3.1}$$

$$MAE = \frac{1}{N}\sum_{i=1}^{N}\left|GHI_{Forecast,i} - GHI_{Obs.,i}\right| \quad \text{Eq. 3.2}$$

$$RSME = \sqrt{\frac{1}{N}\sum_{i=1}^{N}\left(GHI_{Forecast,i} - GHI_{Obs.,i}\right)^2} \quad \text{Eq. 3.3}$$

$$STDERR = \sqrt{\frac{1}{N}\sum_{i=1}^{N}\left(GHI_{Forecast,i} - GHI_{Obs.,i} - MBE\right)^2} \quad \text{Eq. 3.4}$$

$$rMBE = \frac{1}{N}\sum_{i=1}^{N}\left(kt_i^* - kt_{m,i}\right) \quad \text{Eq. 3.5}$$

$$rMAE = \frac{1}{N}\sum_{i=1}^{N}\left|kt_i^* - kt_{m,i}\right| \quad \text{Eq. 3.6}$$

$$rRSME = \sqrt{\frac{1}{N}\sum_{i=1}^{N}\left(kt_i^* - kt_{m,i}\right)^2} \quad \text{Eq. 3.7}$$

$$rSTDERR = \sqrt{\frac{1}{N}\sum_{i=1}^{N}\left(kt_i^* - kt_{m,i} - rMBE\right)^2} \quad \text{Eq. 3.8}$$

3.3.4 Effect of Spatial Averaging

N_K, G, and E are spatially discrete functions for GHI. Girodo (2006) showed that spatial averaging of ECMWF output over 0.5° x 0.5° reduces the rRMSE of NWP forecasts. Here, forecast GHI for each station is calculated by taking the mean output GHI of all NWP grid points within various distances (10 km, 50 km, 100 km, and 200 km) of the ground measurement station. The mean absolute error (MAE) is not biased by large error events and is the best metric for determining the advantage of spatial averaging.

Spatial averaging of the N_K (Fig. 3.2) and G (not shown) forecasts results in a reduction in MAE. As the scale of spatial averaging increases the MAE across the majority of kt_m decreases. Generally, spatially averaging reduces the portion of the forecast error that is randomly distributed. Furthermore, averaging eliminates small spatial offsets in cloud fields that contribute to forecast error. Only for small measured clear sky indices ($kt_m < 0.25$) does MAE increase with increased spatial averaging, especially for the 200 km spatial averaging radius. Likely, this occurs because the observed cloud fields are smaller than 200 km and the spatial averaging introduces error by including forecasts that are predominantly clear. Girodo (2006) and Lorenz et al. (2009) also found reduced errors for averaging over a 100 km x 100 km square grid for the ECMWF forecast. Henceforth, only the 100 km radius spatial average will be considered for the analyses.

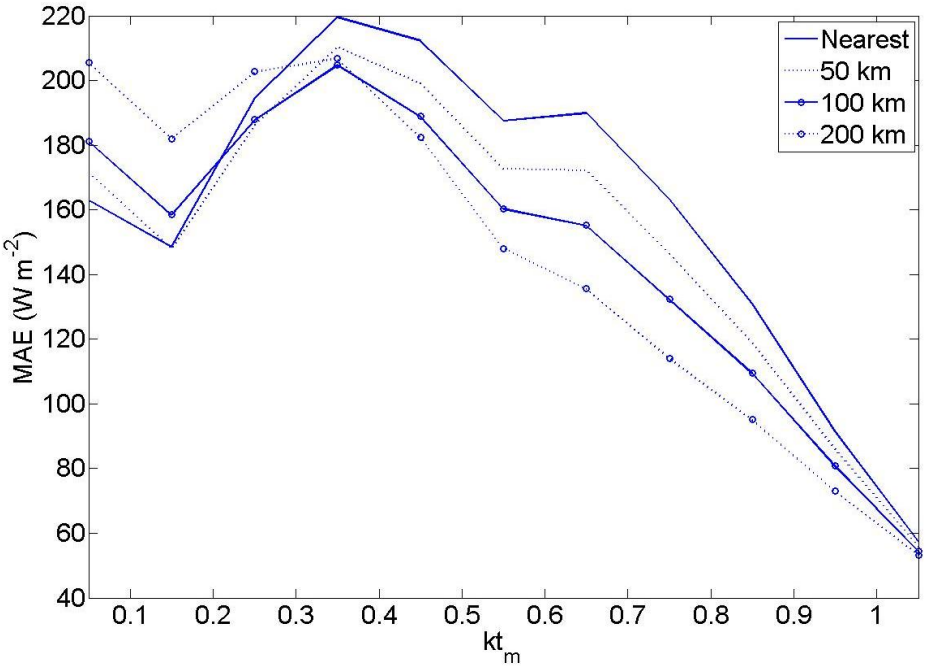


Fig. 3.2: N_K MAE (W m^{-2}) as a function of measured clear sky index (kt_m) for different averaging radii of the NAM model. 50, 100, and 200 km averaging radii correspond to approximately 80, 300, and 1250 grid points, respectively.

3.3.5 Forecast Error of N_K, G, and E

Fig. 3.3 reveals similar MBE profiles for each NWP model. Given measured clear conditions and *SZA*s near solar noon, all NWP forecasts are negatively biased by between 0 and 50 W m^{-2} (Fig. 3.3), indicating the presence of cloudy forecasts that resulted in clear periods. These results may be biased by location and season, since northern stations experience a cos(SZA)> 0.9 only for a short part of the year .

In clear skies, MBE increases with *SZA* reaching 50 W m^{-2} for cos(*SZA*) = 0.35 for N_K and approximately 0 W m^{-2} for *G* and *E*. At cos(*SZA*) < 0.4, many N_K forecasts predict up to 40% more GHI than clear sky models (kt^* = 1 to 1.4,). This over-prediction of GHI in measured clear conditions is surprising as it potentially indicates an inaccurate NWP clear sky model.

For measured cloudy conditions ($kt_m < 0.8$) and relevant *SZA* (*SZA* < 75°), N_K, *G*, and *E* are positively biased by up to 225 W m^{-2}. Positive MBEs in measured cloudy conditions ($kt_m < 0.8$) suggest that either cloudy conditions were not predicted or that the prescribed cloud optical depths or cloud cover fractions were too small.

Some of these patterns can be explained by the binary nature (either cloudy or clear) of solar forecasts. Examination of the data distribution of predicted and measured conditions (Table 3.2 with an overcast threshold of $kt = 0.8$) shows that 20.6% of all N_K forecasts are measured cloudy days which were predicted to be clear. False clear forecasts occurred in 19.7% of *G* forecasts and 12.4% of *E* forecasts. Forecast cloudy, but measured clear conditions were only observed for 5.7% (N_K), 5.5% (*G*), and 6.9% (*E*) of forecasts. These results are indicative that the NWP models are generally biased towards predicting clear conditions and at a larger clear sky index than measured. Overall, the ECMWF model had the smallest likelihood of incorrect forecasts (19.3%) while both the NAM and GFS were incorrect for 25% of forecasts.

Table 3.2: Normalized frequency of clear and cloudy forecasts and observations for each NWP model. The threshold to distinguish between cloudy and clear conditions is a clear sky index of 0.8.

SURFRAD	N_K		*G*		*E*	
	Cloudy	Clear	Cloudy	Clear	Cloudy	Clear
Cloudy	0.187	0.206	0.170	0.197	0.282	0.124
Clear	0.057	0.550	0.055	0.579	0.069	0.525

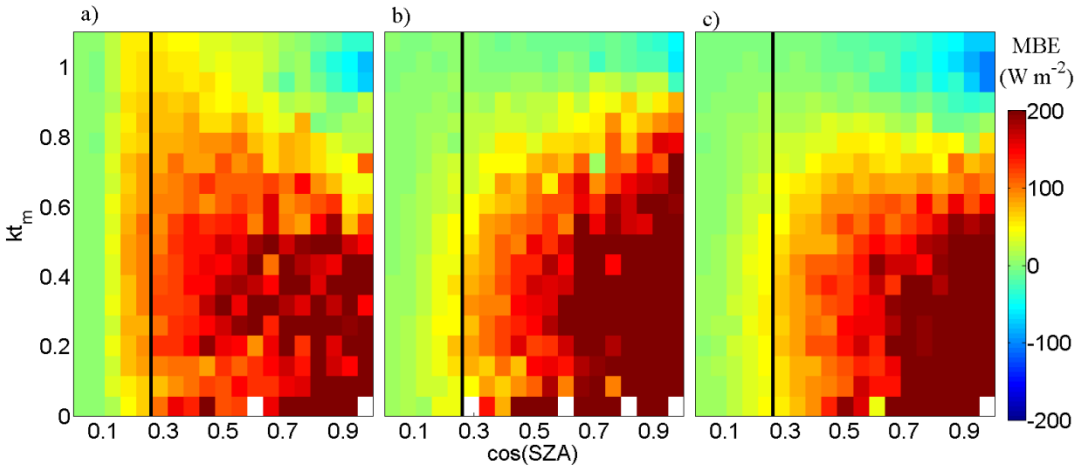


Fig. 3.3: NWP forecast MBE (W m^{-2}) as a function of SZA and measured clear sky index for all SURFRAD stations for a) N_K; b) G; c) E.

3.4 Spatial Evaluation of the NAM for solar irradiance forecasting in California

Spatially, forecast accuracy can vary significantly. This is especially true when cloud or meteorological regimes change drastically over short distances, such as in California. In this section, the NAM will be compared against the extensive California ground measurement network in addition to satellite data (SolarAnywhere, 2013). During summer months, NAM GHI forecasts will be shown to be significantly more biased for coastal regions than inland. Additionally, cumulative distribution functions (cdfs) of bias error show that large GHI over-predictions are much more common near the coast, implying that the effect of summertime coastal clouds is under-predicted. This will motivate a statistical function to describe forecast certainty (Chapter 4).

3.4.1 CIMIS Ground Measurement Network

The California Irrigation Management Information System (CIMIS), managed by the California Department of Water Resources (DWR), is a statewide network of weather stations.

Consisting of 152 operational stations (88 studied here), CIMIS sites (Fig. 3.4) measure air temperature, relative humidity, wind speed, and GHI (CIMIS, 2009a). GHI is measured to within ±5% using Li-Cor LI200S photovoltaic pyranometers (CIMIS, 2009b) and reported as the hourly average of 60 instantaneous measurements.

Built-in quality control flags (CIMIS, 2009c; CIMIS, 2009d) provide information on likely erroneous data. Missing data, data exceeding historical limits, and measurements exceeding clear sky irradiances by more than 5% for extended periods of time are excluded in this study. Furthermore, stations located within 25 km of the Pacific Ocean will be considered coastal stations and those 75 km or from the coast considered inland.

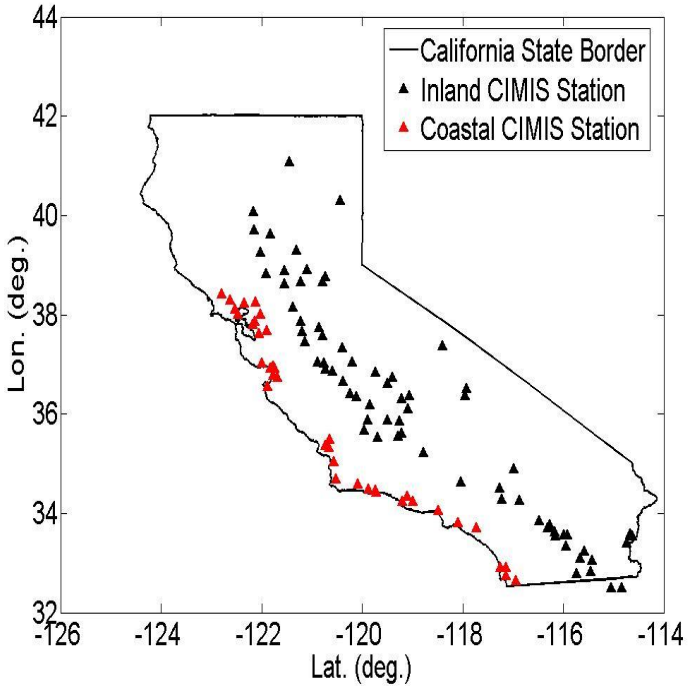


Fig. 3.4: CIMIS weather station locations for California. Black triangles are stations 75 km or more from the coast and red triangles are stations within 25 km of the coast.

3.4.2 SolarAnywhere GHI Dataset

SolarAnywhere (SolarAnywhere, 2013) provides GHI on a 0.01° by 0.01° grid (≈ 0.94 km) for California using the observed cloud fields from Geostationary Operational Environmental Satellite (GOES) imagery. First, a cloud index is calculated from the raw imagery. Instantaneous GHI is calculated by using the cloud index to adjust a clear sky model. Local and seasonal effects of turbidity are considered in addition to topographical effects. Validated by Perez *et al.* (2010) against the Surface Radiation (SURFRAD) network, the SolarAnywhere dataset was found to have root mean square error (RMSE) ranging from 77-112 W m^{-2}. Full details are available in Perez *et al.* (2002).

3.4.3 Spatial Accuracy Evaluation

In summer, cloud conditions can vary significantly for coastal California, especially during morning hours. Marine layer fog and stratocumulus (MLS) conditions, the dominant summer weather phenomena, are frequent but spatially confined to the coast. Rarely penetrating further inland than 25 km, it is expected that these highly localized clouds would have a large impact on NAM GHI accuracy.

Analysis of historical bias error distributions by location can reveal spatial tendencies in N_K accuracy (Fig. 3.5). Regardless of season, N_K is positively biased for both inland and coastal stations. In winter (Fig. 3.5b), coastal and inland CIMIS stations have similar bias error distributions and overall MBE. In summer (Fig. 3.5a), however, GHI over-predictions are much more common, skewing the coastal CDF positive. Large over-predictions (bias error > 200 W m^{-2}) occur for 17.1% of coastal forecasts compared to only 6.1% of inland forecasts. Errors of this magnitude generally occur when clear skies are predicted for measured overcast conditions, implying that summer coastal cloud cover is regularly under-predicted by the NAM. This tendency is characteristic for all coastal N_K forecasts in southern California (Fig. 3.6).

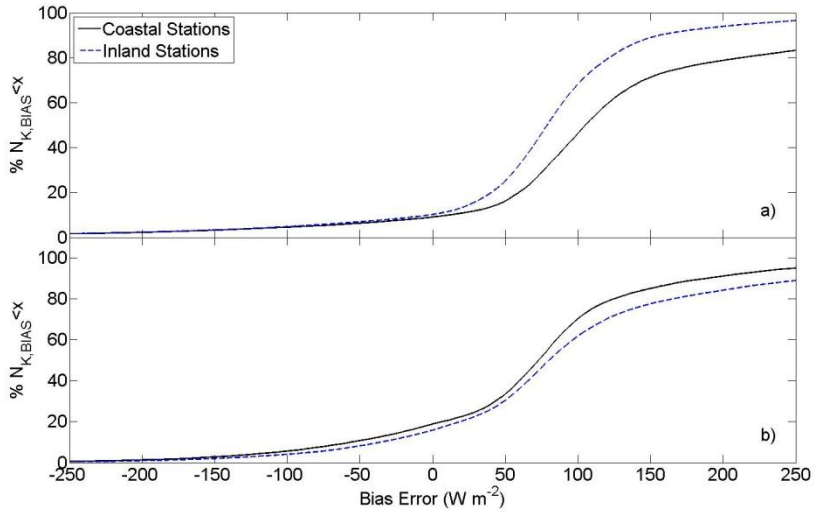


Fig. 3.5: N_K bias error distribution for coastal (black solid line, distance to Pacific Ocean < 25 km) and inland (blue dashed line, distance to Pacific Ocean > 75 km) CIMIS stations for (a) May – July 2010 and (b) November 2010 – January 2011.

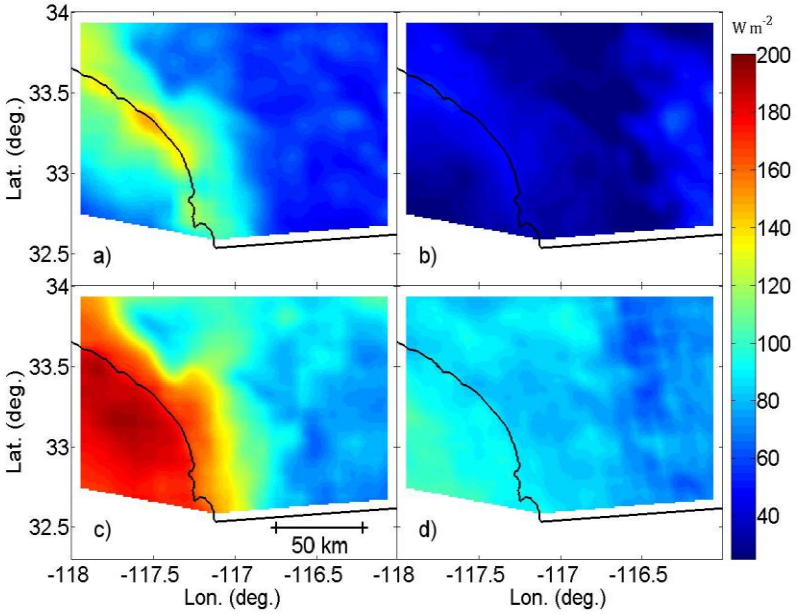


Fig. 3.6: N_K MBE (W m^{-2}, top) and STDERR (W m^{-2}, bottom) compared to SolarAnywhere data for May, June, and July, 2010 (a/c) and November and December 2010 (b/d).

Compared to SolarAnywhere data, N_K MBE approaches 150 W m^{-2} for May, June, and July, 2010 near the coast (Fig. 3.6a). This is consistent with coastal CIMIS stations results (Fig. 3.5a) and reinforces that MLS are under-predicted by the NAM. Further inland, where MLS conditions are unlikely, MBE is less than 30 W m^{-2}. For winter (Fig. 3.6b), when MLS

conditions are rare, N_K MBE is spatially invariant. STDERR (Eq. 3.4), a direct measure of forecast certainty, is location-dependent for summer months (Fig. 3.6c). Near the coast, STDERR exceeds 180 W m^{-2}. As the NAM is unable to accurately predict the spatial extent and duration of MLS conditions, N_K uncertainty is high. For inland regions unaffected by the usually shallow marine layer, the NAM forecast uncertainty is lower.

Thus, for coastal stations, CI_{90} forecast intervals formed by subtracting the 5th and 95th percentiles of the aggregate historical error distribution from N_K are wide (e.g. CIMIS Station 173, Fig. 3.7). Furthermore, as N_K typically over-predicts GHI, the 95th percentile limit is much closer to the N_K forecast (Fig. 3.7a/b, Table 3.1). For inland stations where N_K is more accurate and cloud conditions more predictable, the bias error dispersion is smaller and the forecast interval narrower (Fig. 3.7b). In general, forecast intervals formed using this method encompass nearly the entire range of possible GHI and have limited utility for solar forecasting applications.

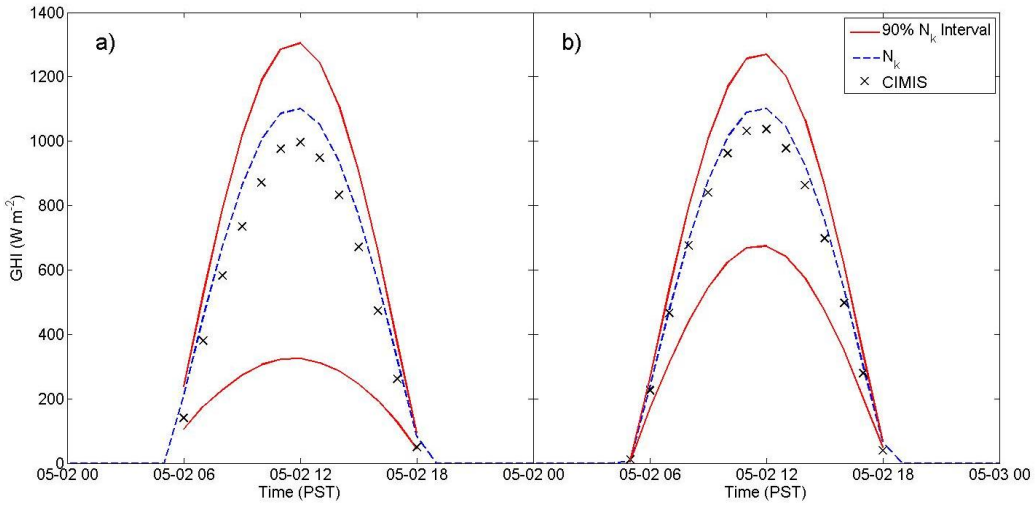


Fig. 3.7: N_K 90% forecast interval for coastal CIMIS Station 173 (a, San Diego, CA) and inland CIMIS Station 128 (b, Salton Sea, CA) based on the historical bias error distribution from summer 2010 (Fig. 3.5a).

3.5 Summary and Conclusions

Overall, the NWP models were shown to be significantly biased towards predicting clear skies. Thus, when plotted against kt_m (Fig. 3.3), negative biases are rare. Overall, N_K, *G*, and *E* predicted more false clear days than false cloudy days. Of the forecasts that erroneously predicted clear or cloudy conditions (Table 3.2), 77.1% of N_K (77.0% for *G* and 64.2% of *E*) were clear forecasts resulting in cloudy days. This was a primary contributor to the large positive MBE observed in forecast clear conditions (Fig. 4.2 in Chapter 4). However, the many accurate clear sky forecasts (59.9% of all N_K, 64.9% of *G*, and 52.5% of *E*) reduced the magnitude of the MBE in clear conditions. Although false cloudy forecast were considerably less frequent (5.0% of all N_K, 4.9% of *G* and 6.9% of *E*), far fewer cloudy days were predicted overall. These few large negative bias events account for part of the 150 W m^{-2} MBE for $kt^* < 0.6$ for N_K and *G* (Fig. 4.2).

Between the original models, ECMWF performed best, closely followed by GFS. Surprisingly, the NAM model performed the worse despite its higher spatial resolution and specialized application to North American Meteorology. Significant problems were found with the clear sky model applied in N_K which over-predicted GHI in clear conditions by up to 40%. A combination of GFS forecasts for clear conditions and ECMWF conditions for cloudy conditions may yield the lowest overall RMSE.

3.6 Acknowledgements

Sections 1-3 have been previously published in Mathiesen and Kleissl, 2011. Section 4 was based off of Mathiesen *et al.*, 2013a.

Chapter 4 Statistical Correction Techniques for NWP

Due to complex cloud microphysics and limitations in spatial resolution and physics parameterizations, clouds and their radiative properties are difficult to predict in numerical models. Consequently, NWP are expected to show inherent regional or global biases limiting forecast accuracy. Chapter 3 described these errors in detail. In general, the operational NWP over-predict irradiance. This error is dependent on location. In California, solar irradiance forecasts near the coast, where cloud conditions are highly dynamic, are most inaccurate. Though significant, error patterns are generally consistent.

As such, statistical correction techniques can be applied to operational forecasts that improve forecast accuracy. Consistent error patterns allow for MOS to be used to produce a bias reduction function for future forecasts (Heinemann et al., 2006). Bofinger and Heilscher (2006) used MOS locally with ECMWF GHI forecasts to create daily solar electricity predictions accurate to 24.5% RMSE. Lorenz et al. (2009) related forecasted solar zenith angle (*SZA*) and clear sky index (kt^*, Eq. 1.1) to ECMWF MBE for Germany, revealing a consistent over prediction (up to 100 W m^{-2}) for moderately cloudy conditions. Using a MOS correction function eliminated bias and reduced RMSE by 5% for 24 h forecasts.

Furthermore, statistical techniques can be used to characterize forecast uncertainty. Generally, this involves calculating forecast certainty from historical distributions of forecast accuracy. Bremnes (2004) expanded on this idea by assuming that forecast (confidence) interval width is a function of other predicted variables. Using local quantile regression, Bremnes (2004) produced month-dependent 90% forecast intervals for wind power output using NWP-predicted 10-m wind speed and direction. For GHI, Lorenz *et al.* (2009) used standard error to estimate prediction interval width. After using model output statistics (MOS) to correct GHI mean bias error (MBE), Lorenz *et al.* (2009) forecast standard error as a function of clear sky index (kt^*)

and solar zenith angle (*SZA*) based on historical measurements. Assuming a normal distribution of standard error, Lorenz *et al.* (2009) was able to produce out-of-sample prediction intervals containing 95% of GHI observations.

This chapter discusses MOS corrections to the NAM, GFS, and ECMWF forecasts that were evaluated in Chapter 3. Using clear sky index and solar zenith angle as input parameters, the MOS correction mitigates bias errors of the NWP forecasts and significantly reduces RMSE. Additionally, forecast uncertainty intervals are created by relating synoptic scale geostrophic wind conditions to historical NWP GHI accuracy. Specifically, the 700 mbar (approximately 3000 m above sea level) East-West geostrophic wind speed, as an indicator of inversion height, is related to the historical GHI bias error. Overall, these statistical corrections provide an effective method to improve the accuracy of the operational NWP.

4.1 Model Output Statistics (MOS) Bias Correction

4.1.1 MOS Methodology

Following Lorenz et al. (2009) a stepwise multivariate fourth-order regression (Rogers, 2007) is applied to derive the MOS correction function (Eq. 4.1).

$$GHI_c\left(SZA, kt^*\right) = \alpha \cos^4\left(SZA\right) + \beta\left(kt^*\right)^4 + \ldots \qquad \text{Eq. 4.1}$$

GHI_c is the modeled MBE for a given *SZA* and clear sky index. Weighted regression coefficient calculation ensures accurate representation of unevenly distributed data (see Fig. 4.1). For all combinations of *SZA* and *kt**, GHI_C provides the best irradiance correction for any future forecast. As an example, the MOS-corrected NAM forecast, $N_{K,c}$, is computed using Eq. 4.2.

$$N_{K,c} = N_K - GHI_c \quad \text{Eq. 4.2}$$

To simulate operational forecasting, local MOS correction functions are calculated dynamically using only the most recent 56 days of MBE analysis (rather than the entire dataset) separately for each SURFRAD station. This provides a training dataset, independent of the evaluation dataset, and a unique MOS correction for each $N_{K,c}$. This method is similarly applied for *G* and *E* and designed to eliminate systematic bias error. Since MOS corrections are not applicable for SZAs larger than 75°, evening and early morning corrected forecasts are not calculated.

4.1.2 NAM MBE Correction

Fig. 4.1a is the histogram for the NAM forecast between March 21st, 2010 and February 8th, 2011, as a function of *SZA* and *kt**. Consistent with Table 3.2, more data exist for predicted clear skies than for cloudy conditions. Fig. 4.1a indicates that the NAM model often forecasts GHI 20% to 40% in excess of clear sky irradiance, especially for large SZAs. While low atmospheric turbidity during clear sky conditions can result in GHI measurements slightly larger than *C*, the frequency and magnitude of forecasts with *kt** > 1 indicates a fundamental problem with either the NAM radiative transfer model or the primary inputs to the model from the NAM forecast. *G* forecasts only exhibit *kt** > 1 for *SZA*s greater than 75°, which could be caused by a different choice of clear sky model. *kt** > 1.1 are not observed for *E* forecasts.

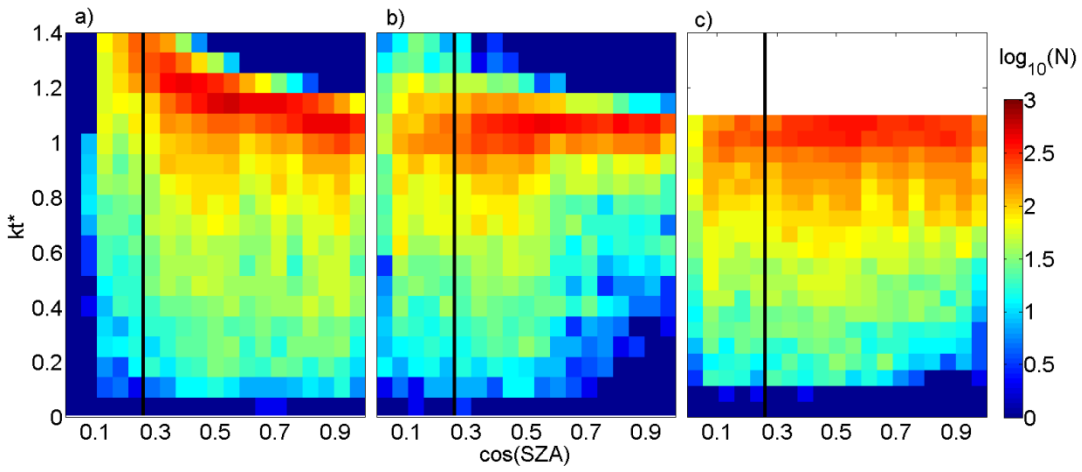


Fig. 4.1: Histogram as a function of solar zenith angle (*SZA*) and clear sky index (*kt**) for a) N_K; b) *G*; c) *E*. Data is presented in $\log_{10}$ format, i.e. a value of 2 indicates 100 observations. All data to the left of the black line (*SZA* > 75°) were not used in the MOS analysis.

The MAE profiles in Fig. 3.2 demonstrate consistent error patterns. However, kt_m is unknown prior to measurement and is unsuitable as an input parameter for MOS correction. Instead MBE profiles as a function of the predicted clear sky index, *kt** must be used. Fig. 4.2a-i shows the MBE of the N_K forecast as a function of cos(*SZA*) and *kt**. For forecast clear sky conditions (*kt** > 0.8), N_K over-predicts measured data by up to 150 W m^{-2} and on average by 73.9 W m^{-2}. In cloudy conditions (*kt** < 0.5), the N_K model under-predicts measured GHI, on average by -32.3 W m^{-2}. Overall, the magnitude of the negative MBE becomes larger for small SZA, while the positive MBE for clear sky conditions becomes slightly smaller for small *SZA*.

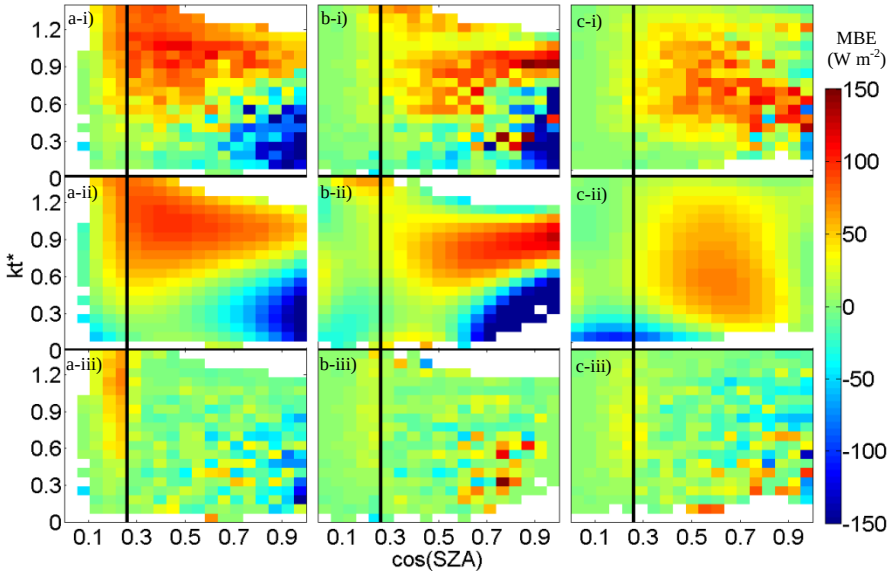


Fig. 4.2: MBE (W m^{-2}) of N_K (a), G (b), and E (c), as a function of solar zenith angle (SZA) and forecasted clear sky index (kt*) compared to SURFRAD measurements: i) raw data, ii) polynomial fit to the data (Eq. 4.1); iii) MBE of the corrected forecasts: $N_{K,c}$, G_c, and E_c

While N_K is an overall inaccurate GHI forecast, Fig. 4.2a shows that NAM bias trends are continuous and therefore, correctable. Using MOS, a correction polynomial was fit to the data (Fig. 4.2a-ii) which well represents the typical MBE characteristics of N_K. Corrections are subsequently applied according to Eq. 4.2, yielding $N_{K,c}$. Note that as temporally dynamic local MOS corrections were applied to simulate operational conditions, Fig. 4.2a-ii was not directly used in forecast correction. The MBE of $N_{K,c}$ (Fig. 4.2a-iii) decreases to less than ±50 W m^{-2} and overall from 57.5 W m^{-2} to 7.0 W m^{-2}. For a perfect MOS correction, a zero MBE would be expected for $N_{K,c}$. Here, the MBE is not zero is due to the polynomial fit MOS correction which cannot fully resolve the variability of Fig. 4.2a-iii.

4.1.3 GFS MBE Correction

Fig. 4.2b-i shows the average MBE profile for the GFS forecast, *G*. The bias error dependence on *kt** is qualitatively similar to the NAM model (Fig. 4.2a-i). For forecasted clear sky conditions (*kt** > 0.8), *G* generally over-predicts GHI, on average by 41.0 W m^{-2}. Similarly, for overcast conditions with moderate to small optical depths (*kt** < 0.5), the GFS forecast is negatively biased by on average -1.8 W m^{-2}. The MBE shows a much stronger dependence on *SZA* compared to the NAM model, increasing during mid-day (MBE_{AVG} = -67.4 W m^{-2} for cos(*SZA*) > 0.7 and *kt** < 0.5) as a result of the larger GHI magnitudes observed then.

Fig. 4.2b-ii shows the MOS correction function fit to Fig. 4.2b-i for the entire data set. From Eq. 4.1, the MOS function applies a negative correction to *G* for predicted clear skies (*kt** > 0.8). Correspondingly, a large positive correction is applied for forecast overcast conditions (*kt** < 0.5). On average, the MBE of the MOS-corrected forecast, G_C (Fig. 4.2b-iii) is reduced from 35.4 W m^{-2} to 5.2 W m^{-2}.

4.1.4 ECMWF MBE Correction

The MBE profile of *E* (Fig. 4.2c-i) is significantly different than N_K or *G*. Predicted clear skies (*kt** > 0.9) and overcast conditions with *kt** < 0.2 are least biased (MBE < 50 W m^{-2}). For predicted moderately cloudy conditions *E* is most significantly biased, by 42.6 W m^{-2} on average. While there are several areas of negative bias, the MBE is in general positive, with some biases exceeding 150 W m^{-2}. Lorenz et al. (2009) found a similar MBE profile for ECMWF data using ground measurements in Germany.

The MOS correction function for *E* (Fig. 4.2c-ii) targets the large positive bias for moderately cloudy conditions. It should be noted that the negative bias correction for very small predicted clear sky indices (*kt** < 0.2) is an artifact of the correction polynomial, which is irrelevant as no such data occurred. This was also observed in the MOS function for *G* (Fig.

4.2b-ii). The MOS correction reduces overall MBE from 31.4 W m^{-2} to 0.5 W m^{-2} (Fig. 4.2c-iii). Using this metric, the MOS correction for *E* is the most effective in reducing systematic errors.

4.1.5 RMSE Comparison

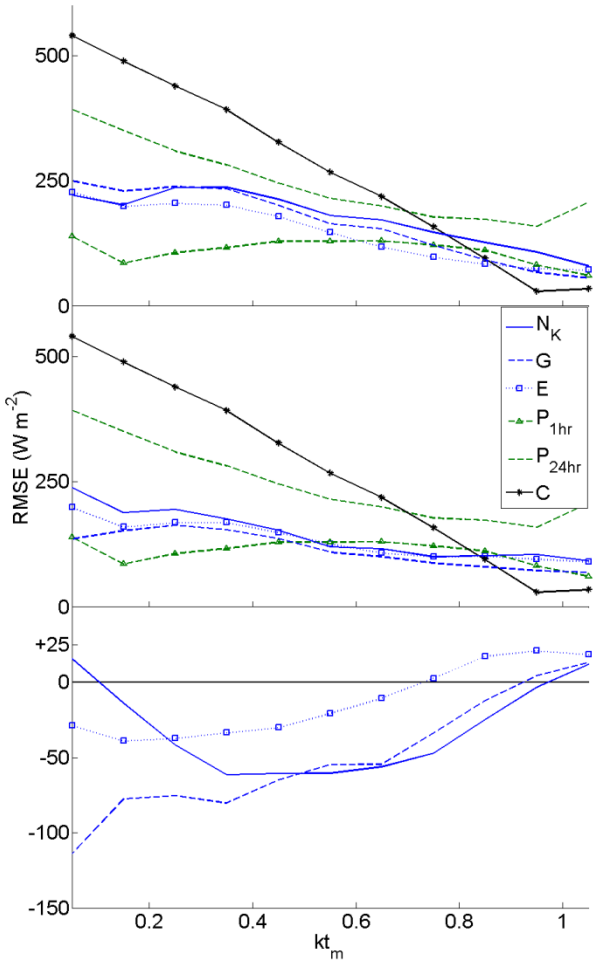


Fig. 4.3: RMSE (W m^{-2}) as a function of measured clear sky index (kt_m): a) (N_K, *G*, *E*, P_1, P_{24}, and *C*); b) ($N_{K,c}$, G_c, E_c, P_1, P_{24}, and *C*); c) Change in RMSE due to MOS correction.

For $kt_m = 1$, *C* is expected to have an RMSE = 0 W m^{-2}. For $kt_m > 0.86$, *C* indeed has the smallest RMSE. However, several instances of $kt_m > 1$ were observed, contributing to the non-zero RMSE for $kt_m = 1$. For overcast conditions, the RMSE of *C* drastically increases.

P_1 is the most accurate forecast for overcast conditions and only slightly less accurate than G and E for clear conditions. Since hourly cloud cover conditions are relatively static the one-hour persistence forecast, P_1, is accurate. For longer persistence forecasting on the order of a day (P_{24}), clear conditions are more static than cloudy. Correspondingly P_{24} RMSE increases with decreasing kt_m, approaching a RMSE greater than 400 W m^{-2} for $kt_m < 0.15$. Transitional periods between synoptic weather patterns and diurnally driven phenomena cause large errors in 24-hour persistence forecasts. For moderate cloudy conditions, the measured clear sky index can vary significantly, making the persistence forecasts inaccurate (e.g. Fig. 3.1 from 1800-2400 UTC). The high spatial variability of irradiance during cloudy conditions is difficult to forecast by NWP. Consequently, NWP RMSE (Fig. 4.3a) increases as kt_m decreases. Under measured clear sky conditions, all NWP forecasts have low RMSE (RMSE < 125 W m^{-2}). In clear conditions ($kt_m = 1$), G is the most accurate. Excluding clear conditions, E has a lower RMSE than other NWP forecasts with typical improvements of 30 W m^{-2} compared to N_K and G.

After MOS correction (Fig. 4.3b) the same general trends for NWP RMSE are present, albeit at a smaller RMSE level. The impact of MOS on RMSE is shown in Fig. 4.3c. Positive changes represent increases in RMSE. The RMSE of the NAM forecast $N_{K,c}$ is reduced by up to 50 W m^{-2} for $0.15 < kt_m < 0.95$. Similarly, G_C is improved over all clear sky indices less than 0.9 by as much as 110 W m^{-2}. The RMSE of E is also significantly lowered for all clear sky indices less than 0.7. For the largest clear sky indices ($kt_m > 0.94$), MOS corrections increased the RMSEs for each NWP forecast. Uncorrected forecasts for measured clear conditions (Fig. 3.3) were relatively unbiased making it difficult to reduce RMSE. For all other clear sky indices, the MOS correction function significantly reduced RMSE.

4.2 Statistical Functions for Uncertainty Forecasts

4.2.1 Relating Synoptic Conditions to Forecast Accuracy

Similarly, statistical methods can be applied to prescribing uncertainty (confidence) intervals to irradiance forecasts. In California, MLS conditions are the largest contributor to irradiance uncertainty for coastal regions and are generally more common for on-shore flow (following the Leipper cycle, Section 2.3). In general, synoptic scale atmospheric flow can be approximated by the geostrophic wind. The theoretical atmospheric flow for which the Coriolis and pressure-gradient forces are in equilibrium, the geostrophic wind can be calculated directly from pressure or geopotential height fields and follows their contours.

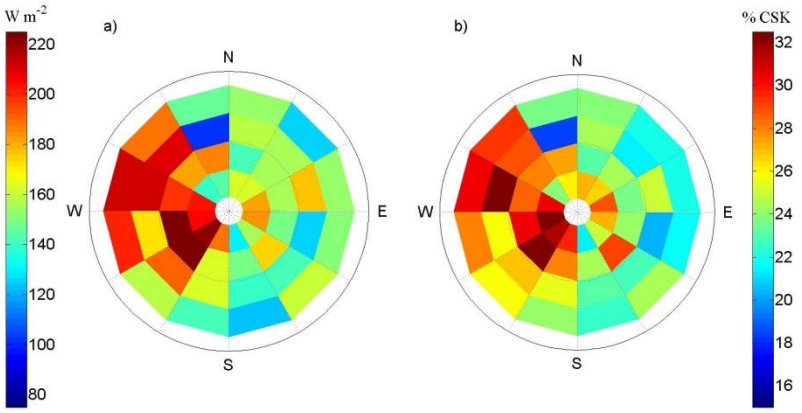


Fig. 4.4: N_K STDERR (a, W m^{-2}) and rSTDERR (b, [% Clear Sky]) as a function of 700 mb geostrophic wind direction and velocity (m s^{-1}) for coastal CIMIS stations between May 1st, 2011 and July 31st, 2011. Velocity ranges from 0 m s^{-1} (center) to 11 m s^{-1} (outside edges).

In summer, N_K is least accurate when the 700 mbar geostrophic wind direction is westerly (Fig. 4.4). This corresponds to on-shore flow generated by a low pressure center over northern California and conditions favorable for cloud formation (Leipper, 1948, Leipper, 1994). Conversely, clear conditions are expected for off-shore flow (easterly). Correspondingly, N_K is most accurate for easterly geostrophic winds with velocities exceeding 4 m s^{-1} (Fig. 4.4b). For winter months (November, December, and January) these trends were not distinct.

4.2.2 Historical rMBE Distribution

The N_K forecast interval limits are defined by the historical distribution of rMBE (Fig. 4.5). Large negative u_g indicate off-shore flow and are associated with clear skies and low N_K uncertainty. As such, both rMBE limits are near 0% regardless of *kt**, resulting in a narrow forecast interval. For weak on-shore geostrophic winds ($0 < u_g < 4$ m s^{-1}), the forecast interval limits vary from -60% to +60% as $\boldsymbol{N_K}$ uncertainty is large. For strong on-shore geostrophic winds ($u_g > 5$ m s^{-1}) the forecast interval narrows, indicating that the NAM predicts cloud cover more accurately for strong atmospheric flow, regardless of direction. $\boldsymbol{N_K}$ interval limits are also dependent on the forecast clear sky index. For forecast clear conditions (*kt** > 0.8), $\boldsymbol{N_K}$ frequently over-predicts such that the interval minimum limit is 50%-75% lower than *kt** but the upper limit is only 0%-5% larger than *kt**.

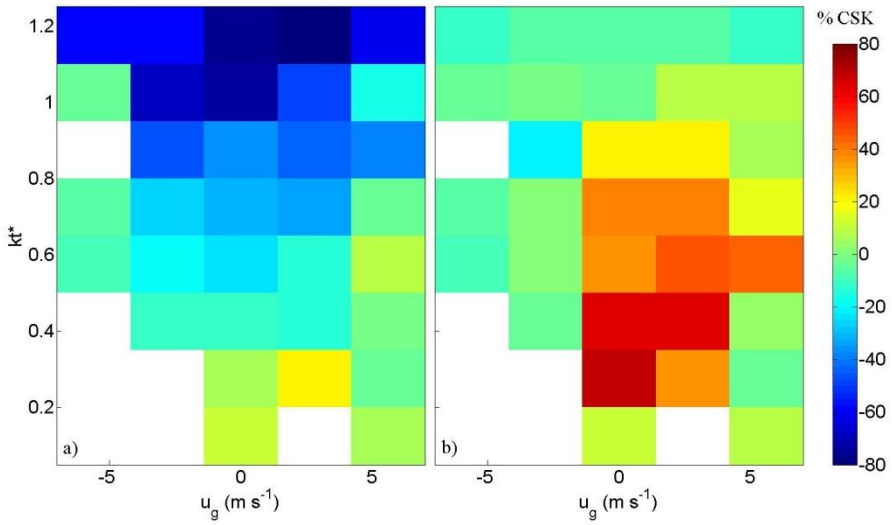


Fig. 4.5: rMBE 5% (a) and 95% (b) interval limits (% of clear sky GHI) averaged over all CIMIS stations for May 1st, 2011 – July 31st, 2011.

4.2.3 Uncertainty Interval Example

On May 8th, 2011, a low-pressure system was centered over northern California (Fig. 4.6a). Westerly atmospheric flow conditions result as geostrophic winds move counter-clockwise

around centers of low pressure. Historically, a wide range of forecast errors were observed at coastal CIMIS stations within the westerly geostrophic wind regime. Generally, this would result in a wide forecast interval (Fig. 4.4). However, since *kt** is low and cloudy conditions are likely, the $\boldsymbol{N_K}$ forecast interval is narrow. Contrastingly, the Lorenz *et al.* (2009) interval is nearly three times as wide.

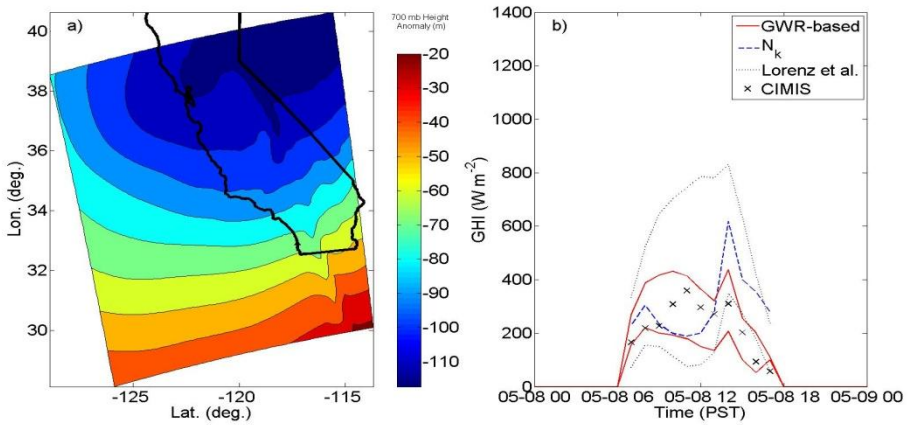


Fig. 4.6: May 3rd, 2011 700 mb geopotential height anomaly (m) and corresponding N_K forecast interval for CIMIS station 173 compared against the intervals obtained by Lorenz *et al.* (2009). Westerly atmospheric flow conditions (a) correspond with likely cloudy conditions.

4.3 Summary and Conclusions

Overall, statistical techniques are an effective method for reducing the error of NWP irradiance forecasts. Table 4.1 summarizes the results of the MOS correction when averaged across all SURFRAD stations. The local MOS functions, used in conjunction with forecast *SZA* and *kt**, reduced RMSE by 20.1 W m^{-2} (N_K), 17 W m^{-2} (E), and 25.6 W m^{-2} (G) and effectively eliminated MBE. RMSE reductions were largest for intermediate *kt** at about 50 W m^{-2}. MBEs were similar across different sites with the smallest errors at Desert Rock, NV (site with the largest kt_m) and the largest errors at Pennsylvania State University, PA (site with the lowest kt_m). MOS-corrected RMSE were smallest at the most clear site, Desert Rock, and largest at Fort Peck,

Montana. For all stations, seasonal changes in bias errors limit MOS-correction accuracy. For several SURFRAD stations, MBE were observed to change significantly from month to month. As the MOS-correction uses 56 days of training data, sudden changes in MBE dependence on SZA and kt^* are not immediately represented increasing the MBE of the MOS-corrected forecasts.

Table 4.1: MBE and RMSE for NWP forecasts before and after MOS correction averaged across all sites.

	N_K	G	E
MBE (W m^{-2})	57.3	35.4	31.4
MBE_C (W m^{-2})	7.0	5.2	0.5
RMSE (W m^{-2})	134.2	110.5	123.2
$RMSE_C$ (W m^{-2})	114.1	84.6	106.2

MOS application to the NWP irradiance output was successful in minimizing bias and reducing RMSE, but did not provide information as to the source of the MBE. Errors originating from the radiative transfer model (RTM), cloud model, and prognostic variable errors can all have contributed to the MBE. Furthermore, MOS corrections in the measured clear sky regime (kt_m > 0.9) did not reduce RMSE (Fig. 4.3c). This is because the MOS could not distinguish between RTM errors (over-prediction of GHI even for clear skies, especially for NAM) and cloud model errors (incorrect parameterization of RTM inputs). Consequently, many initially accurate forecasts were unnecessarily corrected. Rather than correcting all forecasts, differentiating between the sources of the error is the first step into understanding which forecasts need to be corrected.

4.4 Acknowledgements

Previously, section 1 was published in Mathiesen and Kleissl, 2011. Material from section 2 was based off of Mathiesen *et al.*, 2013a.

Chapter 5 A High-Resolution Cloud-Assimilating NWP

Though the operational NWP are more accurate than persistence or imagery based techniques, Chapter 3 and Chapter 4 have conclusively demonstrated that they consistently over-predict irradiance and are generally inaccurate, even when bias corrected using model-output-statistics. This error can be attributed to several sources as discussed in Section 1.4. In this chapter, a new, high-resolution, cloud-assimilating NWP model is developed and tested at the University of California, San Diego (UCSD) for solar irradiance forecasting (WRF-CLDDA). Using fine spatial resolution, physics parameterizations that promote cloud-cover formation, and a cloud-assimilation system, this model is specifically designed to minimize the errors typically associated with NWP irradiance forecasts (Section 1.4). Using WRF-CLDDA, irradiance forecasts are produced for the summer period (5/1/11 – 6/30/11) and validated against a dense UCSD pyranometer network. During this time, marine layer stratocumulus clouds (Chapter 2) are common. Since marine layer clouds are co-located with regions that have high-potential for distributed generation solar photovoltaic generation (the southern California coast), their accurate prediction is critical. WRF-CLDDA hourly-average irradiance forecasts are calculated and compared to NAM forecasts and ground observations. Finally, the ability of WRF-CLDDA to resolve detailed, high-resolution cloud fields is tested by comparing forecast irradiance variability, expressed as a ramp-rate distribution, to observed variability. Overall, it is shown that clouds are successfully populated into the initial conditions and that WRF-CLDDA irradiance forecasts are significantly more accurate than the NAM, especially during marine layer cloud conditions.

5.1 The Weather Research and Forecasting Model (WRF)

The Weather and Research Forecasting (WRF, Skamarock *et al.*, 2008) model is a highly customizable numerical weather prediction model that is maintained by the National Center for Atmospheric Research (NCAR). In this study, WRF V3.4 is configured with three-nests of horizontal resolutions of 12 km, 4 km, and 1.3 km (Fig. 5.1, centered at the University of California, San Diego). Boundary conditions for the outer domain are derived from the NAM. To facilitate low-altitude marine layer stratocumulus formation, the domain is vertically divided into 75 terrain-following levels, 50 of which are below 3000 m. The model time-step size is defined dynamically according to a Courant-Freidrichs-Lewy (CFL, Eq. 1.2) criterion of 0.3. This ensures that the distance of horizontal advection occurring in a single time step does not exceed the discretization size. Downward short-wave irradiance fields are output every 5 min to a maximum forecast horizon of 36 hours.

Cloud microphysics is parameterized using the Thompson microphysics package (Thompson *et al.*, 2004). Previously, Otkin and Greenwald (2008) demonstrated that the Thompson scheme produced accurate WRF-simulated cloud fields while maintaining efficient computation time. The Thompson model is a hybrid single/double moment parameterization that explicitly predicts the interaction between six classes of water (water vapor, cloud water, rain, cloud ice, snow, and graupel) in addition to the cloud ice number concentration. To support marine layer stratocumulus formation, the cloud condensation nuclei (CCN) concentration for water clouds is fixed at 300 cm^{-3} (Hudson and Frisbie, 1991). Furthermore, planetary boundary layer (PBL) mixing is parameterized using the Mellor-Yamada-Nakanishi-Niino scheme (MYNN, Nakanishi and Niino, 2006). Like in the NAM, sub-grid scale vertical mixing is unresolved in the coarse ($\Delta x = 12$ km) domain and the Kain-Fritsch (Kain, 2004) cumulus parameterization is applied. For the inner nests ($\Delta x \leq 4$ km) it is assumed that all vertical motion is explicitly resolved and no cumulus parameterization is used. Finally, irradiance is calculated

using the MM5 short-wave scheme (Dudhia, 1989) which takes into account cloud reflection, cloud absorption, water vapor absorption, and clear-sky scattering.

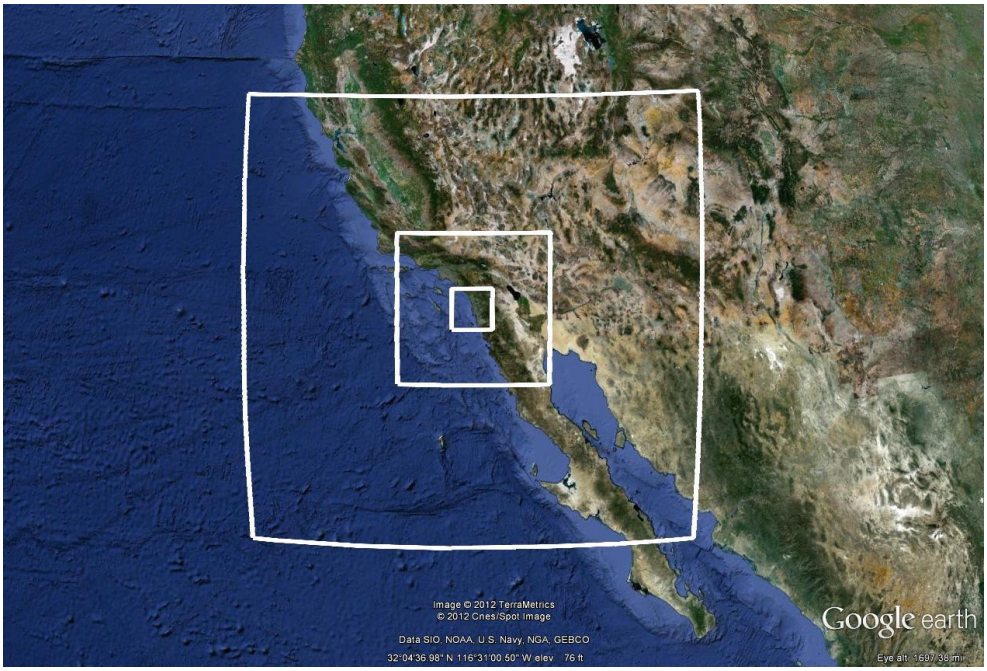


Fig. 5.1: WRF-CLDDA nest configuration (Δx = 12 km, 4 km, 1.3 km) centered at the University of California, San Diego using Google Earth.

5.2 WRF Cloud Assimilation System (WRF-CLDDA)

5.2.1 GOES Cloud Data

Cloud field information is determined using Geostationary Operational Environmental Satellite (GOES) imagery. GOES Solar Insolation Project (GSIP) level-2 data provides cloud-top-temperature (CTT) with 4 km x 4 km spatial resolution (Sengupta *et al.*, 2010). To remove noise, CTT data is spatially convolved to 12 km horizontal resolution. Furthermore, clouds spanning less than 3 adjacent pixels (< 12 km) are filtered from the data and data that is missing or outside of historical limits is ignored.

5.2.2 WRF-CLDDA Methodology

In standard data assimilation, observations are used to produce an optimal estimate for the initial conditions of the state variables (e.g. pressure, temperature, relative humidity, etc.). The cloud microphysics model in conjunction with the modified state variables is subsequently relied upon to accurately populate the initial conditions with clouds. As cloud hydrometeors are not directly initialized into the model, several hours of simulation time (known as 'spin-up') are required to develop the initial cloud field. Since the benefit of data assimilation often disappears over the first few hours (Novakovskaia *et al.*, 2011), this 'indirect' approach becomes impractical as clouds formed from assimilated data are nearly always outdated. Alternatively, direct cloud assimilation initializes clouds nearly instantaneously by raising water vapor mixing ratios to supersaturation, forcing the microphysics scheme to convert excess water vapor to clouds.

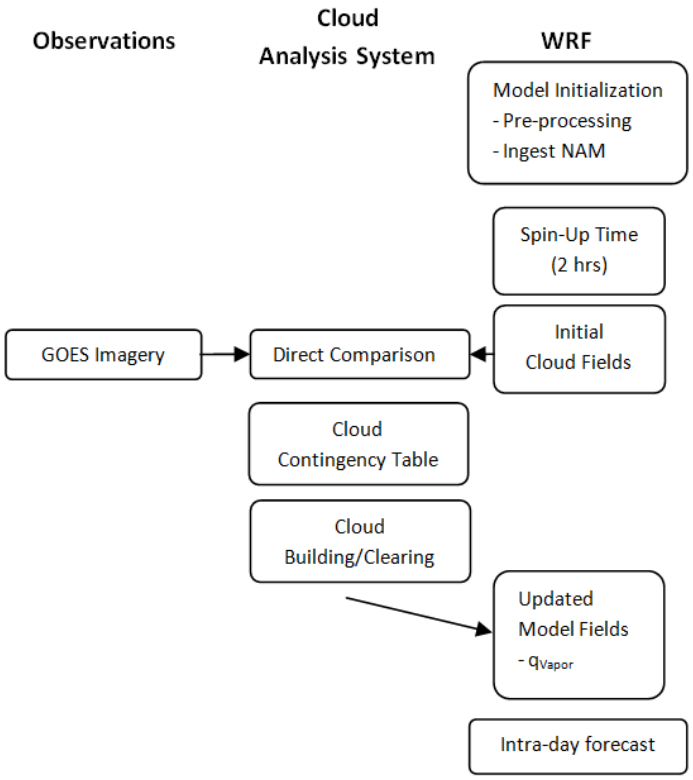


Fig. 5.2: WRF-CLDDA direct cloud assimilation system overview.

Fig. 5.2 depicts a general outline of the WRF-CLDDA forecast system. The direct-cloud assimilation is based on Benjamin *et al.* (2002, 2004b), Albers *et al.* (1996) and Hu *et al.* (2007). First, the WRF model is initialized with 12 UTC NAM data. For two simulation hours, WRF is spun-up with redundant 12 UTC NAM boundary conditions. In this way, NAM provided initial conditions such as wind velocity and pressure are downscaled to match the high-resolution WRF-domain topography. To initialize cloud cover, GOES satellite imagery is first co-located onto the WRF grid. Horizontally, the convolved CTT field is matched to WRF coordinates via nearest neighbor interpolation. In coastal California, the dominant overnight cloud structure consists of stable marine stratocumulus clouds. Assuming this cloud structure, model cloud-top location is fixed to the base of the columnar temperature inversion. In general, cloud thickness increases with inversion height. As such, model cloud base is calculated according to Eq. 5.1 and Eq. 5.2.

$$z_{c,base} = 0.45 \cdot z_i ; z_i < 750\, m \qquad \text{Eq. 5.1}$$

$$z_{c,base} = 0.28 \cdot z_i + 127.5; z_i \geq 750\, m \qquad \text{Eq. 5.2}$$

Here, $z_{c,base}$ is the base of the cloud and $z_.$ is the altitude of the temperature inversion. If no temperature inversion is predicted within the column, cloud-top pressure is instead calculated via the intersection of the WRF-simulated vertical temperature profile and observed CTT. Finally, the 2-D cloud-top and cloud-base location maps are combined to produce a 3-D binary matrix of cloud location co-located with the WRF domain. This cloud contingency table determines the action for cloud-building and -clearing in the domain initial conditions

Assimilated cloud water content is determined via WRF-simulated temperature and pressure profiles. The saturation water vapor mixing ratio (q_s) is defined by Eq. 2.1 where P is pressure, e_s is the saturation water vapor pressure, and ε is the ratio of the gas constants of moist

and dry air. e_s, however, depends on temperature and is defined by the Clausius-Clapeyron Equation (Eq. 2.2 in hPa). For observed cloudy cells, q_s is calculated using the WRF-simulated temperature and q_v (the water vapor mixing ratio) is raised to 110% of saturation using Eq. 5.3.

$$q_v = 1.1 \cdot q_s \qquad \text{Eq. 5.3}$$

Raising q_v to 110% of saturation generally produces clouds that are optically similar to the marine stratocumulus clouds observed in coastal California. Excess water in supersaturated grid cells is immediately converted from q_v to cloud water (q_L) or cloud ice (q_i) via the microphysics simulation of cloud condensation. During this process, latent heat is released causing an unintended increase in model air temperature. To avoid this side-effect, microphysics heating in WRF is disabled for the hour following cloud assimilation. For grid cells without GOES cloud cover, q_v is reduced to a maximum of 75% of saturation. Fig. 5.3 shows an example of the cloud assimilation result for June13, 2011. For areas observed as cloudy (green in Fig. 5.3a), columnar q_v (Fig. 5.3b) is large. Over the eastern Gulf of California, higher temperatures result in larger saturation water vapor mixing ratios (q_s) and subsequently higher concentrations of q_v (Eq. 5.3).

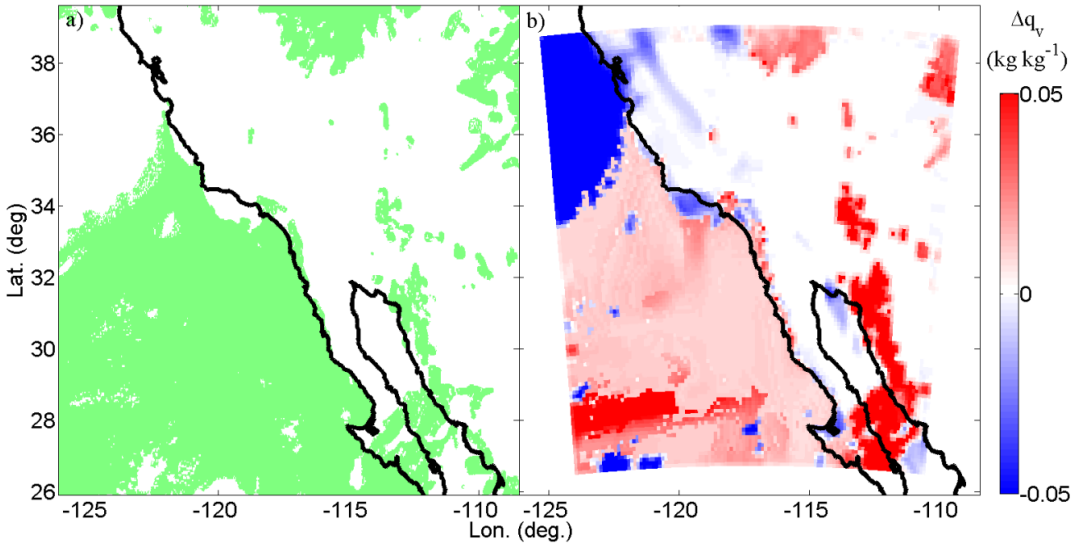


Fig. 5.3: a) GOES cloud mask, where green is cloudy and white is clear and b) Δq_v (kg kg^{-1}) for assimilated initial conditions on 6/13/2011.

Several further steps are performed to ensure numerical stability. To avoid disagreement with the specified boundary conditions, data assimilation is not performed for the outer 5 points on each side of the domain. Furthermore, numerical instability manifested as unphysical, rapid waves can be triggered by large gradients. To avoid creating artificial water vapor gradients through data assimilation, the q_v field is smoothed horizontally via convolution for all cells within 30 km of cloud-building cells. Vertically, spline interpolation is used to smooth q_v within 7 levels.

5.3 WRF-CLDDA Validation

5.3.1 Qualitative Validation of a Single Day

For 6/13/2011, WRF-CLDDA predicted the MLS general pattern (Chapter 2) well resulting in an accurate irradiance forecast (Fig. 5.5). Fig. 5.4 depicts vertical cross sections through UCSD (black line) for the NAM and WRF-CLDDA forecasts. On this day, marine layer

clouds capped by the temperature inversion (dashed red line) were predicted by both models. In the NAM, however, the cloud cover retreated to the ocean (≈-117.3°) by 0800 PST. WRF-CLDDA predicted thicker clouds that extended inland and persisted until 1000 PST and WRF-CLDDA GHI increased significantly. On this day, the dissipation of the marine layer at UCSD was accurately predicted to within 10 min. at UCSD (Fig. 5.5).

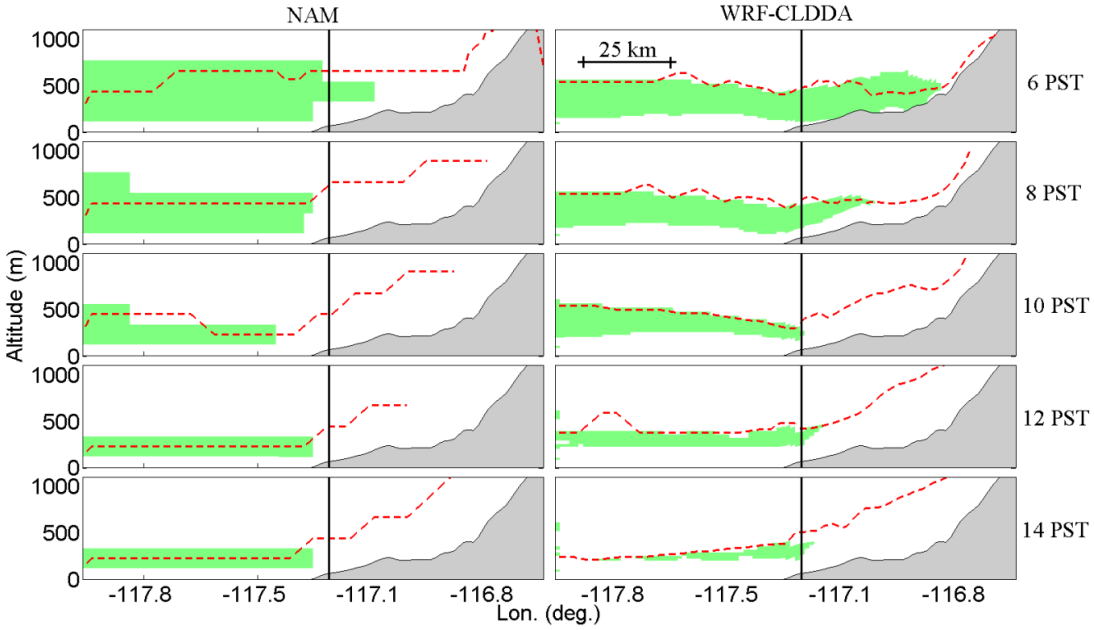


Fig. 5.4: NAM (left) and WRF-CLDDA (right) cross-sections for 6/13/2011 depicting cloud extent (green) and temperature inversion height (dashed red line). The black vertical line marks the location of UCSD. For all forecasts, marine layer cloud cover extent is greatest in the early morning (0600 PST). As temperature near the surface increases, the temperature inversion rises and marine layer clouds over land dissipate until 1200 PST.

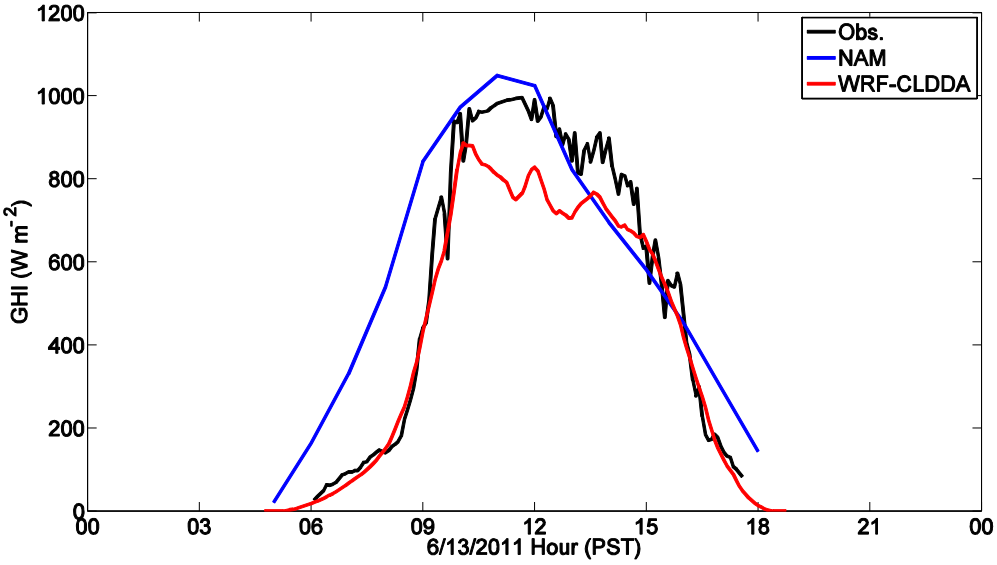


Fig. 5.5: Time-series of 5-min. observed (black), hourly NAM-predicted (blue), and 5-min. WRF-CLDDA-predicted (red line) GHI for 6/13/2011.

5.3.2 Irradiance Error Metrics

Decision Making using Real-time Observations for Environmental Sustainability (DEMROES) is a high-density network of weather stations located at the University of California, San Diego. In addition to meteorological data such as wind speed/direction, temperature, and precipitation, global horizontal solar irradiance at the surface (GHI) is measured at 1 Hz to within ±5% (Campbell Scientific, 1996) using Licor LI-200SZ photodiode pyranometers. To match WRF-CLDDA/NAM GHI output, 1 s irradiance data is temporally averaged to 5 min or 1 hr. Furthermore, to ensure that similar spatial scales are being compared between NWP and observed data, DEMROES GHI measurements are averaged across WRF-simulated grid cells prior to comparison. In this study, only the cell containing six DEMROES stations was analyzed (Fig. 5.6, red dots).

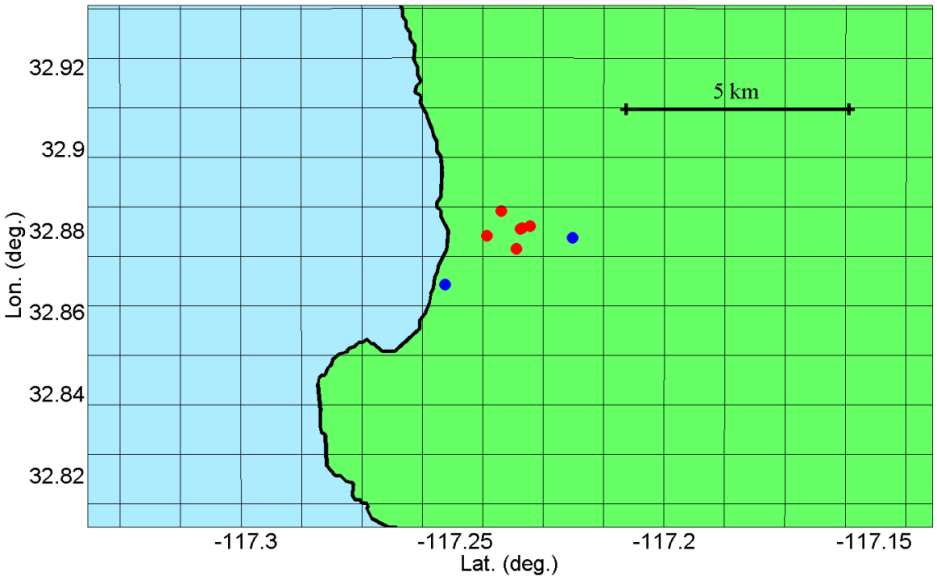


Fig. 5.6: Map of WRF-CLDDA grid cells (Δx = 1.3 km) and DEMROES pyranometer locations (red circles). Blue circles show DEMROES sites that were not analyzed and the black line demarks the Pacific coast.

For the May through June 2011 forecast period, consistent with marine layer cloud cover, observed clear sky indices (Eq. 1.1) fit an approximate bi-modal pattern (Fig. 5.7a) corresponding to clear ($kt_m = 1.0$) and overcast ($kt_m < 0.3$) conditions. Specifically, overcast conditions were common for morning hours (< 0900 PST); for over 30% of days marine layer cloud cover resulting in $kt_m < 0.3$ was observed. By 1000 PST, clear conditions ($kt_m > 1.0$) were observed most frequently (> 60% of days) and generally persisted until late afternoon (1600 PST). In evening (1800 PST) overcast conditions were found to return for 25% of days. In principle, kt_m should never exceed 1. Thus, the large frequency of observations with $kt_m > 1$ indicates a shortcoming in GHI_{CSK}. However, since the clear sky model was similarly applied to observation, NAM, and WRF-CLDDA data, the comparison is valid.

Contrastingly, the NAM (Fig. 5.7b) intra-day kt^* distribution was dominated by clear conditions ($kt^* > 1.0$) throughout the day. Even for early morning hours, NAM intra-day forecasts rarely predicted overcast conditions, indicating that marine layer cloud cover is

routinely under-predicted. For day-ahead forecasts, however, cloudy conditions were more common. For morning hours, the NAM predicted cloudy conditions less frequently (15%) and at a larger kt^* ($kt^* = 0.50$) than observation ($kt_m = 0.25$). Thus, morning cloud cover predicted by the NAM was optically too thin. For mid-day day-ahead forecasts (1200-1800 PST), the NAM kt^* distribution was inaccurate. Clear conditions were over 20% less common than observed and partially cloudy conditions ($0.50 < kt^* < 0.75$) were 10%-20% more common than observed. As such, the kt^* distribution appears more random than observed.

The WRF-CLDDA intra-day and day-ahead kt^* distributions (Fig. 5.7), however, matched the bi-modal observation pattern well. The frequency of morning marine layer cloud cover was captured accurately for both intra-day and day-ahead forecasts indicating that WRF-CLDDA correctly predicts the extent and thickness of overnight marine layer reformation.

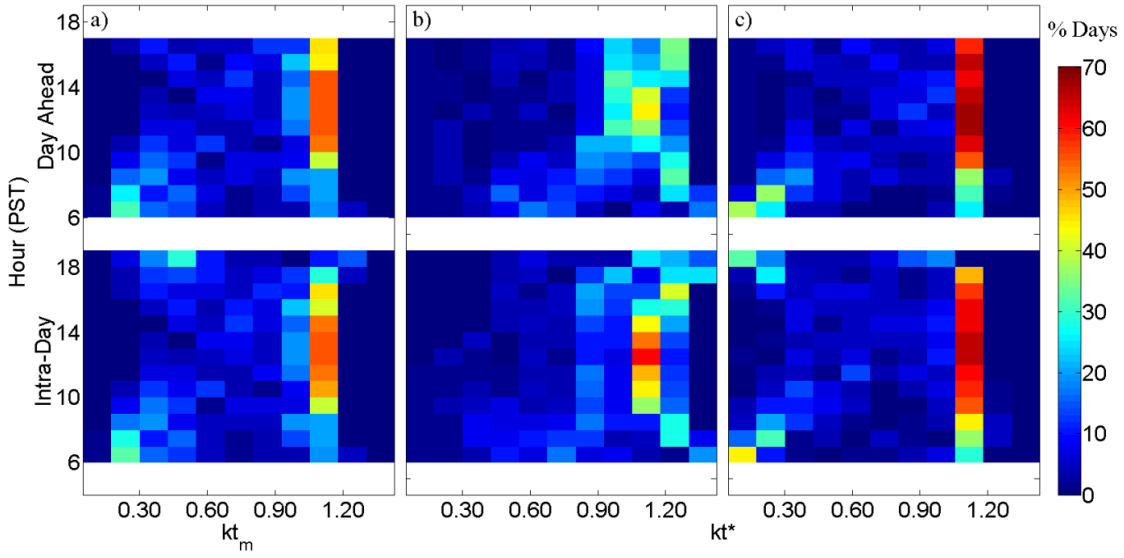


Fig. 5.7: Joint clear sky index (kt_m/kt^*) and time of day (hr PST) histogram for observations (a), NAM (b) and WRF-CLDDA (c) intra-day and day-ahead forecasts for UCSD in May and June 2011.

Table 5.1: Summary of hourly-average error metrics for persistence, NAM, and WRF-CLDDA irradiance forecasts at UC San Diego.

	Error	Intra-Day			Day Ahead		
	(% GHI_{CSK})	P_{24}	NAM	WRF-CLDDA	P_{24}	NAM	WRF-CLDDA
Overall	rMBE	3.3	17.8	0.4	2.7	14.3	1.6
	rMAE	22.4	25.4	21.3	28.3	23.8	18.2
	rRMSE	30.4	33.8	31.1	36.7	32.8	27.5
	rSTDERR	30.2	28.7	31.1	36.6	29.5	27.5

Table 5.2: Error summary (% GHI_{CSK}) as divided by month.

	Error	Intra-Day			Day Ahead		
	(% GHI_{CSK})	Pers.	NAM	WRF-CLDDA	Pers.	NAM	WRF-CLDDA
May	rMBE	2.0	14.7	-2.8	2.1	13.4	2.2
	rMAE	22.0	22.3	20.4	30.6	24.3	17.5
	rRMSE	31.0	30.0	29.9	39.3	34.6	27.0
	rSTDERR	30.9	26.1	29.8	39.2	31.7	26.9
June	rMBE	4.8	21.1	3.8	3.2	15.0	1.0
	rMAE	22.8	28.7	22.2	27.0	24.0	19.4
	rRMSE	29.7	37.4	32.2	34.8	31.6	28.7
	rSTDERR	29.3	30.8	31.9	34.7	27.8	28.7

Quantitatively, irradiance error is summarized in Table 5.1. Here, intra-day (day-ahead) persistence forecasts are calculated by multiplying the hourly-average kt_m from 24 (48) hours prior with clear sky irradiance. As expected, WRF-CLDDA is more accurate than the persistence models; day-ahead rMAE is 11.1% smaller. However, WRF-CLDDA only improves over the 24 hr persistence model by 1.1%. Since the presence of marine layer stratocumulus is dependent on slowly changing, large scale meteorological conditions (e.g. the general circulation pattern and marine temperature inversion characteristics), coastal cloud cover patterns are often similar on consecutive days. Under these conditions, the 24 hr persistence model generally captures the irradiance signal well.

Consistent with previous studies (Mathiesen and Kleissl, 2011), NAM intra-day forecasts are positively biased (rMBE = 17.8%) indicating an under-prediction of coastal cloud cover. Comparatively, WRF-CLDDA irradiance forecasts are only slightly positively biased (rMBE = 0.4%), representing a large improvement in accuracy. Furthermore, improvements are observed in both intra-day rMAE (4.1%) and rRMSE (2.7%). In terms of rSTDERR, however, WRF-CLDDA is 2.3% less accurate. Since relative standard error is the bias-corrected rRMSE it represents the random component of forecast error and can be interpreted as the 'spread' of the forecast error distribution. Thus, though WRF-CLDDA is much less biased, intra-day forecast errors are similarly as random as the NAM.

In general, NWP rMAE and rRMSE increase by 1%-3% between intra-day and day-ahead forecasts (Perez *et al.*, 2011). Here, however, NAM rRMSE decreases by 1% and rMBE decreases by 3.5%. Despite the slight improvement in rRMSE, NAM rSTDERR increases by 0.8% since less of the forecast error can be attributed to systematic bias. This confirms that the day-ahead NAM kt^* is more random (Fig. 5.7b).

Additionally, WRF-CLDDA day-ahead forecasts are slightly more accurate than intra-day. WRF-CLDDA day-ahead rSTDERR is 27.5% (an improvement of 2% over the NAM). As discussed previously, the day-ahead kt^* distribution indicates that WRF-CLDDA accurately predicts the overnight reformation of marine layer cloud cover. Furthermore, clouds assimilated within the large outer WRF-CLDDA domain likely increase day-ahead accuracy. Since the outer domain of WRF-CLDDA is very large (1500 km x 1500 km), clouds (especially frontal systems) can be assimilated and advected for 24 hours or more before impacting the region of interest and improving the day-ahead irradiance forecast.

Previously, Lara-Fanego *et al.* (2011) found WRF rMBE of 62% - 75% (Table 5.3) for observed overcast conditions ($kt_m < 0.4$). Overall, it was concluded that WRF predicted clear skies too frequently and that WRF accuracy decreases as observed cloud fraction increases. Here,

considering only observed overcast conditions WRF-CLDDA intra-day rMBE was 16.3% (Table 5.3). While still over-predicting irradiance, this demonstrates that the combination of model configuration and data assimilation increases the likelihood that cloudy conditions will be forecast correctly. Furthermore, WRF-CLDDA improved most over the NAM for overcast (ΔrRMSE = 10.7%) and cloudy ($0.4 < kt_m < 0.65$, ΔrRMSE = 10.5%) conditions indicating that WRF-CLDDA performs best when clouds are present. Clear conditions ($kt_m > 0.65$), however, were negatively impacted; NAM rRMSE was 5.3% lower than WRF-CLDDA. When compared to the reference persistence forecast, WRF-CLDDA has rRMSE 22.8% lower for overcast conditions and 37.8% lower for cloudy conditions (Table 5.4). Only in clear conditions (ΔrRMSE = -22.5% when referencing the persistence) did WRF-CLDDA have less accurate forecasts. Furthermore, Lara-Fanego found rMBE between 2% and 4%, while WRF-CLDDA rMBE was -4.8%. Thus, for some clear observations, clouds incorrectly were assimilated or failed to evaporate in WRF-CLDDA.

Table 5.3: rMBE and rRMSE error summary (% GHI_{CSK}) as divided by clear sky index. Lara-Fanego *et al.*, 2011 values are reported as the range of annual error between observation sites.

kt_m range	rMBE (%)			rRMSE (%)		
	Lara-Fanego *et al.*, 2011	NAM	WRF-CLDDA	Lara-Fanego *et al.*, 2011	NAM	WRF-CLDDA
$kt_m < 0.4$	[62, 75]	43.1	16.3	[116, 149]	52.0	41.3
$0.4 < kt_m < 0.65$	[13, 20]	34.8	0.9	[35, 45]	47.2	36.7
$kt_m > 0.65$	[2, 4]	6.1	-4.8	[9, 14]	20.0	25.3

Table 5.4: rMBE and rRMSE error summary as a percentage of persistence error as divided by clear sky index.

kt_m range	rMBE (% Pers. rMBE)			rRMSE (% Pers. rRMSE)		
	NAM	WRF-CLDDA	Δ|rMBE|	NAM	WRF-CLDDA	ΔrRMSE
$kt_m < 0.4$	106	40.1	65.9	112	89.2	22.8
$0.4 < kt_m < 0.65$	190	4.9	185.1	167	130	37
$kt_m > 0.65$	-51.3	40.3	11	85.5	108	-22.5

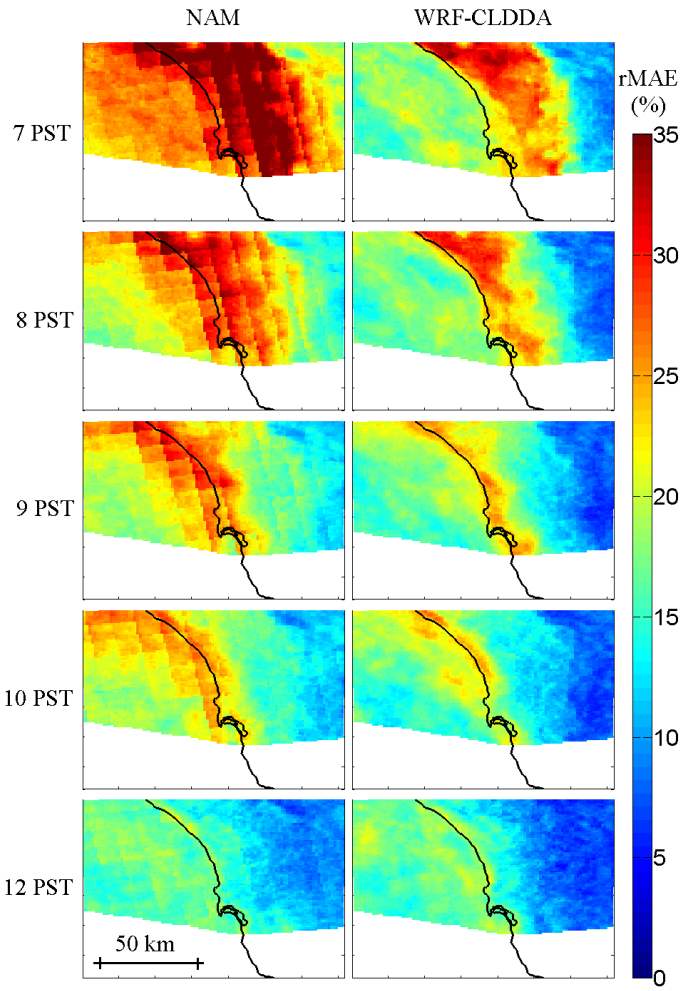


Fig. 5.8: rMAE (% GHI_{CSK}) of NAM (left) and WRF-CLDDA (right) forecasts compared to SolarAnywhere data at several times of day. In early morning hours, NAM forecasts are much less accurate, especially over oceanic and coastal regions, indicating a deficiency in predicting marine layer cloud cover.

Fig. 5.8 shows the spatial rMAE of NAM (left) and WRF-CLDDA (right) irradiance forecasts as a function of time of day. At 0700 PST, NAM forecast rMAE is approximately 27% over the ocean. For land areas within 30 km of the coast, rMAE is much higher, exceeding 35% in some regions. Comparatively, oceanic WRF-CLDDA forecasts have rMAE from 17% to 23% and coastal rMAE of 23% to 33%. The improvement over the NAM is largest within 10 km of

the coast. These results indicate that for early morning hours, WRF-CLDDA more accurately predicts marine layer cloud cover especially in coastal regions. Later in the day, as marine layer clouds become less frequent, the difference in accuracy decreases. Notably, WRF-CLDDA forecasts greater than 30 km inland are very accurate (rMAE < 5%) regardless of time of day. This is due to infrequent cloud cover in inland regions.

5.3.3 Variability Error Metrics

Irradiance variability is characterized by ramp magnitude, duration, and frequency of occurrence. Defined as the change in irradiance divided by the time over which it occurs (Δt, Eq. 5.4), irradiance ramp rates are expressed in W m^{-2} $min.^{-1}$

$$RR_{\Delta t} = \frac{dGHI}{dt} \approx \frac{GHI\left(t + \frac{\Delta t}{2}\right) - GHI\left(t - \frac{\Delta t}{2}\right)}{\Delta t} \qquad \text{Eq. 5.4}$$

For each day, ramp rates were calculated for WRF-CLDDA, DEMROES data, and clear sky irradiance for Δt = 5, 10, 30, and 60 min. Daily observed variability statistics were derived by comparing the cumulative distribution functions (CDFs) of the observed and clear sky ramp rates. On highly variable days, observed ramp rate magnitudes are much larger than the reference clear sky ramp rates (Fig. 5.9b, inset). Consequently, the observed ramp rate CDF deviates significantly from the clear-sky ramp rate CDF. This difference is quantified using the Kolmogorov-Smirnov Integral (KSI, Beyer *et al.*, 2009) as the integrated difference between the CDFs of observed and clear-sky ramp rates (KSI_{CSK}, Eq. 5.5).

$$KSI_{CSK} = \int \left(CDF_{Obs.} - CDF_{CSK}\right) dRR \qquad \text{Eq. 5.5}$$

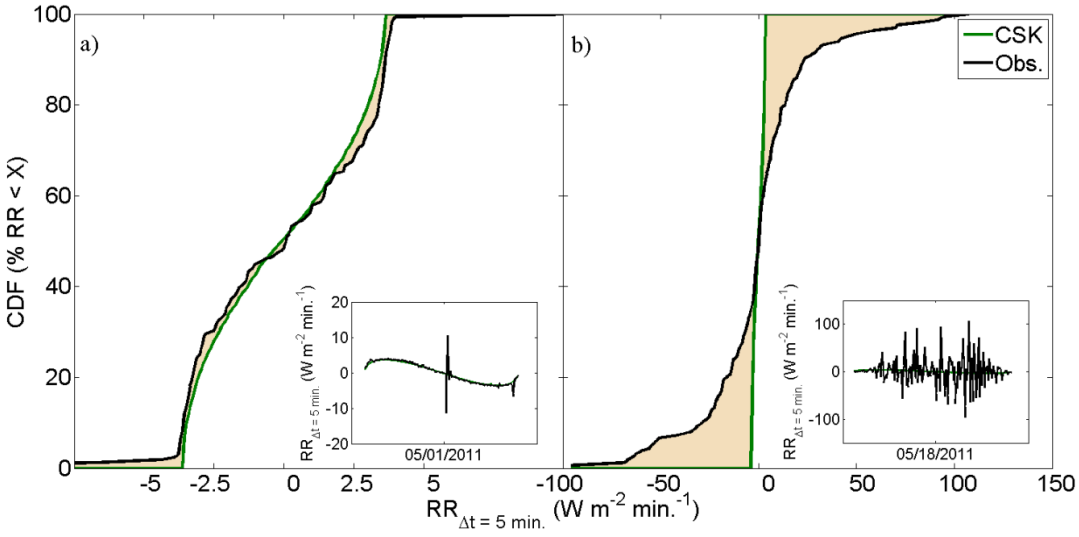


Fig. 5.9: KSI_{CSK} examples for a clear day (5/1/2011, a) and a highly variable day (5/18/2011, b). The main plots compare the CDF of observed (black line) and clear sky (green line) RR with KSI_{CSK} equal to the shaded area. Insets show the instantaneous 5-min. RR.

Fig. 5.9a depicts a day with little variability. Since the observed irradiance ramp rates match closely with clear-sky ramp rates, the difference between the CDFs and KSI_{CSK} (shaded area) are small. For a highly variable day (Fig. 5.9b), observed and clear sky ramp rates are significantly different and KSI_{CSK} is large. KSI_{CSK} was calculated for each day and Δt.

At high temporal resolutions it is unlikely that the exact timing of irradiance variability precisely matches observed. Small spatial offsets or phase errors can drastically affect forecast accuracy as measured by MAE or RMSE, even if the predicted cloud field characteristics are correct. Thus, directly comparing forecast to observed ramp rates does not necessarily produce an accurate assessment of model performance. Instead, the variability ratio (V, Eq. 5.6) was used to quantify the accuracy of predicted variability statistics.

$$V = \frac{\sum |RR_{WRF}|}{\sum |RR_{Obs.}|} \qquad \text{Eq. 5.6}$$

V is defined as the ratio of the sums of forecast and observed ramp rates. The variability ratio estimates if the distribution of forecast ramp rates is under- or over-dispersive. In general, highly variable days are more difficult (and often more important) to predict correctly. To determine how WRF-CLDDA performs as a function of observed variability, *V* was plotted against KSI_{CSK}. To directly compare *V* at different time-scales, KSI_{CSK} is multiplied by ramp duration (Δt).

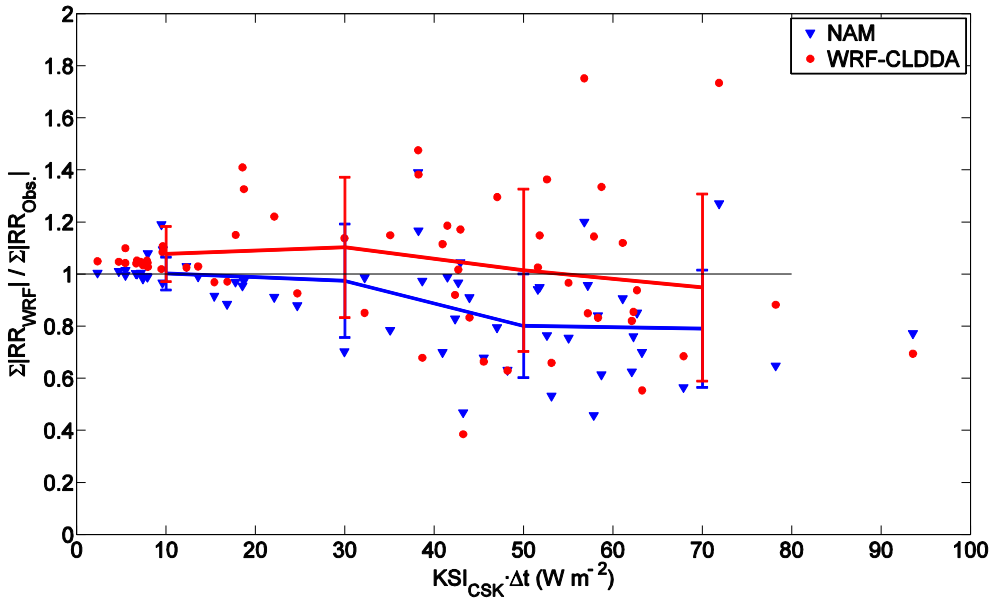


Fig. 5.10: Variability ratio (*V*, Eq. 5.6, *y*-axis) as a function of the daily variability statistic ($KSI_{CSK}\cdot\Delta$t) for NAM and WRF-CLDDA 60 min. ramp rates. Each dot represents a single day. Lines and bars indicate the mean and standard deviation of *V* in bins of 20 W m^{-2} on the *x*-axis.

Due to its hourly output, the NAM cannot resolve irradiance variability for Δt < 60 min. Even for hourly ramp rates, though, the NAM is slightly under-dispersive (Fig. 5.10) with average variability ratios of about 0.9. Only for days with little observed variability ($KSI_{CSK}\cdot\Delta t$ < 10 W m^{-2}) does the NAM accurately characterize hourly ramp rates. Additionally, for large KSI_{CSK}, the spread of *V* increases, indicating that for any particular day the variability could be over-predicted by up to 25% or under-predicted by 40%. Since spatial resolution determines the size of

resolvable cloud features, this implies that the NAM spatial resolution is too coarse to accurately resolve the cloud features that influence hourly irradiance ramp rates. Essentially, the spatial averaging that occurs over a single grid cell smoothes the variability characteristics of the predicted hourly irradiance time-series. Conversely, the 1.3 km horizontal resolution of WRF-CLDDA is fine enough to capture hourly variability characteristics. However, WRF-CLDDA is more likely to be over-dispersive (predicting too much hourly variability).

At finer time scales (Δt = 5 min.), however, WRF-CLDDA is consistently under-dispersive, especially for highly variable days (Fig. 5.11a). For $KSI_{CSK} \cdot \Delta t > 20$ W m^{-2}, WRF-CLDDA predicts less than half of the observed variability for Δt = 5 min ($V < 0.5$). For Δt = 10 min., WRF-CLDDA is again under-dispersive (Fig. 5.11b). However, days for which $KSI_{CSK} \cdot \Delta t < 15$ W m^{-2} are characterized accurately. Only for $\Delta t > 30$ min. (Fig. 5.11c) does WRF-CLDDA accurately characterize variability for all observed days. Physically, a ramp rate is dependent both on cloud speed and the time over which the ramp occurs. Generally, this can be related to the scale of cloud features that contribute to variability by $\Delta x = U_{Cloud} \cdot \Delta t$. For WRF-CLDDA, Δx = 1.3 km if clouds are being resolved with sizes on the order of the horizontal discretization. Assuming a typical cloud speed of 12.5 km hr^{-1} implies that WRF-CLDDA should resolve ramp rates with Δt as fine as 6.5 min. However, Fig. 5.11 suggests that the minimum resolvable Δt is 30 min. As such, using U_{Cloud} = 12.5 km hr^{-1} and Δt = 30 min., the actual resolved cloud features have a scale of 6.25 km, nearly 5 times larger than the model resolution of 1.3 km. Thus, to resolve irradiance ramp rates accurately at time scales of 5 min., a discretization size smaller than 1.3 km, possibly as small as 250 m, would be required.

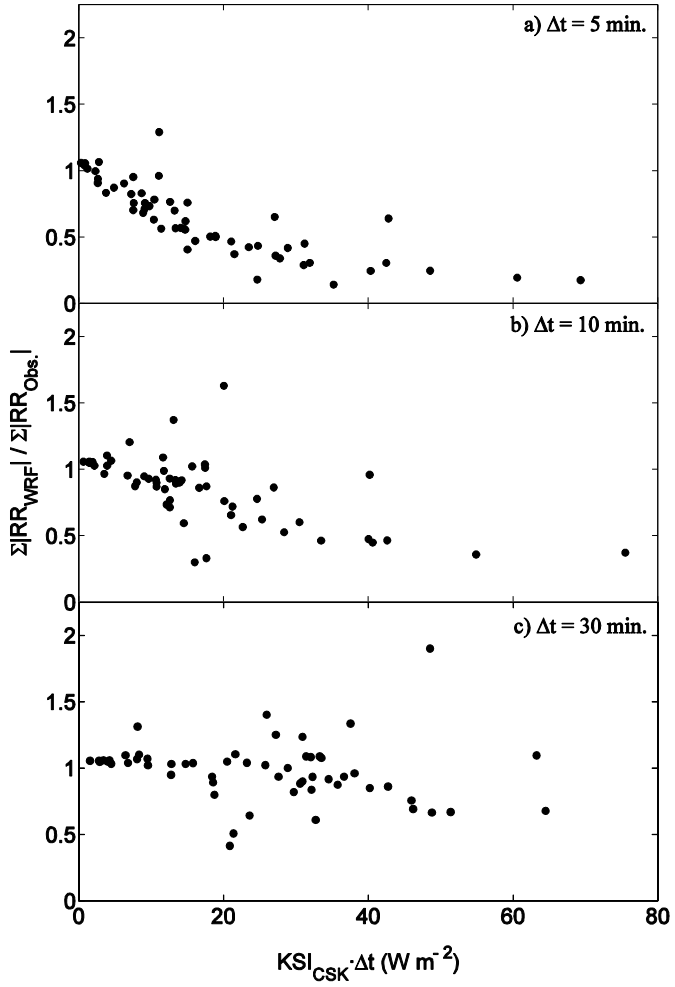


Fig. 5.11: Variability ratio as a function of the daily variability statistic ($KSI_{CSK}\cdot\Delta t$) for WRF-CLDDA ramp rates of Δt = 5 min. (a), Δt = 10 min. (b), and Δt = 30 min. (c). Dots represent single days.

5.4 Summary and Conclusions

To improve upon the operational NWP for solar irradiance forecasting, a high-resolution, cloud-assimilating NWP based on the Weather and Research Forecasting (WRF) model was implemented at the University of California, San Diego for solar irradiance forecasting. Fine horizontal (Δx = 1.3 km) and vertical resolutions were used to promote low-altitude cloud

formation. Additionally, a direct-cloud assimilation system was employed to populate the model initial conditions with cloud cover. To match GOES imagery, clouds were systematically added or subtracted from the model initial conditions by directly modifying the water vapor mixing ratio (q_v). Using this system, intra-day and day-ahead irradiance forecasts were created for 5/1/2011 and 6/30/2011 and validated against the dense UCSD pyranometer network.

Overall, WRF-CLDDA intra-day and day-ahead forecasts matched the observation distribution of clear sky index well, indicating that data assimilation correctly populated clouds in the initial conditions and that the model configuration accurately predicted the evening reformation of marine layer cloud cover, even though data assimilation had taken place more than 12 hours prior. Furthermore, WRF-CLDDA intra-day forecasts had rMBE of 0.4% compared to 17.8% for the NAM. Furthermore, rMAE was 21.3%, 4.1% smaller than the NAM. For day-ahead forecasts (> 24 hours), WRF-CLDDA accuracy did not degrade; rMAE was 18.2% and rSTDERR 27.5%. In general, NWP rMAE and rRMSE increase by 1%-3% between intra-day and day-ahead forecasts (Perez *et al.*, 2011). Here, however, it was that WRF-CLDDA accuracy slightly *increased* in day-ahead forecasts. As explored in Chapter 6, this artifact is potentially due to an incorrect soil moisture specification in the initial conditions. WRF-CLDDA derives its soil moisture initialization from the NAM. It will be shown that these initializations are biased dry which results in unphysically large Bowen ratios. Since MLS clouds frequently contain drizzle, moisture is provided to the surface throughout the day, facilitating lower Bowen ratios and longer cloud lifetimes for day-ahead forecasts. Overall, it was shown that by addressing the errors in the initial conditions and the physics parameterizations, forecast accuracy can be significantly improved.

Finally, the ability of WRF-CLDDA and the NAM to characterize irradiance variability was quantified. For one-hour ramp rates, it was found that the NAM is about 10% under-dispersive for all days, regardless of observed variability. In general, the NAM predicts 1 hr

ramp rates with less frequency and smaller magnitude than observed. Likely, this is because of the coarse discretization size of the NAM, where clouds of a small enough scale to affect the irradiance signal on 1 hr are not fully resolved. Conversely, WRF-CLDDA accurately predicted variability at Δt = 60 min. The ability of WRF-CLDDA to characterize variability at finer scales was also evaluated. For ramp rates with Δt < 30 min., WRF-CLDDA was under-dispersive, especially for highly variable days. Based on a typical cloud speed of 12.5 km hr^{-1} and a minimum resolvable ramp rate Δt of 30 min. it was determined that the model-resolved cloud length scale was approximately 6.25 km, nearly 5 times the horizontal discretization size. Thus, in order to accurately resolve ramp rates with Δt = 5 min., a model resolution of much finer than 1.3 km is required. Previous studies, however, have demonstrated that increasing model resolution generally reduces model accuracy (Zack, 2012). As spatial averaging increases, the random component of error is minimized and accuracy improved. The ability to accurately characterize variability, though, will also be diminished.

While high-resolution NWP forecasting with data assimilation was demonstrated for conditions typical of southern California, it is applicable with minor modifications to other regions and meteorological conditions. Changes in the cloud data assimilation procedure may be required, such as in the expected water content and cloud altitude. For instance, over other regions, the temperature inversion that is characteristic to marine layer stratocumulus clouds is not present. As such, satellite cloud height retrievals must be instead used to place the vertical location of the cloud. Cloud vertical extent can subsequently be derived from the expected cloud type; cumulus clouds can be built between the lifting condensation level and the reported cloud top and cirrus clouds can be assimilated by raising the water vapor content for a thin layer high in the atmosphere. By considering the local meteorology, the method of direct cloud assimilation presented here can be extended to many areas in order to improve solar irradiance forecasting.

5.5 Acknowledgements

The majority of this chapter has been published previously as Mathiesen *et al.*, 2013b.

Chapter 6 A WRF-Based Ensemble Forecasting System (WRF-SRAF)

Chapter 5 demonstrated that WRF-CLDDA outperformed the NAM and more frequently predicted MLS clouds over land. Furthermore, the diurnal cycle was more accurately characterized as WRF-CLDDA simulated the reformation of MLS clouds and their advancement over land. Though forecast performance improved considerably over the NAM, the timing of MLS cloud dissipation was inaccurately simulated for approximately 30% of simulations. On average, MLS dissipation occurred 1.9 hours early, resulting in a positive irradiance bias along the coast.

Historically, there thus exists some uncertainty in NWP-simulated MLS dissipation rates. For effective grid operations support this uncertainty must be predicted in operational forecasts. NWP models, however, are inherently deterministic. Outside of post-processing techniques (eg. Delle Monache *et al.*, 2011, Mathiesen *et al.*, 2013a), the most common method of establishing a probabilistic forecast using NWP is through ensemble forecasting (Larson, 2013). Generally, ensemble forecasts are created by running multiple iterations of a forecast model, each with a unique variation to represent the miscellaneous sources of uncertainty within the model. For instance, since the specification of the initial conditions is inexact, the initial conditions of each ensemble member can be independently perturbed. Simulation of the entire ensemble produces a diverse set of solutions that is representative of the model uncertainty (Toth and Kalnay, 1993). Alternatively, physics parameterizations that inaccurately characterize sub-grid scale processes contribute to model error. To simulate the uncertainty propagation as a result of these errors, multi-physics (Stensrud, *et al.*, 2000, Murphy *et al.*, 2004, Lopez-Coto *et al.*, 2014a) ensembles are used. Here, multiple physics parameterizations are used or modified to produce slightly different atmospheric interactions. Though the combination of the ensemble members is more accurate than any single member, the model dispersion, and therefore the forecast uncertainty, is

typically underestimated (Buizza *et al.*, 2005, Berner *et al.*, 2011). Since the MLS cloud dissipation rate is directly related to the ratio of the surface heat fluxes over land (the Bowen ratio, β), uncertainty in the land-surface model and its specification of β is assumed to be the dominant factor affecting uncertainty in the MLS dissipation rate. Thus, by perturbing β, an initial-condition ensemble with a variety of surface heat fluxes, atmospheric heating rates, and MLS dissipation rates can be established.

Using the mixed-layer principles outlined in Chapter 2, this chapter will establish the foundation for an ensemble forecasting system (WRF-SRAF) that corrects model bias and accurately characterizes the uncertainty in marine layer stratocumulus (MLS) dissipation rate to produce a dispersive set of irradiance signals useful for solar power forecasting. Using a two-dimensional idealized WRF configuration, the cloud dissipation model developed in Section 2.4 (Eq. 2.19) is validated for a variety of β. Furthermore, it is shown that outside of advection and entrainment, the surface sensible and latent heat fluxes have the largest influence on MLS cloud dissipation. Since β is primarily a function of soil moisture (q_g), the MLS dissipation bias and uncertainty is expressed as a function of the soil moisture. Using an initial condition ensemble that depends on variations in soil moisture, a dispersive set of irradiance signals useful for solar power forecasting is produced using WRF. For 30 days when MLS clouds were observed the results are validated using satellite solar irradiance data. The median ensemble member (P_{50}) improves coastal irradiance forecasts by up to 25 W m^{-2} and reduces the dissipation timing bias by 0.5 hours in coastal areas. Finally, the ensemble is applied to a MLS case study day and ensemble characteristics analyzed for May and June, 2011

6.1 WRF Configuration

In this chapter, the Weather Research and Forecasting (WRF) model version 3.4.1 (Skamarock *et al.*, 2008) was used to simulated cloud fields and solar irradiance at the surface.

Additional modifications to several physics parameterizations were provided by Joseph Olson of the Earth System Research Laboratory (ESRL) at the National Oceanic & Atmospheric Administration (NOAA). This version is consistent with the operational Rapid Refresh (RAP) and High-Resolution Rapid Refresh (HRRR) models (Benjamin *et al.*, 2006, Benjamin *et al*., 2013). To expedite the simulations, WRF was configured with a single 2.5 km domain centered at the University of California, San Diego (Fig. 6.1).



Fig. 6.1: WRF domain configuration (Δx=2.5 km) centered at the University of California, San Diego. Image created using Google Earth.

As forecast accuracy generally increases with vertical resolution (Tselioudis and Jakob, 2002), the domain was configured with 75 terrain-following vertical levels. To further facilitate the formation of the low-level stratocumulus clouds ubiquitous to coastal California (Sec. 2c), 50 vertical levels were concentrated below 3000 m. To ensure numerical stability, the time-step size was defined dynamically using a Courant-Friedrichs-Lewy (CFL) criterion of 0.3.

Additionally, the choice of physics parameterizations can have a large impact on the characteristics of simulated cloud fields (Otkin and Greenwald, 2008, Lopez-Coto *et al.*, 2014a). Previously, Lopez-Coto *et al*. (2014a) found that the choice of cumulus parameterization has the largest influence on the simulated cloud field. In this study, even the relatively fine horizontal resolution of 2.5 km insufficiently resolves vertical mixing. As such, the New Simplified Arakawa-Schubert (NSAS, Han and Pan, 2011) cumulus scheme was implemented and invoked every time step to ensure that deep convection was accurately resolved. Since cloud-top radiative cooling is the driving force behind the persistence of coastal stratocumulus clouds (Sec. 2c), the choice of radiation scheme is the second most influential physics parameterization (Lopez-Coto *et al.*, 2014a). Here, both longwave and shortwave radiation were calculated every five minutes using the new Goddard radiation transfer model (Chou and Suarez, 1999, Chou and Suarez, 2001). Additionally, the Morrison double-moment microphysics scheme (Morrison *et al.*, 2005) was used to explicitly predict the interaction of six hydrometeor classes (water vapor, cloud water, rain, ice, graupel, and snow) and their number concentration.

As this chapter examines the relationship between the soil moisture content and the simulated cloud field, the interaction between the surface and the planetary boundary layer (PBL) is especially critical to consider. Turbulent mixing propagates heat and moisture from the surface throughout the PBL which directly impacts cloud formation and evaporation. Here, turbulent mixing was parameterized using the Mellor-Yamada-Nakanishi-Niino scheme (MYNN, Nakanishi and Niino, 2006). The PBL is coupled to the surface through surface sensible and latent heat fluxes. These are calculated using the six-layer Rapid Update Cycle Land-Surface Model (RUC-LSM, Smirnova *et al.*, 1997). In general, the RUC LSM predicts lower Bowen ratios (Eq. 2.11, where Q_H (Q_E) is the sensible (latent) heat flux) than the Noah LSM (Ek *et al.*, 2003) which results in smaller sensible heat fluxes and longer cloud lifetimes.

For all simulations, boundary conditions were provided by North American Mesoscale Model (NAM) data (Janjic *et al.*, 2010, Janjic *et al.*, 2011). In addition to atmospheric variables such as temperature, humidity, wind, and pressure, soil temperature and volumetric moisture content at four depths is derived from the NAM data. Simulations were run in a 24 hour cycling model; the final output from the previous day was used to initialize the model for the forecast period and no data assimilation was used. The complete WRF configuration is summarized in Table 6.1.

Table 6.1: Summary of WRF Configuration

Domain/Time Options		**Physics Options (WRF Option #)**	
Δx (km)	2.5	*Cumulus*	NSAS (14)
Vertical Pts.	75	*Radiation*	New Goddard (5)
CFL	0.3	*Microphysics*	Morrison (10)
Output Interval (m.)	15	*PBL*	MYNN (5)
Spin-Up Interval (hr.)	24+ (Cycling)	*LSM*	RUC (3)
Initial and Boundary Cond.	12 UTC NAM		

Additionally, a 2-D idealized WRF model was used to validate the analytical cloud dissipation model (Chapter 2.4, Eq. 2.19). Unlike the full model (Table 6.1), phase-change latent heating and precipitation from the Morrison scheme was disabled. Furthermore, the 2-D model used flat topography, no oceanic cells, and identical soil and surface properties throughout the domain. In this configuration, uniform surface heating occurred and no horizontal pressure gradients formed. Additionally, as the boundary conditions were periodic and the simulations initialized with zero wind, no horizontal advection occurred. In this way, the effect of surface heating on the cloud dissipation rate can be validated independent of other factors such as horizontal advection and phase-change latent heating. The initial conditions (15 June 2011 1200 UTC radiosonde from Miramar KNKX) contained a strong temperature inversion and typical MLS cloud vertical extent. Satellite data showed MLS to dissipate steadily from about 40 km

inland at sunrise to the coast line at 1200 PST. Therefore this was an ideal day to test the analytical cloud dissipation model.

6.2 Validation of Mixed-Layer Cloud Dissipation Model

In Chapter 2.4, an analytical expression for the cloud dissipation rate as a function of the surface heat fluxes and Bowen ratio (β) was derived (Eq. 2.19). To validate this, β was varied in a simplified two-dimensional WRF model and the simulated cloud dissipation rate was compared to the analytical cloud dissipation expression derived in Chapter 2.4 (Eq. 2.19). Since advection, phase-change latent heating, and precipitation were suppressed, the simulated cloud dissipation rate was only a function of radiative heat transfer and surface heat fluxes. While radiative heat transfer could also have been disabled, doing so would have inhibited the dynamics that drive stratocumulus formation – cloud top radiative cooling. However, WRF output explicitly provides the air temperature tendency due to radiative heat transfer ($dT\ dt^{-1}|_{Rad.}$). To isolate $d\langle q_L\rangle\ dt^{-1}$ due to the surface heat fluxes, $dT\ dt^{-1}$ on the right hand side of Eq. 2.12 was split into the individual contributions due to radiative heat transfer and surface heat fluxes ($dT\ dt^{-1} = dT\ dt^{-1}|_{Rad.} + dT\ dt^{-1}|_{Sfc.}$). The $d\langle q_L\rangle\ dt^{-1}$ contribution due to radiative heating ($dq_S\ dT^{-1} \cdot dT\ dt^{-1}|_{Rad.,zi}$, Eq. 2.12) was subtracted from the total simulated cloud dissipation rate ($d\langle q_L\rangle\ dt^{-1}$, Eq. 2.19) to segregate the simulated cloud dissipation rate due to the surface heat fluxes alone.

For each simulation, $\langle q_L\rangle$ was greatest shortly before sunrise (Fig. 6.2a). Small differences in pre-sunrise Q_E and Q_H resulted in slightly different simulated $\langle q_L\rangle$ before 0600 PST. As incident solar radiation increased, $\langle q_L\rangle$ decreased and reached a minimum in the afternoon (1500 - 1600 PST). As expected, simulations with the lowest daily $\langle q_L\rangle$ mimina corresponded to high Bowen ratios and most PBL heating at 1200 PST (red lines in Fig. 6.2b). Overall, the simulated cloud dissipation rates ($d\langle q_L\rangle\ dt^{-1}$) matched the analytical cloud dissipation model with a correlation coefficient of 0.994 (Fig. 6.3, Eq. 2.19), indicating (as expected) that the contribution to the cloud dissipation rate from the surface can be approximated

solely by the surface fluxes. Notably, for large β, simulations deviate slightly from analytical when inhomogeneous heating occurs within the PBL. Generally, this occurs as air near the surface heats more quickly (Fig. 6.2b) and indicates that the PBL is not well mixed. When averaged for the period between $<q_L>$ maxima and mimina, (Fig. 6.3, inset), the relationship between β and $d<q_L> dt^{-1}$ is confirmed; larger β result in larger cloud dissipation rates.

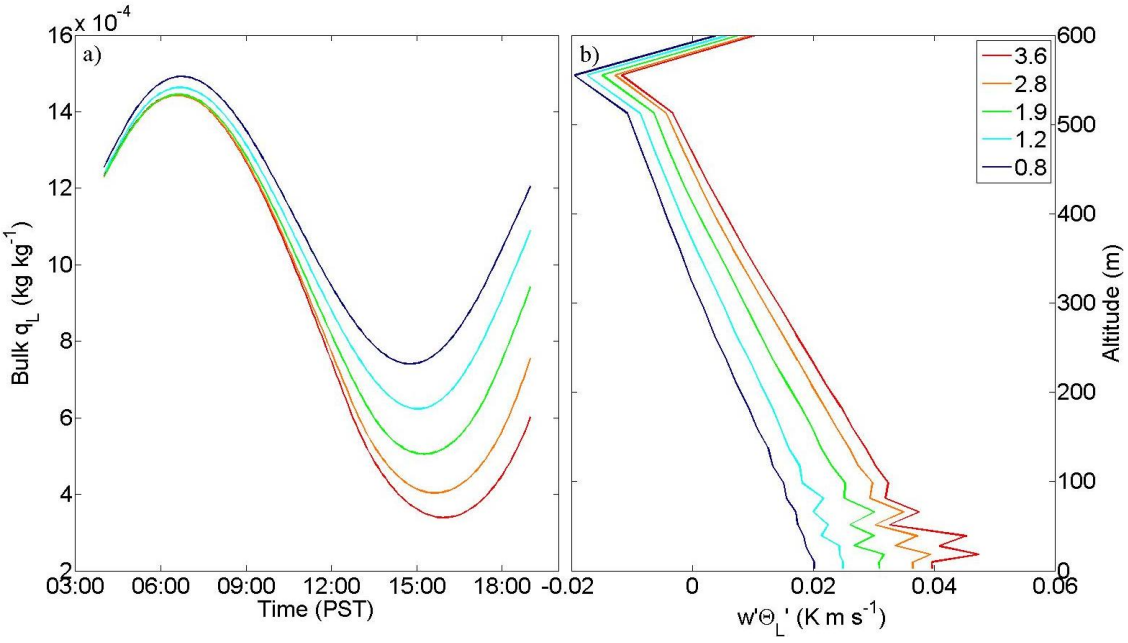


Fig. 6.2: Simulated vertically-averaged cloud water mixing ratio (a, $<q_L>$) as a function of time and Bowen ratio (β, legend) and simulated horizontally-averaged $w'\theta_L'$ heating profiles (b, at 1200 PST) using the simplified 2-D WRF model. Near the surface, inhomogeneous heating occurs for large β.

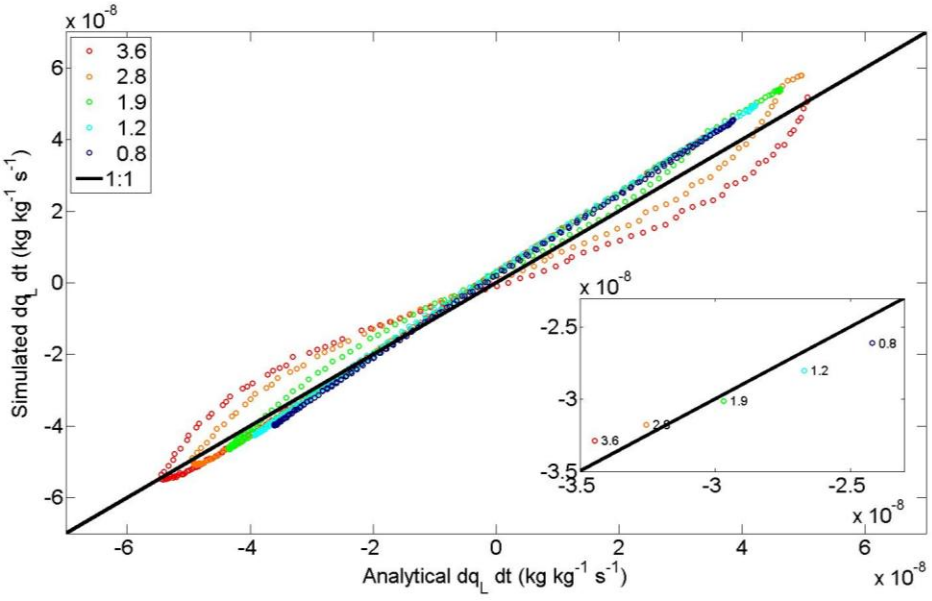


Fig. 6.3: WRF-simulated $d\langle q_L \rangle\, dt^{-1}$ compared to analytical $d\langle q_L \rangle\, dt^{-1}$ as derived from the mixed layer model (Eq. 2.19) for vertically-averaged PBL variables for all data in Fig. 6.2a. Inset (same axes) shows the average values over the period of cloud dissipation (maximum to minimum in Fig. 6.2), where labels indicate the Bowen ratio of the simulation.

6.3 Influence of Non-Idealized Conditions

In reality, however, the influence of other physical processes must be included and Eq. 2.19 is only a single component of the total change in LWP. Surface heat fluxes, cloud radiative fluxes, latent heating from water phase changes, and advection are all important for the vertically-averaged potential temperature ($d\langle\theta\rangle\, dt^{-1}$) and liquid-water ($d\langle q_L \rangle\, dt^{-1}$) tendencies. For instance, precipitation (primarily drizzle) removes water from the PBL, reducing q_T and partially offsetting the effects of Q_E. Alternatively, advection can remove or add water to the PBL (e.g. dry air entrainment at the cloud top mixes dry air into the PBL, lowering q_T). Fig. 6.4 shows the WRF-simulated (non-idealized configuration) tendencies for 15 June 2011 when averaged throughout the coastal corridor (within 30 km of the coast). Over the ocean (Fig. 6.4a/c), PBL potential temperature and liquid water tendencies are primarily dependent on advection (cyan). By 1100 PST, the $\langle q_L \rangle$ advection tendency is largely negative (Fig. 6.4c), indicating dry air entrainment.

Overall, advection accounts for 73% of the change in cloud water content over ocean (Table 6.2). Outside of advection, cloud-top radiative cooling provides the primary temperature forcing which reduces q_S and slightly increases cloud water content (magenta line in Fig. 6.4c). Radiative forcing is strongest before sunrise (0400 PST) and decreases with increasing incident solar radiation (0500-0900 PST). In total, radiative forcing is responsible for 6.3% of the change in $<q_L>$. Additionally, since the temperature of the ocean surface is cool throughout the day the surface sensible heat flux has little impact on the temperature of the PBL (red) over the ocean.

Over land (Fig. 6.4b/d), advection is similarly important and accounts for 59% of the $<q_L>$ tendency (Table 6.2). The influence of the seabreeze is evident as the advective component of the potential temperature tendency is strongly negative after sunrise (Fig. 6.4c) as cool oceanic air is advected over land. For radiation, the cloud-top cooling is similar to the radiative tendency observed over water and accounts for 2.8% of the total cloud water tendency. Before sunrise (0600 PST), radiative cooling is larger than the slightly positive sensible heat flux and the PBL is cooling. After sunrise, the surface heat fluxes that increase with increasing incident solar radiation are the only contributor to increasing PBL potential temperatures. Together, the sensible and latent heat flux account for 37% of the total cloud water tendency over land. Dry-air entrainment and advection, however, is the most influential physical process, accounting for 47% (three times larger than the surface sensible heat flux) of the cloud water tendency. In general, phase-change latent heating (1.0%) and precipitation (0.3%) are minor contributors.

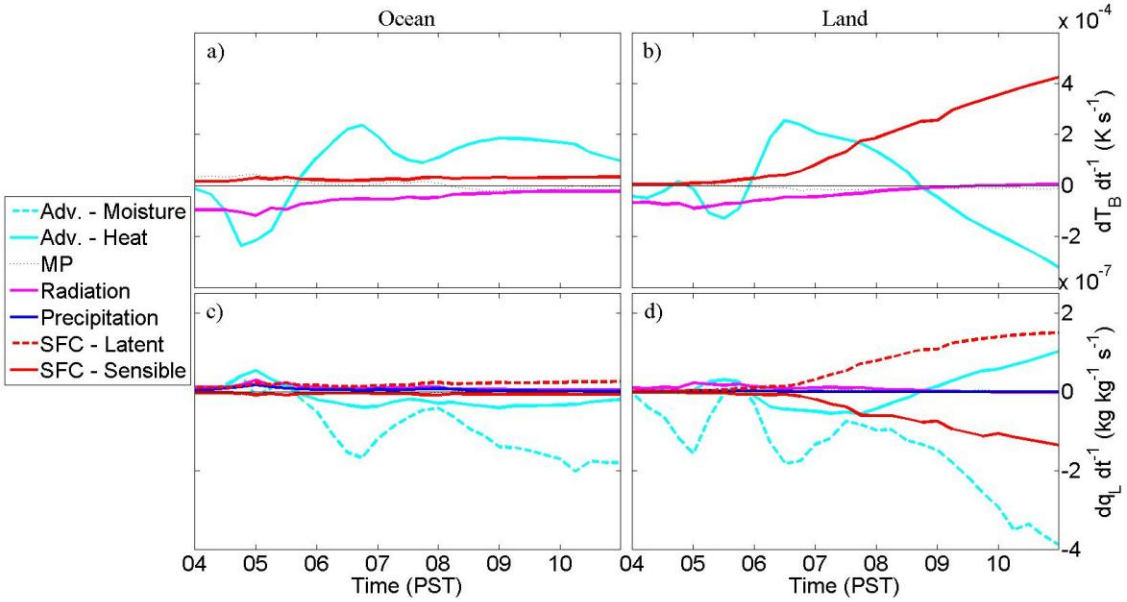


Fig. 6.4: WRF-simulated vertically-averaged potential temperature tendency ($d\langle\theta\rangle\, dt^{-1}$) and corresponding liquid water tendency ($d\langle q_L\rangle\, dt^{-1}$) partitioned by source for the ocean (a/c) and land (b/d) on 15 June 2011 with average Bowen ratios of ≈1.5 (land) and ≈0.6 (water). Over land, cloud dissipation occurs at 1100 PST.

Table 6.2: Vertically averaged liquid water tendency ($d\langle q_L\rangle\, dt^{-1}$) partitioned by source for 15 June 2011 between 0400 and 1100 PST. Percentages are calculated by taking the absolute values of the $\langle q_L\rangle$ tendencies.

Factor	Oceanic (% Total)	Land (% Total)
Advection - Moisture	56.3	47.7
Advection - Heat	16.9	11.7
MP Latent Heating	1.8	1.0
Precipitation	3.7	0.3
Radiation	6.3	2.8
Surface - Latent Heat Flux	11.9	20.8
Surface - Sensible Heat Flux	3.2	15.8

6.4 Ensemble Composition and Bowen Ratio Uncertainty

On days when MLS clouds dissipate, there exists some observed average cloud dissipation rate ($\langle dq_L\, dt^{-1}|_{Obs.}\rangle$, Eq. 6.1) given the WRF-simulated initial cloud water content. The deviation between this and the corresponding average simulated cloud dissipation rate ($\langle dq_L\, dt^{-1}|_{WRF}\rangle$, Eq. 6.2) is the dominant source of model solar irradiance bias error. Here, t_0 defines the

time at which the cloud is at its maximum extent and generally occurs just before sunrise. Aggregating bias statistics over two months of simulations, Fig. 6.5 shows the median error in WRF-simulated cloud dissipation time (a) when compared to SolarAnywhere data and corresponding error in average cloud dissipation rate (b). Averaged over all times and locations, WRF-simulated MLS clouds dissipate 1.9 hours earlier than observed over land. This is consistent with previous studies (Mathiesen *et al*., 2013a, Mathiesen *et al.*, 2013b) which demonstrated that, in coastal areas, NWP irradiance forecasts generally predict too few clouds. For inland regions at the maximum extent of MLS clouds (≈35 km from the coast) WRF-simulated clouds dissipate quickly and the cloud dissipation rate is much larger than observed. Near the coast (<10 km), WRF-simulated clouds persist for longer and the timing bias error is less than 30 minutes.

$$\left\langle \left. \frac{dq_L}{dt} \right|_{Obs.} \right\rangle = \frac{q_{L,0}}{t_{Obs.} - t_0} \qquad \text{Eq. 6.1}$$

$$\left\langle \left. \frac{dq_L}{dt} \right|_{WRF} \right\rangle = \frac{q_{L,0}}{t_{WRF} - t_0} \qquad \text{Eq. 6.2}$$

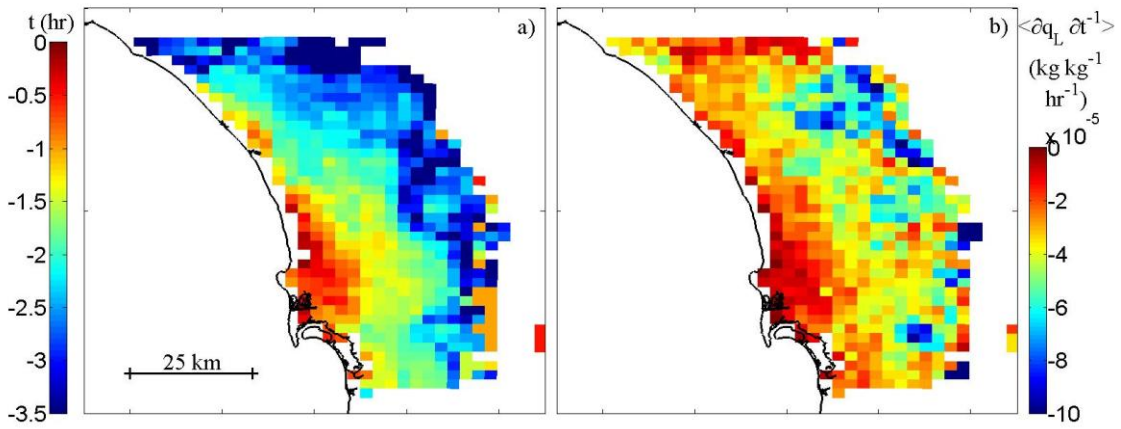


Fig. 6.5: Median bias (WRF – satellite observed) of cloud dissipation time (a, hr) and average cloud dissipation rate (b, kg kg^{-1} hr^{-1}) for MLS days in May and June, 2011. For days and locations in which no clouds are observed or simulated, no dissipation rate is calculated. Oceanic data and locations with no cloud cover were ignored (white areas).

Since the cloud dissipation rate increases with β (Eq. 2.19) and the sensible heat flux is the largest term in the daytime heat balance (Fig. 6.4a), Fig. 6.5b suggests that the WRF-simulated sensible heat fluxes are generally too large. For each day and location, an ideal average (over the observed cloud dissipation period) Bowen ratio ($\beta_{Idl.}$) was calculated from Eq. 2.19 using the observed average cloud dissipation rate (Eq. 6.1). It was assumed that the individual cloud water tendencies ($d\langle q_L \rangle\, dt^{-1}$) due to advection, precipitation, radiation, and phase-change heating would not change when the surface heat fluxes were altered. Next, the cumulative error distribution of Δβ ($\Delta\beta = \beta_{WRF} - \beta_{Idl.}$) was calculated and is shown in Fig. 6.6 at three γ-percentiles, 10% (Fig. 6.6a), 50% (Fig. 6.6b), and 90% (Fig. 6.6c). Here, $\Delta_\gamma\beta$ represents the γ-percentile of the Δβ distribution where (1-γ)% of all Δβ exceed the $\Delta_\gamma\beta$ percentile (e.g. $\Delta_{90}\beta = 4$ states that 10% of all Δβ exceed 4).

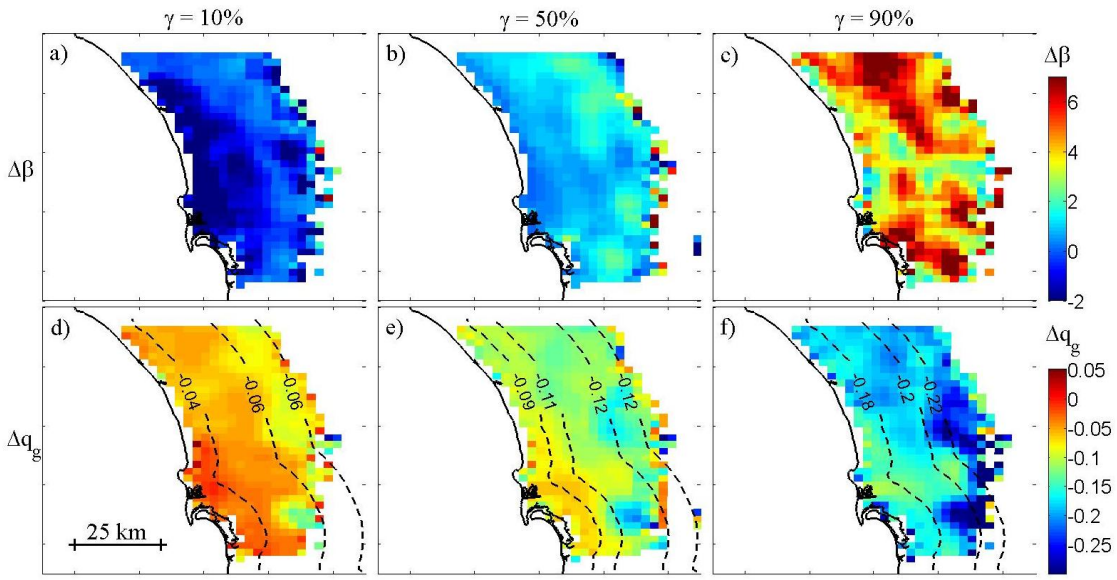


Fig. 6.6: May and June 2011 error distribution of β (a-c) and q_g (m^3 m^{-3}, d-f) at three γ (percentile) levels: 10% (a/d), 50% (b/e), and 90% (c/f). Dashed contours (d-f) show distance-averaged Δq_g. Negative $\Delta_\gamma q_g$ indicate that the soil is too dry.

On average, WRF-simulated β are 2.2 larger than $\beta_{Idl.}$ confirming that WRF-simulated sensible heat fluxes are too large to accurately simulate the dissipation of MLS clouds. For greater than 10% of forecasts, β_{WRF} are approximately 7 larger than ideal (Fig. 6.6c). Near the coast, where average cloud dissipation error is lowest, this error is smallest and coastal WRF-simulated β are too small for about 10% of forecasts (Fig. 6.6a). Inland, where WRF-simulated cloud dissipation times are most biased (Fig. 6.5a), the β deviation is largest. Overall, β uncertainty ($\gamma_{90} - \gamma_{10}$) is largest greater than 10 km from the coast. In this area, observed average cloud dissipation rates vary significantly day-by-day. At the coast, where WRF-simulated forecasts are most accurate, the β uncertainty is lowest.

Sensible heat fluxes are a function of the temperature gradient at the land surface interface and associated resistances while latent heat fluxes are a function of the water vapor gradient. Additionally, latent heat is influenced by vegetation properties such as stomatal conductance and root depth, but these complexities are greatly simplified within WRF. The

surface soil moisture content (q_g m^3 m^{-3}) and relative soil moisture (RSM) appears in the denominator for the Bowen ratio (Eq. 6.3).

$$\beta = \frac{R_q}{R_\theta} \frac{\left(\theta_g - \theta_a\right)}{M^2\left(q_{s,g} - q_a\right)} \qquad \text{Eq. 6.3}$$

Here, R_q over R_θ is the WRF-parameterized ratio of moisture to thermal resistances and is approximately equal to 0.000135. θ_g and θ_a are the ground and 2 m air temperature while $q_{S,g}$ is the saturated ground water mixing ratio and q_a is the water vapor mixing ratio of air at 2 m. *RSM* describes the relative q_g value within the range of soil moisture from the wilting point (*RSM* = 0, $q_{g,Dry}$) to saturation (*RSM* = 1, $q_{g,Max}$). For soil moisture at saturation (*RSM* ≈ 1), latent heat fluxes dominate and β approaches a practical lower limit. For instance, β ≈ 0.1 over the ocean in near thermal equilibrium conditions. For very dry conditions, the latent heat flux approaches zero and β becomes large. Though β rarely exceeds 6 in observations for arid regions, 21.6% of WRF-simulated β for land areas are greater than 10 (Fig. 6.8, later). In principle, large β are expected during the summer in coastal California. During this time, precipitation is zero (the most recent rain event recorded at the San Diego International Airport (KSAN, 117.186° W, 32.733° N) occurred on 8 and 9 April 2011 with 3.8 mm, 22 days before the start of the trial period and substantial incident solar radiation causes continuous evapotranspiration which dries the soil and root zone. However, in southern California the soil receives water through widespread irrigation (inhabited areas) and nighttime condensation of marine layer fog. In addition, the coastal areas are vegetated with plants that can access deep-soil moisture and therefore are less affected by drying of the top soil layers. As such, the large WRF-simulated β are likely due to abnormally low soil moisture content and suggest a deficiency in the soil initial conditions as derived from the NAM. Unfortunately, latent and sensible heat flux measurements are sparse and limited to non-representative riparian ecosystems (e.g. Baldocchi *et al.*, 2001). Similarly, there are no soil

moisture measurements for coastal California known to the authors and it is therefore difficult to ascertain the physically correct soil moisture or Bowen ratios.

To adjust β_{WRF}, the initial soil moisture content was modified for each simulation (i.e. every 24 hours at 12 UTC). Soil moisture content can be derived from β_{WRF} if the surface parameters (such as the dry and moist limits on q_g) are known (Eq. 6.3, Fig. 6.6d/e/f). q_g was increased (decreased) where β was too large (small). The ensemble was created by initializing members with different soil moisture contents that represent the soil moisture error distribution (Fig. 6.6d/e/f). For each ensemble member, the initial soil water content was modified according to Eq. 6.4.

$$q_{g,WRF} = q_{g,NAM} + \Delta_{\gamma}\left(q_g\right) \quad \text{Eq. 6.4}$$

Here, $\Delta_{\gamma}(q_g)$ is the change in soil moisture content for a specific γ-percentile and is obtained directly from the $\Delta(q_g)$ error distribution. For instance, $\Delta_{10}(q_g)$ is the change in soil moisture that represents the 10th percentile in the q_g error distribution (Fig. 6.6d). Correspondingly, GHI forecasts using the Δ_{10} soil adjustment contain the driest surface conditions and are expected to have the lowest cloud water content. Furthermore, irradiance forecasts using the Δ_{10} soil adjustment are expected to be very large and should, on average, be exceeded by GHI observations for only 10% of forecasts – the P_{10} forecast.

6.5 WRF-SRAF Ensemble Validation

6.5.1 Ensemble Case Study

For May and June, 2011, WRF simulations were produced with NAM-provided initial conditions adjusted at three γ levels (0.1, 0.5, 0.9) according to Eq. 6.4. An example irradiance forecast is provided for La Jolla (117.23° W 32.88° N) on 15 June 2011 in Fig. 6.7.

Corresponding to the smallest β, the P_{90} forecast (Fig. 6.7, blue thin-dashed line) has the slowest rate of cloud dissipation and lowest irradiance at the surface. In fact, P_{90} simulated clouds never fully dissipate. Furthermore, since the P_{50} forecast shows similar cloud water content as the P_{90} forecast, the P_{50} surface is likely near saturation. Conversely, the P_{10} forecast has the largest β and surface sensible heat fluxes, resulting in faster cloud dissipation and larger irradiance than the other members. This is similar to the unperturbed WRF forecast (black line). Comparatively, the NAM forecast (blue dashed line) predicts no clouds and irradiance matches clear conditions for the entire day. Further post-processing could be applied to determine ensemble weights and probabilistic forecasts via various statistical methods (Lopez-Coto *et al*., 2014b) but this is beyond the scope of this chapter.

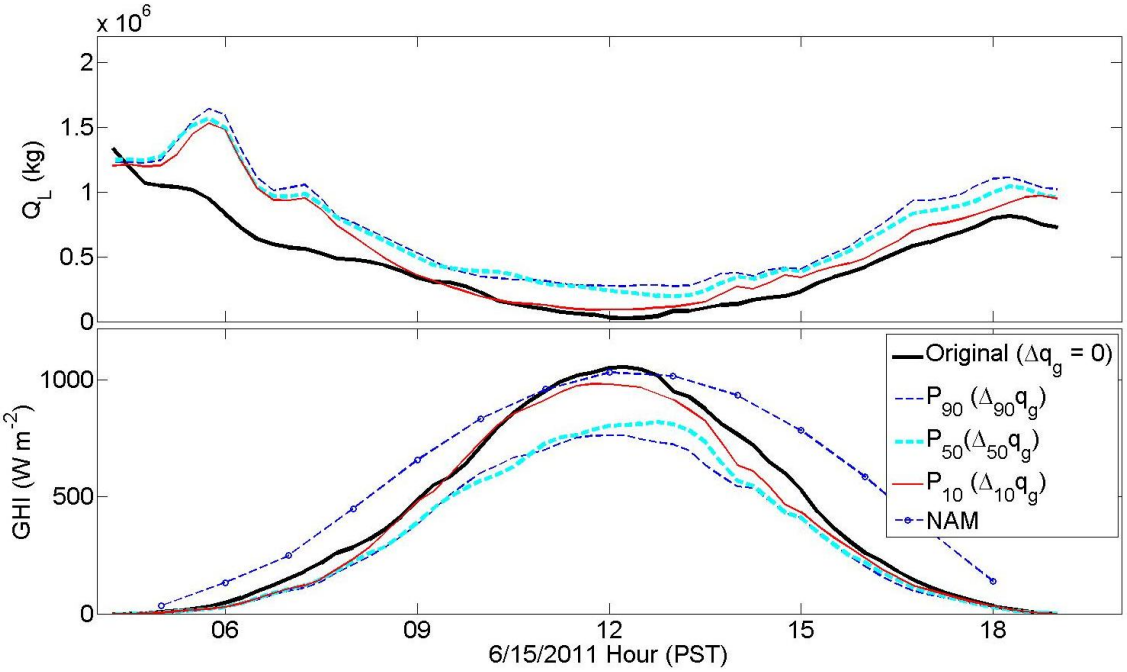


Fig. 6.7: Example columnar cloud water content (a, kg) and resulting irradiance (b, W m^{-2}) forecast for 15 June 2011 at La Jolla, CA (117.23° W 32.88° N – red circle in Fig. 6.9, later) using the WRF cloud lifetime ensemble.

6.5.2 Accuracy Improvement and Dispersion Analysis

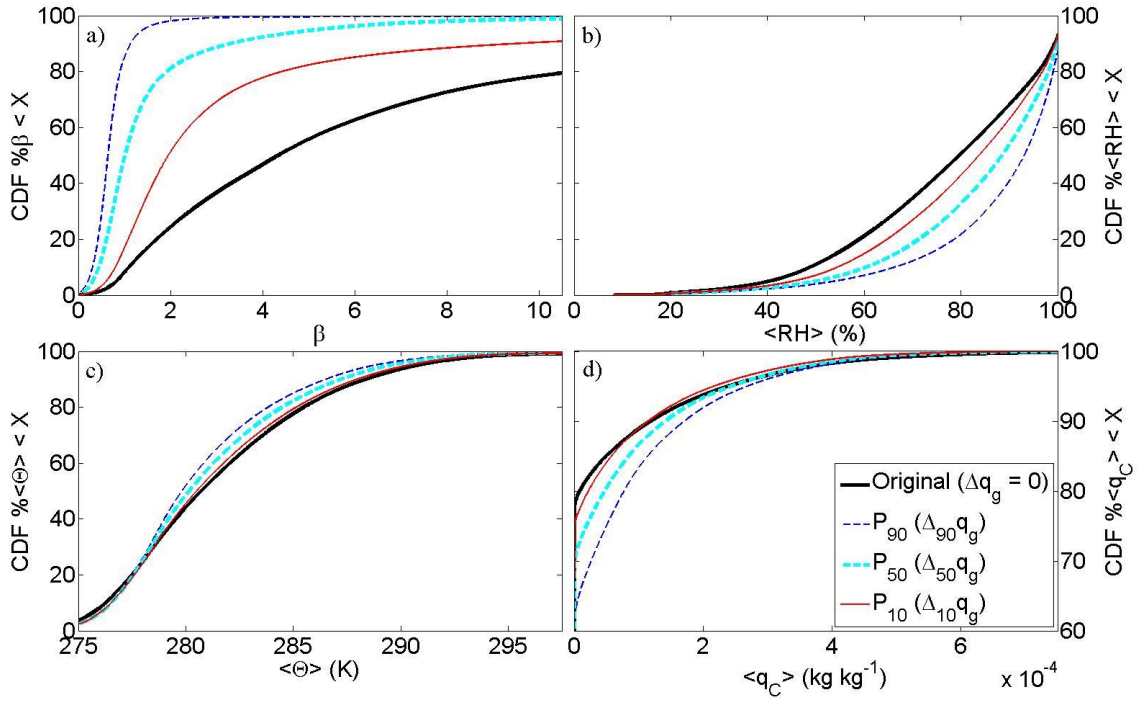


Fig. 6.8: Cumulative distribution functions (CDFs) of simulated β (a), vertically-averaged relative humidity (b), vertically-averaged potential temperature (c), and vertically-average cloud-water mixing ratio (d) for original forecasts with NAM-provided soil moisture contents (black thick-solid line) compared to ensemble members with adjusted soil moisture contents. Only locations within 30 km of the coast were considered.

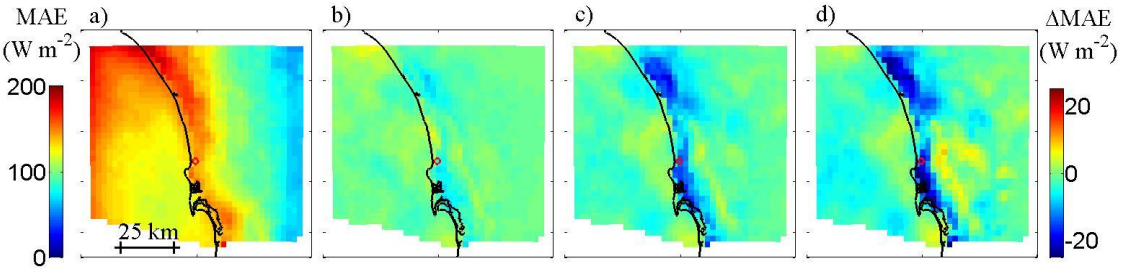


Fig. 6.9: MAE (W m^{-2}) of WRF forecasts with NAM-provided soil moisture contents (a) and ΔMAE for P_{10} (b), P_{50} (c), and P_{90} (d) forecasts on MLS days in May and June, 2011. Forecast improvement is largest within 15 km of the coast. Red circles denote La Jolla, CA.

In general, β were more realistic for the soil-adjusted simulations. In fact, only 1.2% of P_{50} β exceeded 10 compared to 21.6% previously (Fig. 6.8a, cyan thick-dashed line). As β decreases, latent heat fluxes increase and sensible heat fluxes decrease. As such, the vertically-

averaged relative humidity increases with soil moisture perturbation (Fig. 6.8b). Additionally, PBL temperatures were generally coolest for P_{90} simulations as less energy was devoted to sensible heating (Fig. 6.8c, blue thin-dashed line). Subsequently, cloud cover frequency and total cloud-water content was greater for all soil-adjusted simulations compared to the NAM. For the P_{90} forecast, 16% more forecasts contained clouds (Fig. 6.8d, blue-thin dashed line). Additionally, WRF GHI forecasts (unmodified and adjusted soil moisture) were compared to SolarAnywhere data (Fig. 6.9). Inland, cloud dissipation occurs in the early morning when GHI is small. As such, even large dissipation rate errors (Fig. 6.5) can result in low MAE (Fig. 6.9a). At the coast, however, MLS dissipation occurs when irradiance is large, meaning that even small errors in dissipation timing will result in large MAE.

Compared to WRF simulations with NAM-provided soil moisture content (Fig. 6.9), MAE was reduced for P_{10}, P_{50}, and P_{90} forecasts (Fig. 6.9b-d). Overall, MAE was improved for P_{50} forecasts by approximately 25 W m^{-2} for areas within 15 km of the coast (Fig. 6.9c), corresponding to the least accurate regions of the original forecast (Fig. 6.9a). Since MLS spatial extent is limited by topography, little improvement was observed inland. Despite this increase in accuracy, P_{50} cloud dissipation occurred 1.4 hours too early, an improvement of only 0.5 hours (Fig. 6.10). In general, accuracy increased with soil moisture content. The P_{90} forecast (Fig. 6.9d and Fig. 6.10, blue thin-dashed line) had MAE improvements of 30 W m^{-2}. However, P_{90} q_g approach saturation and β are frequently less than 1 (Fig. 6.8, blue thin-dashed line) which is likely unrealistic. Even in this limiting case, cloud dissipation times were about 1.0 hours early indicating that other factors (Table 6.2), notably dry-air entrainment, significantly contribute to cloud dissipation.

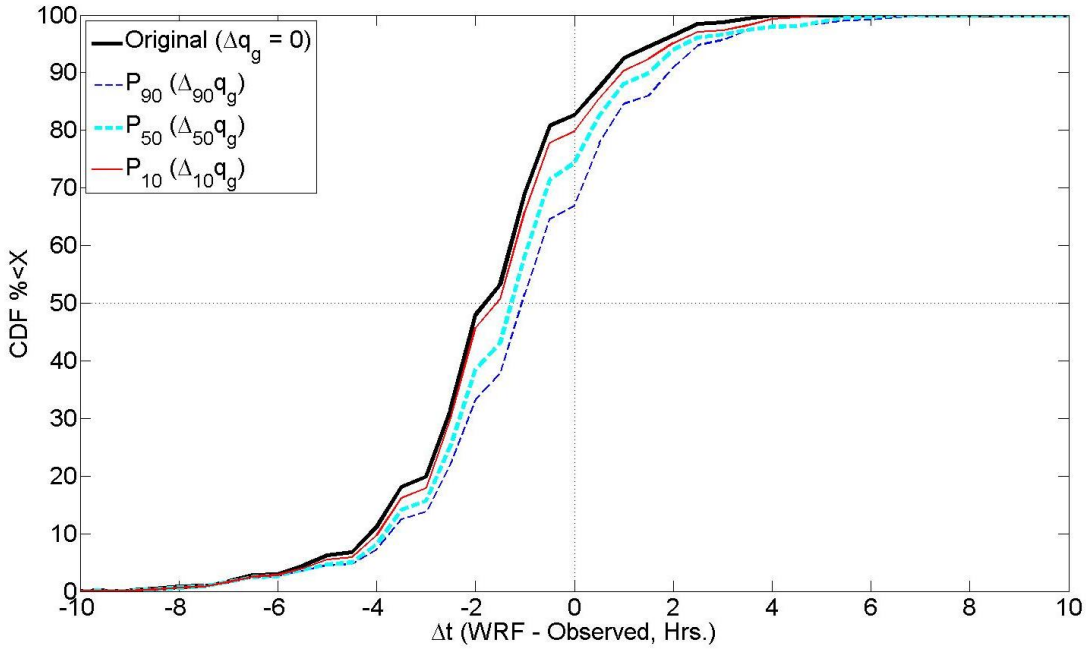


Fig. 6.10: The dissipation timing bias cumulative distribution functions (CDFs) for original forecasts with NAM-provided soil moisture contents (blue thin-dashed line) and the P_{50} ensemble member with adjusted soil moisture contents (red thin-solid line) for all locations (e.g. Fig. 6.5).

For an effective solar forecasting ensemble, inter-member irradiance dispersion must be large. For this ensemble, forecast spread was largest in the morning and evening hours near the coast (Fig. 6.11: Forecast clear sky index spread (*P10 – P90*) as a function of time of day and distance to coast.Fig. 6.11). Here, the models simulate diverse cloud dissipation/formation rates and forecast spread is 12% of GHI_{CSK} on average. Correspondingly, observed clouds are more common and forecasts more uncertain in the morning and evening (Mathiesen *et al.*, 2013b). Further inland, where clouds are rare, the models agree and average forecast dispersion is very small. Overall, however, the ensemble is largely under-dispersive when compared to observations. Specifically, β is physically constrained between about 0.1 and 6 by the saturated and dry limits of soil moisture content. As such, the influence of the surface-flux influence on cloud dissipation rate (Eq. 2.19) reaches a limit and further changes in soil moisture content will

not result in a more dispersive ensemble. As such, Fig. 6.11 represents nearly the largest ensemble dispersion achievable by modifying the surface moisture parameters.

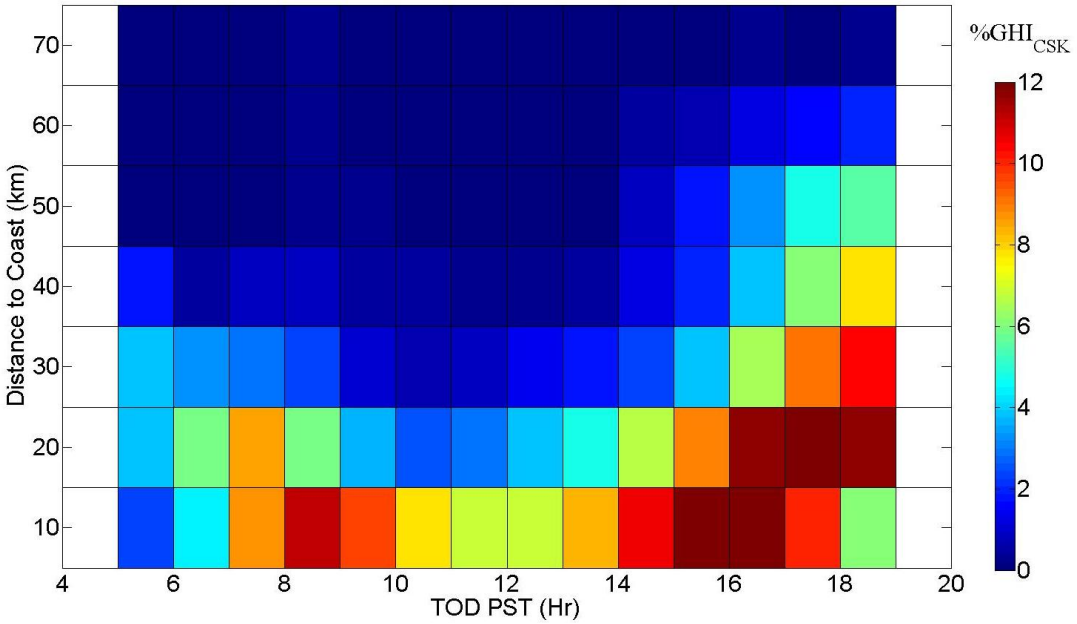


Fig. 6.11: Forecast clear sky index spread ($P_{10} - P_{90}$) as a function of time of day and distance to coast.

6.6 Summary and Conclusions

To validate the cloud dissipation model presented in Chapter 2 (Eq. 2.19), idealized, two-dimensional WRF simulations were conducted for a variety of β. In these simulations, precipitation and latent heating from cloud microphysics were disabled. Furthermore, the model was initialized with horizontal velocities of zero and boundary conditions were periodic. Since the surface parameters were identical for all grid points, no horizontal pressure gradients could form. As such, no advection took place. Overall, Eq. 2.19 was validated, showing that the surface heating contribution to the cloud dissipation rate could be predicted from the Bowen ratio.

For May and June of 2011, WRF was used to simulate MLS clouds in San Diego, CA. Using SolarAnywhere data, WRF-simulated and observed cloud dissipation rates were compared.

Overall, WRF-simulated MLS clouds dissipated 1.9 hours early which translated to β approximately 2-4 larger than ideal (Fig. 6.6a). This discrepancy was largest for inland regions, where the WRF-simulated cloud dissipation rate was largest. Overall, 21.6% of WRF-simulated β exceeded 10 (Fig. 6.8) reflecting large sensible heat fluxes due to extraordinarily dry surface conditions. This suggests a deficiency in the soil initial conditions as derived from the NAM. Though precipitation is infrequent in summertime coastal California, underground water movement, substantial irrigation, and marine layer fog condensation supply the soil with moisture making the NAM-derived Bowen ratios appear unrealistic.

In general, the NAM over-predicts irradiation, even in clear conditions (Fig. 6.7 and Mathiesen and Kleissl, 2011). Since solar irradiation is the primary determinant of evapotranspiration, it is likely that NAM-modeled evapotranspiration is too large, resulting in excessive drying of the soil. Furthermore, as NAM-simulated clouds are rare, there is no source of precipitation or fog condensation. Subsequently, this negative feedback makes cloud formation less likely and further enhances soil drying. Additionally, the present findings retrospectively explain why day-ahead forecasts were slightly more accurate when cloud liquid water was assimilated into WRF initial conditions (Mathiesen *et al.*, 2013b) based on satellite observations. This resulted in extra WRF-simulated precipitation which likely reduced day-ahead forecast β as the soil moisture content was increased. With reduced sensible heat fluxes, cloud dissipation rates were smaller in day-ahead forecasts, which possibly contributed to more accurate day-ahead when compared to intra-day forecasts (Mathiesen *et al.*, 2013b).

To improve forecast accuracy and reduce cloud dissipation rates, a soil moisture perturbation was introduced to the surface boundary conditions. Using Eq. 6.4 and the background uncertainty from Fig. 6.6, the surface soil moisture contents were modified for 30 MLS days in May and June, 2011. As expected, the smallest soil moisture perturbations (P_{10}) resulted in larger β (Fig. 6.8, solid-thin red line), fast cloud dissipation rates, and highest

irradiance at the surface. Conversely, large soil moisture perturbations resulted in the longest cloud lifetimes and lowest irradiance at the surface. Overall, P_{50} forecast (the ensemble member using $\Delta_{50}q_g$) β were significantly reduced (Fig. 6.8) and only 1.2% exceeded 10. As such, sensible heat fluxes and PBL heating were reduced.

Validated against SolarAnywhere data, the timing of cloud dissipation was improved by 0.5 hrs and irradiance forecast mean absolute error (MAE) was decreased by 25 W m^{-2} in coastal areas. Inland, where MLS clouds were rare, MAE was not improved. If all assumptions in the mixed layer model were valid, then the P_{50} forecast ($\gamma = 0.5$) would yield a roughly unbiased cloud dissipation time on average. In practice, however, the heat and moisture inputs not accounted for in Eq. 2.19 (e.g. precipitation, advection, etc.) will result in additional forcing that could accelerate cloud dissipation. It should also be noted that since training and validation dataset were identical, the soil moisture corrections (Fig. 6.6) are idealized, and errors presented in Section 5 are overly optimistic. However, given the relatively consistent Southern California summer climate, only relatively small changes in marine layer dissipation times and soil moisture corrections year-over-year are expected. Comparatively, this method is more effective than other forecast improvement techniques. Model-output-statistics (MOS, Lorenz *et al.*, 2009, Mathiesen and Kleissl, 2011) using bivariate regression to statistically remove forecast bias, improved forecast MAE by 17.1 W m^{-2} for one year of instantaneous hourly NAM irradiance forecasts. Similarly, direct-cloud-assimilation (Mathiesen *et al.*, 2013b) addressed the uncertainty in the model atmospheric initial conditions and only improved hourly average WRF MAE by 10.5 W m^{-2} when compared to the NAM for May and June 2011 (the same time period used in this study). Likely, the soil moisture perturbation method presented in this study outperforms these other techniques because it directly addresses the physical processes that effect cloud dissipation. By reducing β, more realistic PBL heating rates were established which resulted in more accurate cloud dissipation rates and irradiance estimates at the surface.

Furthermore, dispersion statistics were presented in Section 5b. Here, the uncertainty in the surface boundary conditions was propagated through the model and expressed as a spread in the irradiance signal at the surface. Overall, model dispersion was largest in the morning and evening (Fig. 6.11) at approximately 12% of GHI_{CSK}. Inland, where clouds are rare, the ensemble members agreed and forecast dispersion was small. On average, however, the ensemble was significantly under-dispersive when compared to observation, indicating that further perturbations are necessary for an effective ensemble system.

As demonstrated by Fig. 6.11, model dispersion from the modification of the soil initial conditions is less than observed. Since q_g is bounded by dry and saturation limits, its potential influence on cloud dissipation rate is constrained according to Eq. 2.19. For instance, as q_g approaches its dry limit, β goes to infinity and the latent terms of Eq. 2.19 go to zero. The cloud dissipation rate is thus limited by the remaining terms: The total turbulent flux, the inversion height, the PBL air density, and the PBL temperature. In observation, cloud dissipation rates can exceed these limits as other factors influence the total cloud dissipation rate. As such, the perturbation of the soil moisture alone is insufficient to produce an unbiased P_{50} forecast and accurately dispersive ensemble. Fig. 6.4 implies that outside of the surface heating rates, advection has the largest influence on the temperature of the PBL. Other factors such as radiative heating rates, microphysical heating rates, inversion altitude, and precipitation play a secondary role. To create more dispersive ensemble, perturbations to the initial velocity field and the physics that influence advection, particularly the sea-breeze, could be used in conjunction with the surface soil moisture perturbation.

In addition to the more encouraging findings presented in this study, several other methods were attempted with limited success. For each, the goal was to reduce the sensible heating within the PBL. First, modifications to the physics parameterizations were executed to influence PBL heating and cloud dissipation rates. For instance, the surface thermal roughness

length was significantly reduced in order to diminish the efficiency at which sensible heat was transferred to the PBL. While sensible heat fluxes were indeed initially reduced, energy conservation resulted in significant heat storage within the soil which yielded unphysical skin temperatures which eventually *increased* sensible heat fluxes. This feedback negated much of the expected reduction in sensible heat flux and cloud dissipation rates varied little. PBL mixing length scales were also studied in detail. By changing the relative importance of the surface, buoyant, and turbulent mixing length scales, the PBL heating rate and the rate of dry-air entrainment could be controlled. Though this resulted in changes to the cloud dissipation rate, mixing lengths had to be changed to extreme levels that were difficult to justify. Ultimately, it was determined that a multi-parameter based approach (in which the physics parameterizations are modified) was less effective than an initial condition perturbation method.

6.6 Acknowledgements

The entirety of this chapter in conjunction with material from Chapter 2 has been submitted for publication as Mathiesen *et al.*, 2014.

Chapter 7 Afterword

Numerical weather prediction (NWP) is an essential tool in the burgeoning field of solar forecasting. More accurate than statistical or imagery-based techniques for the critical medium to long-range solar forecasting timescales (balance of day/day-ahead), NWP forecasts are the primary component of any comprehensive forecasting system. As such, improvements to their accuracy are an active and vital field of research. This project explored three innovative methods for improving NWP forecast accuracy, specifically in the dynamic and difficult to predict region of coastal California. Overall, it was shown that by using these methods, significant forecast improvements could be obtained.

One of the primary advantages of NWP is their ease of accessibility. Free of charge, the National Centers for Environmental Prediction (NCEP) provides NWP forecasts for the Continental United States using several models. Chapter 3 explored these models and their accuracy. In general, it was shown that the models consistently over-predict irradiance. The majority of this error was attributed to incorrect cloud cover forecasts (e.g. too few clouds). However, it was shown that, even in clear conditions the operational NWP over-predict irradiance, indicating a potential problem with the radiative transfer models or inaccurate characterization of background atmospheric constituents. These errors motivated the statistical correction techniques presented in Chapter 4, which nearly eliminated bias error and significantly reduced root-mean-squared error.

Statistical techniques, however, do not address the inherit limitations with numerical modeling. NWP error can occur from a variety of sources (Chapter 1.4): Model resolution, inaccurate physics parameterizations, and initial/boundary conditions are the primary modes. To address these, this project presented a cloud-assimilating NWP (WRF-CLDDA, Chapter 5) and a surface-condition-based ensemble (WRF-SRAF, Chapter 6). Importantly, these models used

meteorological theory to justify their implementation. For instance, the mixed-layer model was utilized to derive an analytical expression for cloud dissipation rate in coastal California. Subsequently, this expression was used to motivate changes to the simulated soil moisture content at the surface boundary. Overall, these provided an accurate alternative to the operationally available NWP.

Together, Chapters 4, 5, and 6 presented three innovative but introductory methods for improving the accuracy in NWP solar irradiance forecasts. As the three methods were distinct, there was little time to go further in depth with each. As such, there are many possibilities to expand upon this research. For instance, the statistical correction techniques could be improved by introducing a regime-based dependence on the correction function. Under certain metrological conditions (an approaching front for instance) cloud forecasts may be more accurate. Consequently, in this regime bias errors would be different than typical and the overall correction function may not be applicable. As such, distinct correction functions could be derived for each regime and dynamically applied, resulting in a more accurate forecast.

Additionally, improving model initial conditions further will likely result in large improvements to forecast accuracy. Three- and Four-Dimensional Variational data assimilation (3D/4DVAR) could be used to integrate more observations. In California, observations that capture the conditions influence marine layer stratocumulus, such as accurate inversion observations, would be most beneficial. Additionally, the adjoint method, in which the regions/observations that will have the largest influence on forecast accuracy are targeted for data assimilation, could be implemented.

Lastly, improvements to the ensemble forecasting system will provide a large benefit for solar forecasting. It is known that the combination of an ensemble of individual deterministic forecasts will yield a higher accuracy than any single member could. As such, researching new methods to produce a diverse set of solutions is important. Chapter 6 examined this by varying

surface parameters. There are many other facets that should be explored; seabreeze/advection, cloud radiative characteristics, precipitation, and microphysics interactions are all potential areas that could vary significantly among ensemble members. Furthermore, new methods of combining the ensemble members, either through statistical techniques, artificial intelligence methods, or by implementing the analogues approach could all significantly improve forecast accuracy.

It is hoped that the pioneering work completed here will serve as the foundation for more advanced techniques to be developed by the Solar Resource Assessment and Forecasting Laboratory at the University of California, San Diego and that UCSD-SRAF will continue to function as a leader in solar forecasting research for the foreseeable future.

References

Albers, S., J. McGinley, D. Birkenheuer, and J. Smart, 1996: The local analysis and prediction system (LAPS): Analyses of clouds, precipitation and pressure. *Weather and Forecasting*. **11** (3), 273-287.

Atkinson, B.W., and J.W. Zhang, 1996: Mesoscale shallow convection in the atmosphere. *Review of Geophysics*, **34** (4), 403-431.

Baldocchi, D., E. Falge, L. Gu, R. Olson, D. Hollinger, S. Running, P. Anthoni, C. Bernhofer, K. Davis, R. Evans, J. Fuentes, A. Goldstein, G. Katul, B. Law, X. Lee, Y. Malhi, T. Meyers, W. Munger, W. Oechel, K.T. Paw, K. Pilegaard, H.P. Schmid, R. Valentini, S. Verma, T. Vesala, K. Wilson, and S. Wofsy, 2001: FLUXNET: A new tool to study the temporal and spatial variability of ecosystem-scale carbon dioxide, water vapor, and energy flux densities. *Bulletin of the American Meteorological Society*, **82** (11), 2415-2434.

Benjamin, S., D. Kim, and J. Brown, 2002: Cloud/hydrometeor initialization in the 20-km RUC using GOES and radar data. *Proceedings of the 10th Conference on Aviation, Range, and Aerospace Meteorology*, American Meteorological Society, Portland, OR, USA.

Benjamin, S., D. Dévényi, S. Weygandt, K. Brundage, J. Brown, G. Grell, D. Kim, B. Schwartz, T. Smirnova, and T. Smith, 2004a: An hourly assimilation-forecast cycle: The RUC. *Monthly Weather Review*, **132** (2), 495-518.

Benjamin, S., S. Weygandt, J. Brown, T. Smith, T. Smirnova, W. Moniger, and B. Schwartz, 2004b: Assimilation of METAR cloud and visibility observations in the RUC. *Proceedings of the 11th Conference on Aviation, Range, and Aerospace and the 22nd Conference on Severe Local Storms*, American Meteorological Society, Hyannis, MA, USA.

Benjamin, S., D. Devenyi, T. Smirnova, S. Weygandt, J.M. Brown, S. Peckham, K.J. Brundage, T.L. Smith, G.A. Grell, and T.W. Schlatter, 2006: From the 13-km RUC to the Rapid Refresh. *12th Conference on Aviation, Range, and Aerospace Meteorology*, Atlanta, GA, 2006.

Benjamin, S., C. Alexander, M. Hu, D. Dowell, S. Weygandt, E. James, P. Hofmann, T. Smirnova, J. Brown, J. Olson, K. Brundage, and B. Jamison, 2013: Data assimilation and model updates in the 2013 Rapid Refresh (RAP) and High-Resolution Rapid Refresh (HRRR) analysis and forecast systems. Presentation at NCEP/EMC Model Evaluation Group meeting, June 6th, 2013. Available online at http://ruc.noaa.gov/pdf/NCEP_HRRR_RAPv2_6jun2013-Benj-noglob.pdf.

Bennetts, D., E. McCallum, and S. Nicholls, 1986: Stratocumulus: An introductory account. *The Meteorological Magazine*, **115**, 65-76.

Berner, J., and S.-Y. Ha, J.P. Hacker, A. Fournier, and C. Snyder, 2011: Model uncertainty in a mesoscale ensemble prediction system: Stochastic versus multiphysics representations. *Monthly Weather Review*, **139** (6), 1972-1995.

Beyer, H., J. Martinez, M. Suri, J. Torres, E. Lorenz, S. Müller, C. Hoyer-Klick, and P. Ineichen, 2009: Report on benchmarking of radiation products, Management and Exploitation of Solar

Resource Knowledge (MESOR) report contract number 038665, available online at: http://www.mesor.net/deliverables.html. Accessed 3/11/12.

Blake, D., 1928: Temperature inversions at San Diego, as deduced from aerographical observations by airplane. *Monthly Weather Review*, **56** (6), 221-224.

Bofinger, S., and G. Heilscher, 2006: Solar Electricity Forecast – Approaches and first results. 21st PV Conference. Dresden, Germany.

Bond, N.A., C.F. Mass, and J.E. Overland, 1996: Coastally trapped wind reversals along the United States west coast during the warm season. Part I: Climatology and temporal evolution. *Monthly Weather Review*. **124** (3), 430-445.

Bosart, L., 1983: Analysis of a California Catalina Eddy Event. *Monthly Weather Review*. **111**, 1619-1633.

Box, G.E.P., G.M. Jenkins, and G.C. Reinsel, 2008: Time series analysis: Forecasting and control. 4th Ed. Wiley.

Bremnes, J.B., 2004: Probabilistic wind power forecasts using local quantile regression. *Wind Energy*. **7**, 47-54.

Buizza, R., P.L. Houtekamer, Z. Toth, G. Pellerin, M. Wei, and Y. Zhu, 2005: A comparison of the ECMWF, MSC, and NCEP global ensemble prediction systems. *Monthly Weather Review*, **133** (5), 1076-1097.

Campbell Scientific, 1992. Eppley PSP – precision spectral pyranometer instruction manual. Campbell Scientific Instruction Manual.

Campbell Scientific, 1996. LI200S Pyranometer instruction manual. Campbell Scientific Technical Specifications, Revision 2/96.

Chou, M.D. and M.J. Suarez, 1999: A solar radiation parameterization for atmospheric studies. NASA Technical Report. NASA/TM-1999-104606, Vol. 15, 38 pgs.

Chou, M.D., and M.J. Suarez, 2001: A thermal infrared radiation parameterization for atmospheric studies. NASA/TM-2001-104606, Vol. 19, 55 pgs.

Chow, C.W., B. Urquhart, M. Lave, A. Dominguez, J. Kleissl, J. Shields, and B. Washom, 2011: Intra-hour forecasting with a total sky imager at the UC San Diego solar energy testbed. *Solar Energy*, **85** (11), 2881-2893.

CIMIS, 2009a: CIMIS Overview. http://www.cimis.water.ca.gov/cimis/infoGenCimisOverview.jsp. Accessed 7/29/2011.

CIMIS, 2009b. Sensor Specs – Total solar radiation (pyranometer). http://www.cimis.water.ca.gov/cimis/infoStnSensorSpec.jsp. Accessed 7/29/2011.

CIMIS, 2009c: QC Overview. http://www.cimis.water.ca.gov/cimis/dataQc.jsp. Accessed 7/29/2011.

CIMIS, 2009d: Current Hourly Flags. http://www.cimis.water.ca.gov/cimis/dataQcCurrentHourly.jsp. Accessed 7/29/2011.

Clough, S.A, M.J. Iacono, and J. Moncet, 1992: Line-by-line calculations of atmospheric fluxes and cooling rate: Application to water vapor. *Journal of Geophysical Research*, **97** (14), 15761-15785.

Coimbra, C., and H. Pedro, 2013: Stochastic learning methods. In: *Solar Energy Forecasting and Resource Assessment, 1st Edition*, Editors: J. Kleissl.

Cotton, W., G. Bryan, and S. van den Heever, 2011: Chapter 6: Fogs and stratocumulus clouds. In: *Storm and Cloud Dynamics*.

Delle Monache, L., T. Nipen, Y. Liu, G. Roux, and R. Stull, 2011: Kalman filter and analog schemes to postprocess numerical weather predictions. *Monthly Weather Review*, **139** (11), 3554-3570.

Diagne, M., M. David, P. Lauret, J. Boland, and N. Schmutz, 2013: Review of solar irradiance forecasting methods and a proposition for small-scale insular grids. *Renewable and Sustainable Energy Reviews*, **27**, 65-76.

Dudhia, J., 1989: Numerical study of convection observed during the winter monsoon experiment using a mesoscale two-dimensional model. *Journal of Atmospheric Sciences*. **46** (20), 3077-3107.

ECMWF, 2012: IFS Documentation – Cy37r2. ECMWF Technical Document available at http://www.ecmwf.int/research/ifsdocs/CY37r2/IFSPart4.pdf.

Ek, M.B., K.E. Mitchell, Y. Lin, E. Rogers, P. Grunmann, V. Koren, G. Gayno, and J.D. Tarpley, 2003: Implementation of Noah land surface model advances in the National Centers for Environmental Prediction operational mesoscale Eta model. *Journal of Geophysical Research*, **108** (D22).

Fu, Q., 1996: An accurate parameterization of the solar radiative properties of cirrus clouds for climate models. *Journal of Climate*, **9** (9), 2058-2082.

Girodo, M. 2006. Solarstrahlungsvorhersage auf der Basis numerischer Wettermodelle. Ph.D. dissertation, Oldenburg Univ., Germany.

Ghonima, M.S., B. Urquhart, C.W. Chow, J.E. Shields, A. Cazorla, and J. Kleissl, 2012: A method for cloud detection and opacity classification based on ground based sky imagery. *Atmospheric Measurement Techniques*, **5** (4), 4535-4569.

Grell, G.A., 1993: Prognostic evaluation of assumptions used by cumulus parameterizations. *Monthly Weather Review*, **121** (3), 764-787.

Han, J., and H.L. Pan, 2011: Revision of convection and vertical diffusion schemes in the NCEP global forecast system. *Weather and Forecasting*, **26** (4), 520-533.

Hansen, C.W., J.S. Stein, and A. Ellis, 2010: Statistical criteria for characterizing irradiance time series. Sandia National Laboratories Report SAND2010-7314.

Heinemann, D., E. Lorenz, and M. Girodo, 2006: Forecasting of solar radiation. In: *Solar Energy Management for Electricity Generation*, Editors: E.D. Dunlop, L. Wald, and M. Súri.

Hong, S.Y., and H.L. Pan, 1996: Nonlocal boundary layer vertical diffusion in a medium-range forecast model. *Monthly Weather Review*, **124** (10), 2322-2339.

Hou, Y., S. Moorthi, K. and Campana, 2002: Parameterization of Solar radiation transfer in the NCEP models. *NCEP Office Note 441*, 1-34.

Hu, M., S. Weygandt, M. Xue, and S. Benjamin, 2007: Development and testing of a new cloud analysis package using radar, satellite, and surface cloud observation within GSI for initializing rapid refresh. *Proceedings of the 18th Conference on Numerical Weather Prediction*. American Meteorological Society, Park City, UT, USA.

Hudson, J., and P. Frisbie, 1991: Cloud condensation nuclei near marine stratus. *Journal of Geophysical Research*. **96**(D11), 20797-20808.

Ineichen, P., and R. Perez, 2002: A new airmass independent formulation for the Linke turbidity coefficient. *Solar Energy*, **73** (3), 151-157.

Inman, R.H., H.T.C. Pedro, and C.F.M. Coimbra, 2013: Solar forecasting methods for renewable energy integration. *Progress in Energy and Combustion Science*, Article in Press.

Janjic, Z., 1994: The step-mountain eta coordinate model: Further developments of the convection, viscous sublayer, and turbulence closure schemes. Monthly Weather Review. 122, 927-945.

Janjic, Z., 2000: Comments on "Development and evaluation of a convection scheme for use in climate models." Journal of Atmospheric Sciencies. 57, 3686.

Janjic, Z., R. Gall, and M.E. Pyle, 2010: Scientific documentation for the NMM solver. NCAR Technical Note NCAR/TN 477+STR.

Janjic, Z., T. Black, M. Pyle, B. Ferrier, H.Y. Chuang, D. Jovic, N. McKee, R. Rozulmalski, J. Michalakes, D. Gill, J. Dudhia, M. Duda, M. Demirtas, L. Nance, T. Slovacek, J. Wolff, L. Bernadet, P. McCaslin, and M. Stoelinga, 2011: User's guide for the NMM core of the Weather Research and Forecast (WRF) modeling system version 3. 195 pg.

Kain, J., 2004: The Kain-Fritsch convective parameterization: An update. *Journal of Applied Meteorology*. **43**, 170-181.

Lacis, A.A. and J.E. Hansen, 1974: A parameterization for the absorption of solar radiation in the Earth's atmosphere. *Journal of Atmospheric Science*, **31** (1), 118-133.

Lara-Fanego, V., J.A. Ruiz-Arias, D. Pozo-Vázquez, F.J. Santos-Alamillos, and J. Tovar-Pescador, 2012: Evaluation of the WRF model solar irradiance forecasts in Andalusia (southern Spain). *Solar Energy*, **86** (8), 2200-2217.

Larson, V.E., 2013: Forecasting solar irradiance with numerical weather prediction models. In: *Solar Energy Forecasting and Resource Assessment, 1st Edition*, Editors: J. Kleissl.

Leipper, D.F., 1948: Fog development at San Diego, California. *Journal of Marine Research*, **7**, 337-346.

Leipper, D, 1994: Fog on the US west coast: A review. *Bulletin of American Meteorological Society*. **75**, 229-240.

Lew, D., and R. Piwko, 2010: Western wind and solar integration study. NREL Technical Report, NREL/SR-550-47434, Golden, CO: National Renewable Energy Laboratory. pp. 536.

Lilly, D.K., 1968: Models of cloud-topped mixed layers under a strong inversion. *Quarterly Journal of the Royal Meteorological Society*, **94**, 292-309.

Lopez-Coto, I., P. Mathiesen, J.L. Bosch, and J. Kleissl, 2014a: Comparison between several parameterization schemes in WRF for solar forecasting in coastal zones. Submitted to *Weather and Forecasting*, September 2013.

Lopez-Coto, I., P. Mathiesen, and J. Kleissl, 2014b: Deterministic prediction using various post-processing methods for solar irradiance forecasting. Submitted to *Weather and Forecasting*, September 2013.

Lorenz, E., J. Hurka, D. Heinemann, and H.G. Beyer, 2009: Irradiance forecasting for the power prediction of grid-connected photovoltaic systems. *IEEE Journal of Selected Topics in Applied Earth Observations and Remote Sensing*, **2** (1), 2-10.

Mathiesen, P.J., and J. Kleissl, 2011: Evaluation of numerical weather prediction for intra-day solar forecasting in the continental United States. *Solar Energy*, **85** (5), 967-977.

Mathiesen, P.J., J.M. Brown, and J. Kleissl, 2013a: Geostrophic wind dependent probabilistic irradiance forecasts for coastal California. *IEEE Transactions on Sustainable Energy*, **4** (2), 510-518.

Mathiesen, P., C. Collier, and J. Kleissl, 2013b: A high-resolution, cloud-assimilating numerical weather prediction model for solar irradiance forecasting. *Solar Energy*, **92**, 47-61.

Mathiesen, P., C. Collier, and J. Kleissl, 2013c: Case studies of solar forecasting with the weather research and forecasting model at GL-Garrad Hassan in *Solar Energy Forecasting and Resource Assessment, 1st Ed.*. Editor: Jan Kleissl. Elsevier Publishing, 2013.

Mathiesen, P., J. Norris, I. Lopez-Coto and J. Kleissl, 2014: Development of a cloud lifetime ensemble for solar irradiance forecasting. Submitted to *Monthly Weather Review*, October 2013.

Marquez, R., and C. Coimbra, 2011: Forecasting of global and direct solar irradiance using stochastic learning methods, ground experiments, and the NWS database. *Solar Energy*, **85** (5), 746-756.

Mass, C., and M. Albright, 1989: Origin of the Catalina Eddy. *Monthly Weather Review*. **117** (11), 2406-2436.

Miller, S.D., A.K. Heidinger, and M. Sengupta, 2013: Physically based satellite methods. In: *Solar Energy Forecasting and Resource Assessment, 1st Edition*, Editors: J. Kleissl.

Mlawer, E. and S. Clough, 1997: Shortwave and longwave enhancements in the Rapid Radiative Transfer Model. *Proceedings of the 7th Atmospheric Radiation Measurement (ARM) Science Team Meeting*. U.S. Department of Energy, CONF-9603149.

Mlawer, E., S. Taubman, P. Brown, M. Iacono, and S. Clough. 1997: Radiative transfer for inhomogeneous atmospheres: RRTM, a validated correlated-k model for the longwave. *J. Geophysical Research*. **102** (14), 16663-16682.

Morcrette, J., P. Bechtold, A. Beljaars, A. Benedetti, A. Bonet, F. Doblas-Reyes, J. Hague, M. Hamrud, J. Haseler, J. Kaiser, M. Leutbecher, G. Mozdzynski, M. Razinger, D. Salmond, S. Serrar, M. Suttie, A. Tompkins, A. Untch, and A. Weisheimer, A. 2007: Recent advances in radiation transfer parameterizations. *ECMWF Tech. Memo.* 539, 1-52.

Morrison, H., J.A. Curry, and V.I. Khvorostyanov, 2005: A new double-moment microphysics parameterization for application in cloud and climate models. Part I: Description. *Journal of the Atmospheric Sciences*, **62** (6), 1665-1677.

Murphy, J.M., D.M.H. Sexton, D.N. Barnett, G.S. Jones, M.J. Webb, M. Collins, and D.A. Stainforth, 2004: Quantification of modeling uncertainties in a large ensemble of climate change simulations. *Nature*, **430**, 768-772.

Nakanishi, M., and H. Niino, 2006: An improved Mellor-Yamada level-3 model: Its numerical stability and application to a regional prediction of advection fog. *Boundary Layer Meteorology*, **119**, 397-407.

NCEP, 2013: The GFS Atmospheric Model. Available online: http://www.emc.ncep.noaa.gov/gmb/moorthi/gam.html. Accessed 9/11/2013.

Nicholls, S., 1984: The dynamics of stratocumulus: Aircraft observations and comparisons with a mixed layer model. *Quarterly Journal of the Royal Meteorological Society*. **110**, 783-820.

Novakovskaia, E., C. Sloop, and Z. Guo, 2011: The impact of real-time observations on the WRF model surface forecasts. *11th EMS Annual Meeting*, **8**, EMS-2011-605-1.

Ohtake, H., K. Shimose, J.G.S. Fonseca, T. Takashima, T. Oozeki, and Y. Yamada, 2012: Accuracy of the solar irradiance forecasts of the Japan Meteorological Agency mesoscale model for the Kanto region, Japan. *Solar Energy*, Article in Press.

Otkin, J.A., and T.J. Greenwald, 2008: Comparison of WRF model-simulated and MODIS-derived cloud data. *Monthly Weather Review*, **136** (6), 1957-1970.

Paluch, I., and D. Lenschow, 1991: Stratiform cloud formation in the marine boundary layer. *Journal of Atmospheric Sciences*. **48** (19), 2141-2158.

Pan, H.L. and W.S. Wu, 1995: Implementing a Mass Flux Convection Parameterization Package for the NMC Medium-Range Forecast Model. *NMC Office Note, No. 409*, 1-40.

Pellend, S., G. Galanis, G. Kallos, 2011: Solar and photovoltaic forecasting through post-processing of the Global Environmental Multiscale numerical weather prediction model. *Progress in Photovoltaics: Research and Applications*, **21** (3), 284-296.

Perez, R., P. Ineichen, K. Moore, M. Kmiecik, C. Chain, R. George, and F. Vignola, 2002: A new operational model for satellite-derived irradiances: Description and validation. *Solar Energy*, **73** (5), 307-317.

Perez, R., K. Moore, S. Wilcox, D. Renné, and A. Zelenka, 2007: Forecast solar radiation – preliminary evaluation of an approach based upon the national forecast database. *Solar Energy*, **81** (6), 809-812.

Perez, R., S. Kivalov, J. Schlemmer, K. Hemker Jr., D. Renné, and T.E. Hoff, 2010: Validation of short and medium term operational solar radiation forecasts in the US. *Solar Energy*, **84** (12), 2161-2172.

Perez, R., M. Beauharnois, K. Hemker, S. Kivalov, E. Lorenz, S. Pelland, J. Schlemmer, and G. Van Knowe, 2011: Evaluation of numerical weather prediction solar irradiance forecasts in the US. *Proceedings of Solar 2011, American Solar Energy Society*, Raleigh, NC.

Perez, R., E. Lorenz, S. Pellend, M. Beauharnois, G. Van Knowe, K. Hemker Jr., D. Heinemann, J. Remund, S.C. Müller, W. Traunmüller, G. Steinmauer, D. Pozo, J.A. Ruiz-Arias, V. Lara-Fanego, L. Ramirez-Santigosa, M. Gaston-Romero, and L.M. Pomares, 2013: Comparison of numerical weather prediction solar irradiance forecasts in the US, Canada, and Europe. *Solar Energy*, **94**, 305-326.

Peterman, C., 2012: Renewables Portfolio Standards (RPS) Proceeding Docket #11-RPS-01 and 03-RPS-1078. California Energy Commission. http://www.energy.ca.gov/portfolio/index.html. Accessed 8/20/2012.

Pilié, R.J., E.J. Mack, C.W. Rogers, U. Katz, and W.C. Kocmond, 1979: The formation of marine fog and the development of fog-stratus systems along the California coast. *Journal of Applied Meteorology*. **18** (10), 1275-1286.

Reikard, G., 2009: Predicting solar radiation at high resolutions: A comparison of time series forecasts. *Solar Energy*, **83** (3), 342-349.

Remund, J., R. Perez, and E. Lorenz, 2008: Comparison of solar radiation forecasts for the USA. *2008 European PV Conference*, Valencia, Spain.

Rogers, E., T. Black, B. Ferrier, Y. Lin, D. Parrish, and G. DiMega, 2001: Changes to the NCEP meso eta analysis and forecat system: Increase in resolution, new cloud microphysics, modified precipitation assimilation, modified 3DVAR analysis. http://www.emc.ncep.noaa.gov/mmb/mmbpll/eta12tpb/. Accessed 9/9/13.

Rogers, S., 2007: 2D weighted polynomial fitting and evaluation. *Matlab Central File Exchange*. http://www.mathworks.com/matlabcentral/fileexchange/13719-2d-weighted-polynomial-fitting-and-evaluation. Accessed 8/25/2010.

Rogers, E., G. DiMego, T. Black, M. Ek, B. Ferrier, G. Gayno, Z. Janjic, Y. Lin, M. Pyle, V. Wong, W.S. Wu, and J. Carley, 2009: The NCEP North American mesoscale modeling system: Recent changes and future plans. *23rd Conference on Weather Analysis and Forecasting* and the *19th Conference on Numerical Weather Prediction*. American Meteorological Society. Omaha, NE, USA.

Rozendaal, M.A., C.B. Leovy, and S.A. Klein, 1995: An observational study of diurnal variations of marine stratiform cloud. *Journal of Climate*, **8** (7), 1795-1809.

Schwartz, R.E., L. Nonnenmacher, V. Kostylev, S.F. Iacobellis, and A. Gershunov, 2012: Exploring meteorological and climatic conditions driving California coastal marine layer clouds. *American Geophysical Union Fall Meeting*, San Francisco, CA, December 3rd-7th, 2012.

Sengupta, M., A. Heidinger, and S. Miller, 2010: Validating an operational physical method to compute surface radiation from geostationary satellites. *Proceedings of the SPIE Conference*. San Diego, CA.

Sfetsos, A., and A.H. Coonick, 2000: Univariate and multivariate forecasting of hourly solar radiation with artificial intelligence techniques. *Solar Energy*, **68** (2), 169-178.
Urquhart, B., M. Ghonima, D. Nguyen, B. Kurtz, and J. Kleissl, 2013: Sky imaging systems for short-term solar forecasting. In: *Solar Energy Forecasting and Resource Assessment, 1st Edition*, Editors: J. Kleissl.

Skamarock, W.C., R. Rotunno, and J.B. Klemp, 2002: Catalina eddies and coastally trapped disturbances. *Journal of the Atmospheric Sciences*. **59** (14), 2270-2278.

Skamarock, W.C., J.B. Klemp, J. Dudhia, D.O. Gill, D.M. Barker, M.G. Duda, X.Y. Huang, W. Wang, and J.G. Powers, 2008: A description of the advanced research WRF – version 3. NCAR Technical Note NCAR/TN 475+STR.

Slingo, A., 1989: A GCM parameterization for the shortwave radiative properties of water clouds. *Journal of Atmospheric Science*, **46** (10), 1419-1427.

Smirnova, T., J.M. Brown, and S.G. Benjamin, 1997: Performance of different soil model configurations in simulating ground surface temperature and surface fluxes. *Monthly Weather Review*, **125**, 1870-1884.

SolarAnywhere, SolarAnywhere Data. Clean Power Research 2013. Available: http://www.SolarAnywhere.com

Stensrud, D.J., J.-W. Bao, and T.T. Warner, 2000: Using initial condition and model physics perturbations in short-range ensemble simulations of mesoscale convective systems. *Monthly Weather Review*, **128** (7), 2077-2107.

Stephens, G.L., 1978: Radiation profiles in extended water clouds. II: Parameterization schemes. *Journal of Atmospheric Science*, **35** (11), 2123-2132.

Stephens, G.L., 1984: The parameterization of radiation for numerical weather prediction and climate models. *Monthly Weather Review*, **112** (4), 826-867.

SURFRAD. 2009a. SURFRAD Network Overview. http://www.srrb.noaa.gov/surfrad/surfpage0.html. Accessed 8/24/2010.

SURFRAD. 2009b. SURFRAD Data README. ftp://ftp.srrb.noaa.gov/pub/data/surfrad/README. Accessed 8/24/2010.

Thompson, G., R. Rasmussen, and K. Manning, 2004: Explicit forecasts of winter precipitation using an improved bulk microphysics scheme. Part I: Description and sensitivity. *Monthly Weather Review*. **132** (2), 519-542.

Thompson, W.T., and S.D. Burk, 2005: Fog and low clouds in a coastally trapped disturbance. *Journal of Geophysical Research*. **110**, 17 pgs.

Tiedtke, M., 1993: Representation of clouds in large-scale models. *Monthly Weather Review*, **121** (11), 3040-3061.

Tjernström, M., and D. Rogers, 1996: Turbulence structure in decoupled marine stratocumulus: A case study from the ASTEX field experiment. *Journal of Atmospheric Sciences*. **53** (4), 598-619

Toth, Z., and E. Kalnay, 1993: Ensemble forecasting at NMC: The generation of perturbations. *Bulletin of the American Meteorological Society*, **74** (12), 2317-2330.

Tselioudis, G., and C. Jakob, 2002: Evaluation of midlatitude cloud properties in a weather and a climate model: Dependence on dynamic regime and spatial resolution. *Journal of Geophysical Research*, **107** (D24), 4781.

Turton, J.D., and S. Nicholls, 1987: A study of the diurnal variation of stratocumulus using a multiple mixed layer model. *Quarterly Journal of the Royal Meteorological Society*. **113**, 969-1009.

Urquhart, B., B. Kurtz, E. Dahlin, M. Ghonima, F. Meija, J. Shields, and J. Kleissl, 2014: Development of a sky imaging system for short-term solar power forecasting. Submitted to *Applied Optics.*

Venkataraman, S., G. Jordan, R. Piwko, L. Freeman, U. Helman, C. Loutan, G. Rosenblum, M. Rothleder, J. Xie, H. Zhou, M. Kuo, B. Hobbs, J. Ma, T. Guo, W. Huang, E. Toolson, A. Pandey, B. Speckman, and P. Worhach, 2010: Integration of renewable resources: Operational

requirements and generation fleet capacity at 20% RPS. CAISO Technical Report available at http://www.caiso.com/2804/2804d036401f0.pdf. pp. 168.

Wald, L., M. Albuisson, C. Best, C. Delamare, D. Dumortier, E. Gaboardi, A. Hammer, D. Heinnemann, R. Kift, S. Kunz, M. LefÉvre, S. Leroy, M. Martinoli, L. Ménard, J.H. Page, T. Prager, C. Ratto, C. Reise, J. Remund, A. Rimoczi-Paal, E. Van Der Goot, F. Vanroy, and A. Webb, 2002: SoDa: A project for the integration and exploitation of networked solar radiation databases. *Proceedings of the European Geophysical Society Meeting, XXV General Assembly*. Nice, France.

Weygandt, S., S. Benjamin, D. Dévényi, J. Brown, and P. Minnis, 2006: Cloud and hydrometeor analysis using METAR, radar, and satellite data within the RUC/Rapid-Refresh model. *Proceedings of the 12th Conference on Aviation, Range, and Aerospace*, American Meteorological Society, Atlanta, GA, USA.

Wood, R., 2012: Stratocumulus clouds. *Monthly Weather Review*, **140** (8), 2373-2423.

Wu, W.S., R.J. Purser, and D.F. Parrish, 2002: Three-dimensional variational analysis with spatially inhomogenous covariances. *Monthly Weather Review*, **130** (12), 2905-2916.

Xue, M. D. Wang, J. Gao, K. Brewster, and K. Droegenmeier, 2003: The advanced regional prediction system (ARPS), storm-scale numerical weather prediction and data assimilation. *Meteorology and Atmospheric Physics*. **82**, 139-170.

Zack, J. 2012: Large system variable generation forecasting: Progress and challenges. UVIG Variable Generation Forecasting Workshop. Tucson, AZ. 2/8/2012.